Universiteit Utrecht

IMAU
Institute for Marine and Atmospheric research Utrecht

Modelling of sand transport in the surf zone

Master Thesis

Vera van Bergeijk
Meteorology, Physical Oceanography and Climate
Institute for Marine and Atmospheric Research, Utrecht University

Supervisors:

Prof. Dr. H.E. de Swart
Institute for Marine and Atmospheric Research

Prof. Dr. B.G. Ruessink
Department of Physical Geography

September 13, 2017

Abstract

Coastal zones across the entire globe are threatened by coastal retreat and increased flood risk due to rising sea levels. A large fraction of the world's population lives in coastal regions and roughly 20% of the world's coastlines are sandy beaches which are highly dynamic. Sandy beaches are found along 20% of the worlds coast and are highly dynamic. Beaches generally erode during high energy conditions, while they accrete during the subsequent low energy conditions. The processes resulting in offshore transport are well understood, but this is not the case for the onshore transport during low energy conditions. Onshore transport is the result of non-linearities in the wave-velocity and acceleration, but the relative contribution of the acceleration-driven transport and the transport related to wave velocity is unknown. The relative contribution of acceleration-driven transport and the transport due to waves to the onshore sand transport during low to moderate energy conditions was investigated in a combined data-model study. Measurements of flow velocities, sand concentrations and the morphology in the intertidal area were performed over a period of 4 weeks at Vejers beach, a sandy uninterrupted coast along the Danish North sea coast. The hydrodynamical SWASH model was used to simulate the water motion and wave conditions measured during the field campaign. Comparison of the SWASH model output with the field data showed that the SWASH model is able to simulate the significant wave height in good agreement with the field data. However, the simulation of the current and the non-linearities in the sea surface elevation and wave velocity need to be further improved. The total normalised root-mean-square error between the SWASH model output and field data is 0.27 for the best fit parameters. A sand transport model was build based on the formulas of Fernández-Mora et al. (2015) including four transport mechanisms: a) transport by the waves, b) joint action of stirring of sand by waves and transport by currents, c) the acceleration-driven transport and d) the diffusive transport. The bed level change over 25.5 hours was computed using the modelled total cross-shore sand transport and compared to the observed bed level change in order to calibrate the sand transport model. For the best fit parameters of the sand transport model, the root-mean-square of the observed and modelled bed level change was 0.0595 m. The relative contributions of the four transport mechanisms to the total cross-shore transport were evaluated as a function of time and distance. The results of the modelling exercise revealed the relative contribution of the four transport mechanisms to the total cross-shore transport and showed that the velocity skewness transport mechanism dominates over the velocity asymmetry mechanism. The results also show that the total transport is dominated by the onshore transport due to waves in the shoaling zone. In the surf zone, the total transport is offshore directed and dominated by the transport due to currents. Additionally, the offshore transport by currents dominates at the edge of the shoaling zone during low water, while during high water the onshore transport by the waves dominates.

Contents

1 Introduction **1**
1.1 Problem description and research focus . . . 3
1.2 Research questions and methodology . . . 4

2 Theory **7**
2.1 Background information . . . 7
2.1.1 The coastal zone . . . 7
2.1.2 Sand transport . . . 9
2.2 Modelling waves and currents in the coastal zone . . . 15
2.2.1 Governing equations . . . 17
2.2.2 Boundary conditions . . . 20
2.2.3 Coupling between the water motion and the sand transport equations 22
2.3 Sand transport equations . . . 23
2.3.1 Transport by the waves . . . 24
2.3.2 Acceleration skewness . . . 25
2.3.3 Transport by currents . . . 25
2.3.4 The diffusive transport . . . 25
2.4 Bed evolution . . . 26

3 Material and methods **27**
3.1 Field campaign . . . 27
3.1.1 Set-up and instrumentation . . . 29
3.1.2 Grain size . . . 32
3.1.3 The measured bed level change . . . 32
3.1.4 Data selection and data processing . . . 33
3.2 The hydrodynamical model SWASH . . . 34
3.2.1 Model setup . . . 34
3.2.2 Calibration method . . . 36
3.2.3 Comparison of the SWASH output with the field data . . . 39
3.3 Sand transport model and bed level change . . . 40
3.3.1 Computation of the sand transport and the bed level change . . . 40
3.3.2 Calibration method . . . 40
3.3.3 The effect of the different transport mechanisms . . . 41

4 Results **43**
4.1 Performance hydrodynamical SWASH model 43
4.1.1 Calibration results 43
4.1.2 Comparison of the SWASH output with the field data 49
4.2 The bed level change and the calibration results of the sand transport model 50
4.3 The effect of the different transport terms 52

5 Discussion **55**
5.1 The hydrodynamics 55
5.1.1 Phase-averaged sea surface elevation 55
5.1.2 Model-data comparison of the hydrodynamical variables 57
5.2 The effect of the different sand transport mechanisms 59
5.3 Limitations in the method 60
5.3.1 Alongshore current and alongshore variability 61
5.4 The influence of the bed profile on the sand transport 64

6 Conclusions **69**

A Locations of the instruments in the cross-shore array **I**

B Skewness and Asymmetry **II**

C Table of the input variables of the 52 periods **III**

D Period P2 **IV**

E The effect of wind **V**

F The calibration results of the SWASH model using the BAR2 profile. **VII**

Chapter 1: Introduction

Coastal areas are interesting in the context of transportation, recreation, fishing, drink water and navigational purposes. Harbours are important international transport routes for goods and are a vital part of the infrastructure. Most major cities are located in the coastal zone, which is also the case in the Netherlands where 9 million people live at an elevation below sea level (Kabat et al., 2009). Figure 1.1a shows the coast at the Dutch town Zandvoort. Coastal zones across the whole world are threatened by climate change, especially by sea level rise which can cause significant coastal retreat. Leatherman et al. (2000) concluded that the shoreline retreats 15 m on average for every 10 cm of sea level rise. According to the IPPC (Stocker et al., 2013), the global mean sea level rise at the end of the century is 0.26-0.55 m in case of the mildest climate scenario (RCP 2.6), but can be up to 0.98 m for the most extreme scenario (RCP 8.5). Although the mean global sea level rise at the end of the century will be below one meter according to the IPPC, the relative sea level rise (RSLR) is expected to be larger in the Netherlands. The Delta Committee (2008) estimates an upper limit of 0.65 to 1.3 m RSLR in 2100 and in the most extreme case a RSLR of 2.0 to 4.0 m

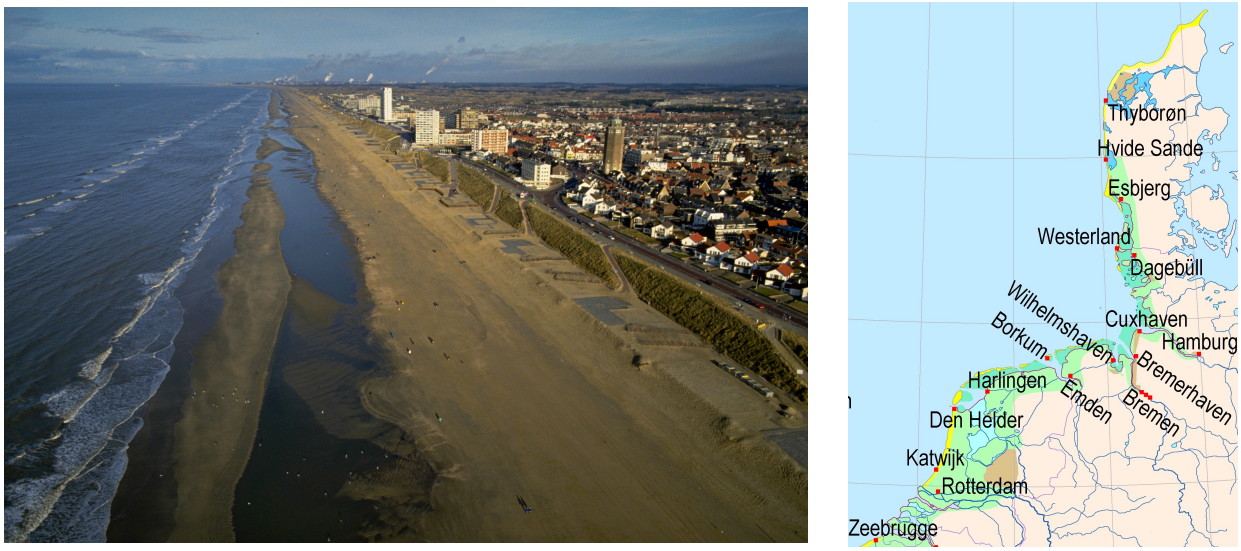

(a) **(b)**

Figure 1.1 – **(a)** A sandy coast located at Zandvoort, a coastal town in the Netherlands (*https://beeldbank.rws.nl, Rijkswaterstaat*). **(b)** The different types of coast along the south-eastern part of the North Sea: marshes (green), mudflats (greenish blue) and sandy coasts (yellow). *User: Ulamm / Wikimedia Commons / CC-BY-SA-3.0*

by 2200. According to the relation between coastal retreat and sea level rise determined by Leatherman et al. (2000), this means a coastal retreat of 300 to 600 m along the Dutch coast by 2200. Beach nourishments are performed along the Dutch coast to maintain the coast line. Annually, around 7 million cubic meters of sand are used in the Netherlands to reinforce the coast line (Rijkswaterstaat, 2017). The threat of coastal retreat due to sea level rise and responsive coastal adjustments such as beach nourishment make it essential to improve our understanding of coastal development.

Different types of coasts exist around the world, which can be categorized as sandy beaches, muddy coasts, rocky coasts and barrier coasts. An example of each type can be found along the east coast of the North Sea, as can be seen in Figure 1.1b. The Wadden Sea is an intertidal zone protected by barrier islands which starts north of Den Helder (Netherlands) and ends west of Esbjerg (Denmark). The Wadden Sea area consists of mainly mud flats and salt marshes, while the barrier islands in the Netherlands have a sandy coast on the side of the North Sea. Examples of rocky coasts are the fjords in Norway and cliffs along the coastline of Scotland. This research focuses on sandy interrupted coasts. Sandy beach systems are found along 20% of the world's coast (Masselink et al., 2014). An example of a sandy beach is seen in Figure 1.1a. Sandy coasts dominate the Dutch coast from Scheveningen (west of Rotterdam) to Den Helder and the Danish North sea coast as well (Figure 1.1b).

Changes in the morphology, the study of bedforms, of the coastal zone are the result of spacial variations in sand transport along the coast (the along-shore direction) and perpendicular to the coast (the cross-shore direction). Only the morphological changes related to the cross-shore sand transport are included in this research project because of computational limits. The cross-shore sand transport gives insight into coastal retreat and beach recovery. The total cross-shore sand transport is the result of sand transport by different mechanisms. Sand is transported offshore by joint action of sand stirring by the waves and transport by the

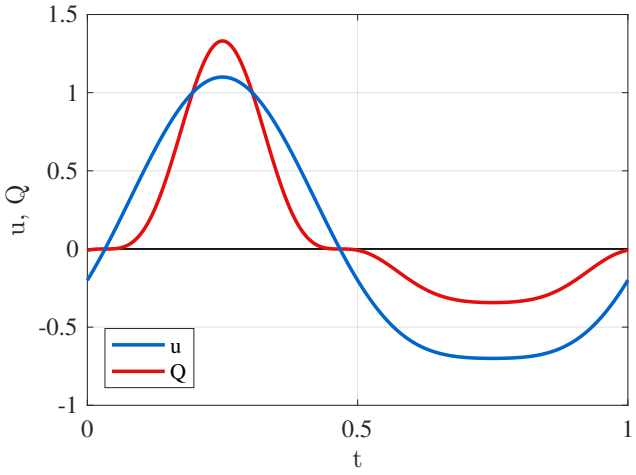

Figure 1.2 – An example of sand transport Q as function of the normalised time t due to non-linearity in the wave velocity u. The maximum onshore directed velocity is larger than the maximum offshore directed velocity resulting in net sand transport in the positive onshore direction.

cross-shore directed current (Gallagher et al., 1998). The offshore directed current is called the undertow (Svendsen, 1984) and compensates for the landward water flux by waves. The sand transport by the waves is separated into a short wave contribution (period, $T > 20$ s) and a long wave contribution (1 s $< T <$ 20 s). Long waves can transport sand in both directions, depending on the slope of the beach and the ratio of their height compared to the wave height of short waves (de Bakker et al., 2016). Sand is transported in the onshore direction by short waves due to non-linearities in the wave velocity (Hsu et al., 2006) and wave acceleration (Hoefel and Elgar, 2003). The transport due to non-linearities in the wave velocity is called the transport due to waves. An example of net transport by the waves is shown in Figure 1.2. The non-linear velocity has a crest height that is larger than the trough depth, but the trough duration is longer than the crest duration. As a consequence of the larger crest height, the net sand transport is positive and onshore directed. Similarly, non-linearity exists in the wave acceleration, which results in onshore directed sand transport called the acceleration-driven transport. The last sand transport mechanism is the diffusive transport, which is related to the slope of the sea bed and the tendency of sand to move downslope. The diffusive transport is small compared to the other types of transport and responsible for flattening of the bed (Dubarbier et al., 2015).

1.1 Problem description and research focus

The direction of the cross-shore sand transport depends on the wave energy conditions and is the result of competition between the onshore directed transport due to the wave non-linearities and the offshore directed transport of the undertow (Gallagher et al., 1998; Hoefel and Elgar, 2003; Abreu et al., 2013; Dubarbier et al., 2015). Sand is transported offshore during storms with high wave energy conditions (wave height, $H \geq 2$ m). The offshore directed transport is the result of the transport by the undertow, which dominates during storms (Gallagher et al., 1998). The offshore directed transport by the undertow is well understood and can effectively be simulated using statistical parameters and time-averaged quantities (Roelvink et al., 2009) and these descriptions are incorporated into complex models that simulate sand transport and beach morphological change (MIKE21, see Warren and Bach (1992); Delft3D, see Lesser et al. (2004); Xbeach, see Roelvink et al. (2009)). During storms, when the long waves are relatively high, the transport by long waves is offshore directed and can reach up to 60% of the total cross-shore sand transport close to the shoreline for beaches with a gentle slope (de Bakker et al., 2016). The offshore directed transport by the long waves during storms is also included in the morphological models (Roelvink et al., 2009).

During fair weather conditions when the energy conditions are low ($H \leq 1$ m) to moderate (1 m $< H <$ 2 m), the cross-shore transport is onshore directed. The undertow is weak and the long waves are small during low energy conditions, so the onshore directed transport by the short waves dominates the cross-shore transport. The first attempts to simulate onshore sandbar migration (Roelvink and Stive, 1989; Gallagher et al., 1998) were not successful, because the models only considered non-linearities in the wave velocity and not in the wave acceleration. Hoefel and Elgar (2003) were able to simulate the onshore sandbar migration using a description of the non-linearity in the wave acceleration. Hsu et al. (2006)

simulate successfully the onshore bar migration over a 5-day period using a simplified model separating the transport by waves from the transport by currents. Dubarbier et al. (2015) performed simulations of flume experiments including the sand transport due to wave velocity as well as the acceleration-driven transport and concluded that both types of transport are necessary to accurately simulate the cross-shore transport. Although it is clear that the onshore directed transport is driven by waves and the result of the wave non-linearities, the relative contribution of the acceleration-driven transport and the transport related to wave velocity is unknown. Because the main driving mechanism of the onshore transport is not known, the currently available morphodynamic models are not able to simulate the onshore sand transport with confidence. The onshore directed transport of sand during fair weather conditions is important for beach recovery between storms and a better understanding of the processes resulting in onshore sand transport is essential to improve simulations of coastal development. Fernández-Mora et al. (2015) started already to investigate the relative importance of the acceleration-driven transport and the transport by the waves. Fernández-Mora et al. (2015) simulated the same onshore bar migration event as Hsu et al. (2006) using a simple hydrodynamical model for the waves by Ruessink et al. (2012) and focussing on the bed level change related to the sand transport mechanisms. Fernández-Mora et al. (2015) concluded that the bed level change related to the acceleration-driven transport dominated close to the beach, while the bed level change due to the transport by waves was more important further offshore. However, no simulations of other bar migration events were performed as Hsu et al. (2006) suggested.

The aim of this research is to unravel which processes are important for the onshore sand transport in shallow water during low to moderate conditions by means of a combined data-model study. This project is part of the international field campaign TASTI performed in the autumn of 2016 (Brinkkemper et al., 2017) at Vejers beach, which is a sandy uninterrupted coast located west of Esbjerg along the Danish North sea coast (see Figure 1.1b). Measurements of flow velocities, sand concentrations and the morphology in the intertidal area were performed over a period of 4 weeks. The goal of this project was to build a sand transport model with focus on wave non-linearities to simulate the conditions measured during the field campaign. The sand transport formulations of Fernández-Mora et al. (2015) are used to calculate the sand transport, but in this study the contributions of the different sand transport mechanisms are investigated using a more sophisticated phase-resolving hydrodynamical model, which computes the wave-velocity for every wave separately instead of using a parametrization of the wave-velocity as done by Fernández-Mora et al. (2015).

1.2 Research questions and methodology

In this thesis the following three research questions and objectives will be answered:

1. What is the skill of a fully wave phase-resolving model for simulating the hydrodynamics at Vejers beach during fair weather conditions?
The hydrodynamics at Vejers beach are modelled using the wave phase-resolving SWASH model (Zijlema et al., 2011), which resolves the sea surface elevation and the wave veloci-

ties. This is an improvement compared to the simulations of Dubarbier et al. (2015) and Fernández-Mora et al. (2015) who used parametrizations of the wave velocity. The non-linearities in wave velocity and acceleration are important for the onshore directed transport, so it is essential to simulate these quantities correctly. The model output of the SWASH model is compared to the field data and the skill of the model is determined based on a normalised root-mean-square error between the model output and the field data.

2. How does the modelled cross-shore transport gradient compare to the measured bed level change?
As was mentioned before, the changes in the morphology of the coastal zone are the result of spacial variations in sand transport. The convergence and divergence of the total cross-shore sand transport results in bed level change. When a location gains sand, the bed level rises while the opposite happens at locations that loose sand. The bed level change during the field campaign was measured daily and will be compared to the gradients of the modelled total cross-shore transport.

3. Quantify the four different sand transport mechanisms during fair weather conditions at Vejers beach related to
(a) the transport of the waves Q_V related to non-linearities in wave velocity
(b) joint action of stirring of sand by waves and transport by currents Q_C
(c) the acceleration-driven transport Q_A
(d) the diffusive transport Q_D.
The aim of this research is to find the relative contribution of the acceleration-driven transport Q_A and the transport due to waves Q_V. The onshore directed transport by waves non-linearities (Q_V, Q_A) is partly balanced by the offshore directed transport by currents Q_C. The diffusive transport Q_D is also included to ensure that no unrealistic shapes develop in the modelled bed profile. The transport due to long waves is not included in this research project. The contribution of sand transport by long waves is only a small fraction of the total cross-shore transport when the long waves are small, which is the case during fair weather conditions (de Bakker et al., 2016).

In every chapter, the distinction between the research questions is made by separating the hydrodynamical model describing the water motion from the description of the sand transport mechanisms and the sand transport model. Chapter 2 starts with a conceptual description of a sandy uninterrupted coast and a detailed explanation of the wave non-linearities and the sand transport mechanisms, followed by the background theory for modelling the water motion, the sand transport and the bed level change. The material and methods can be found in Chapter 3, describing the field campaign, the set-up of the hydrodynamical model, the set-up of the sand transport model, the calibration methods and the set-up of the numerical experiments. The contribution of the different transport mechanisms to the total cross-shore transport is provided in Chapter 4 together with the calibration results and the comparison of the modelled and measured bed level change, followed by a discussion in Chapter 5 and the conclusions and recommendations for further research in Chapter 6.

Chapter 2: Theory

2.1 Background information

2.1.1 The coastal zone

The coastal zone is the interface of water and land where the sea interacts with the beach. A typical beach profile of a sandy uninterrupted coast can be seen in Figure 2.1. Waves enter

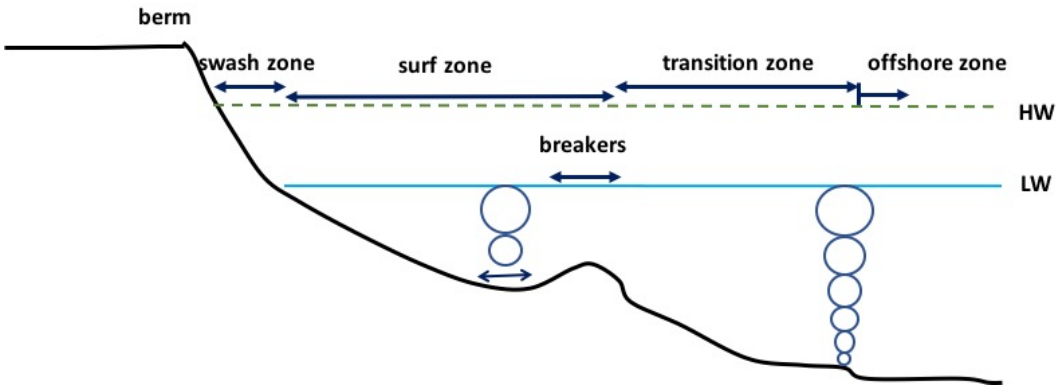

Figure 2.1 – A typical beach profile where the different zones are related to the wave dynamics. The circles indicate the wave orbital motion and the low water line (LW) as well as the high water line (HW) are indicated.

the coastal zone at the seaward boundary referred to as the offshore zone. The water is deep so the waves do not feel the bottom and have a perfect symmetric sinusoidal shape. Waves are observed as the rise and fall of the surface as a result of the oscillatory movement of the water particles. The circles in Figure 2.1 show the orbital motion of water particles due to waves, which starts to reach the bottom at the beginning of the transition zone where the water is shallower. The waves start to feel the bottom and the wave height starts to increase. This process is called shoaling and is related to the wave-energy. The group velocity of the waves, the velocity the energy is transported with, is depth-dependent and decreases with decreasing water depth. The energy density needs to increase to conserve the energy flux, resulting in an increase in the wave height and a decrease in the wavelength. The waves become skewed with peaked wave crests combined with longer and rounded wave troughs. An example of a skewed wave can be seen in blue in the middle panel of Figure 2.2, together with a symmetric wave (green, top panel) and an asymmetric wave (orange, bottom panel). Closer to the coast

the waves start to become more sawtooth shaped, which is determined by the asymmetry of the wave. The asymmetry of a wave is a measure of the acceleration of the water level. The crest height and duration of an asymmetric wave are equal to the trough depth and duration, but an asymmetric wave can not be mirrored in the crest or trough. There is an asymmetry in the duration of the fall and rise of the sea surface elevation: it takes more time to go from the maximum in the crest to the maximum in the trough compared to the time to go from the maximum in the trough to the maximum in the crest. In the beach profile, the waves become asymmetric above the sand bar and start to break. The region of the breaking waves is called the surf zone, after the foamy bubbly surface called surf that forms when waves break. The intertidal area is the part of the beach that is wet during high tide (HT) and dry during low tide (LT). This area is also called the swash zone, because it is only affected by the fore- and backwash of the waves. Sometimes the deposition of sand on the beach can form an almost horizontal plateau called a berm.

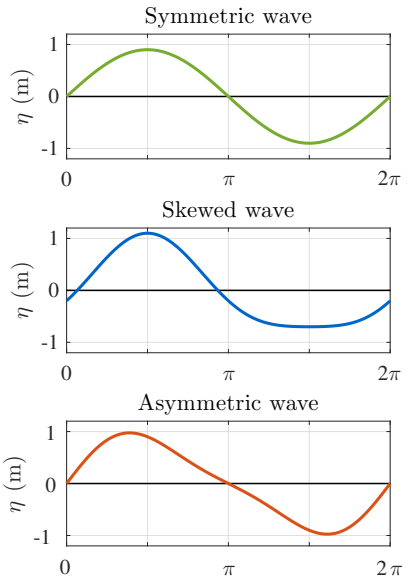

Figure 2.2 – The sea surface elevation η of a symmetric, a skewed and an asymmetric wave.

A beach profile usually consists of multiple bars. The bars can be located in the swash zone, called intertidal bars, or located in the subtidal part of the beach, called subtidal bars. When a sand bar is in the transition zone and followed by a deep trough, the waves start to shoal again after breaking above the bar crest. The waves become skewed and subsequently asymmetric until the waves break again in shallower water. The beach is usually not uniform in the alongshore direction. Alongshore variability can result in crescentic bars and drive alongshore currents (Masselink et al., 2014).

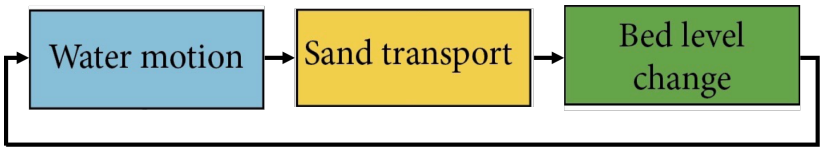

Figure 2.3 – Coastal dynamics is described by the interaction of the water motion, the sand transport and the bed level change.

Dynamics

Sand transport in a coastal system is the effect of a shear stress caused by the movement of water. Sand transport is the result of joint action of sand stirring by the waves to make the sand available for transport and the transport of available sand by the waves and currents. The bed profile changes due to spatial variation of the cross-shore sand transport. Bed level

changes influences the water motion by changing the water depth and the location of sand bars. These changes in the water motion effect the sand transport which subsequently alters the bed level change. The interaction of the water motion, sand transport and bed level change describe the dynamics of the coastal zone and is schematically shown in Figure 2.3.

2.1.2 Sand transport

Sand can be transported by currents, by the oscillatory wave motion of skewed and asymmetric waves or by the combination of waves and currents. The transport of sand depends on various sand properties, which will be described first, followed by the transport modes and the transport mechanism, respectively.

Sand properties

The grain size d_s is an important sand characteristic, which varies between 0.06 mm and 2 mm. A beach consists of many sand particles with different grain sizes, which can be determined by sieve analysis. The cumulative frequency curve of a sand sample is illustrated in Figure 2.4, where the percentage indicates what percent by weight of the total sample is finer than the grain size. The d_{50} of the sample is shown in orange and corresponds to the median, indicating that 50 percent by weight is finer and 50 percent is coarser (Fredsøe and Deigaard, 1992). The median grain size d_{50} is usually used in the sand transport equations to characterise the sand on the beach.

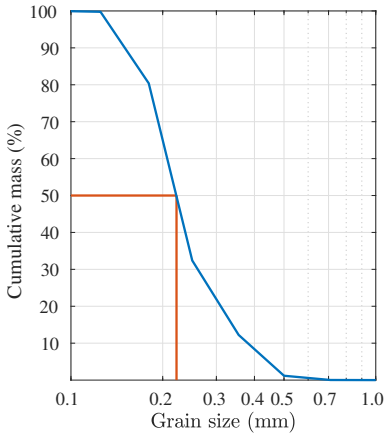

Figure 2.4 – An accumulation graph of a sand sample in blue with the medium grain size d_{50} of 0.22 mm indicated in orange.

The fall velocity W_S is the velocity with which suspended sand settles when the water is calm. Following Fredsøe and Deigaard (1992), the drag force F on a particle in a fluid is given by

$$F = \frac{1}{2} c_D \, \rho \, V^2 A \tag{2.1}$$

with c_D the drag coefficient, ρ the density of the fluid, V the relative velocity and A the area of the particle. The settling of a particle with diameter d is the result of the combined action of gravity and buoyancy, described by

$$(\rho_s - \rho) \, g \, \frac{\pi}{6} \, d^3 \tag{2.2}$$

with ρ_s the density of sand and g the gravitational acceleration. Under equilibrium conditions, the particle settles with the fall velocity W_S and the settling force is balanced by the drag force

$$(\rho_s - \rho) \, g \, \frac{\pi}{6} \, d^3 = \frac{1}{2} \, c_D \, \rho \, W_S^2 \, \frac{\pi}{4} \, d^2 \tag{2.3}$$

from which we can determine the fall velocity

$$W_S = \sqrt{\frac{4\,(s-1)g\,d}{3\,c_D}} \tag{2.4}$$

with s the specific gravity of sand, a variable that determines if a substance will float ($s < 1$) or sink ($s > 1$). The specific gravity of sand is 2.65. The drag coefficient c_D depends on the Reynolds number Re, which is the ratio of inertial forces to viscous forces inside the fluid. The drag coefficient c_D varies between 23 for a $Re = 1$ and 1.5 for $Re = 1000$. For sand particles in sea water the fall velocity W_S is around 2.5 cm/s, but the fall velocity increases for larger particles and a larger resistance of the water, determined by the grain diameter d and the drag coefficient c_D respectively.

The angle of repose ϕ is the largest declination angle a pile of material can make when the particles on the slope are not moving. It is essentially the angle a pile of sand makes without collapsing when a bucket of sand is emptied on a horizontal plane. The angle of repose is also called the friction angle and depends on the shape of the sand grains and the water content. Smooth, rounded sand grains have a smaller angle of repose compared to rough, irregular sand particles, because the frictional contact between smooth, rounded grains is smaller. The angle of repose of dry sand varies between 30° and 40° (Glover, 1989), but the angle of repose changes when water is added to the sand. When a small amount of water is added to sand, the friction angle increases to 45° (Glover, 1989), because the water forms a thin layer around the sand particles holding them together. When more water is added, the sand becomes oversaturated and is completely surrounded by water resulting in no frictional contact between the grains and a decrease of the angle of repose to 15-30° (Glover, 1989). The angle of repose for dry sand, wet sand and oversaturated sand is shown in Figure 2.5. The frictional angle determines how steep the bed profile can be and is important for the diffusive sand transport.

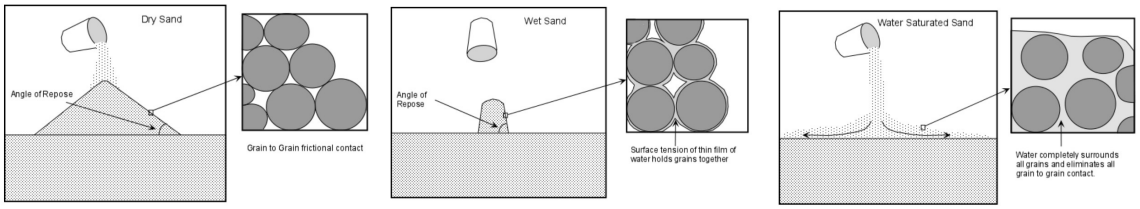

Figure 2.5 – The angle of repose for dry sand, wet sand and oversaturated sand. Adapted from Nelson (2013).

The threshold of grain movement and the transport modes

When water flows over a bed composed of grains, the grain particles experience driving forces trying to move the grain particles. The driving forces compete with the stabilizing force related to gravity. For slow flow velocities, the driving forces are not strong enough to move the particle from their equilibrium velocity, but when the flow velocity exceeds a certain

threshold the grain particle starts to move. This threshold velocity is called the critical flow velocity u_{*c}. Likewise, a critical shear stress τ_c can be defined, which is the force per unit area induced by the water flow to start sediment movement. The critical shear stress is related to the critical flow velocity by

$$\tau_c = \rho\, u_{*c}^2 \tag{2.5}$$

Shields (1936) determined the threshold of movement based on a ratio between the driving forces F_d and the stabilizing forces F_S. Figure 2.6 shows the force balance on a grain particle in case of a steady horizontal flow. The driving forces are the horizontal drag force F_D and the lift force F_L. The horizontal drag force is the result of friction on the surface of the grain and a pressure difference between the upstream and downstream side of the grain caused by flow separation (Fredsøe and Deigaard, 1992). The horizontal drag force on a grain particle with diameter d is given by

$$F_D = \frac{1}{2}\,\rho\, c_D\, \frac{\pi}{4}\, d^2\, U^2 \tag{2.6}$$

with U the horizontal flow velocity. A grain particle on the boundary disturbs the flow leading to deflection of the stream lines over the top of the grain particle (see Figure 2.6). This results in acceleration of the fluid over the top of the grain particle (Dyer, 1986) which causes a decrease in pressure according to Bernoulli's principle. The vertical pressure difference over the grain causes a lift force F_L,

$$F_L = \frac{1}{2}\,\rho\, c_L\, \frac{\pi}{4}\, d^2\, U^2 \tag{2.7}$$

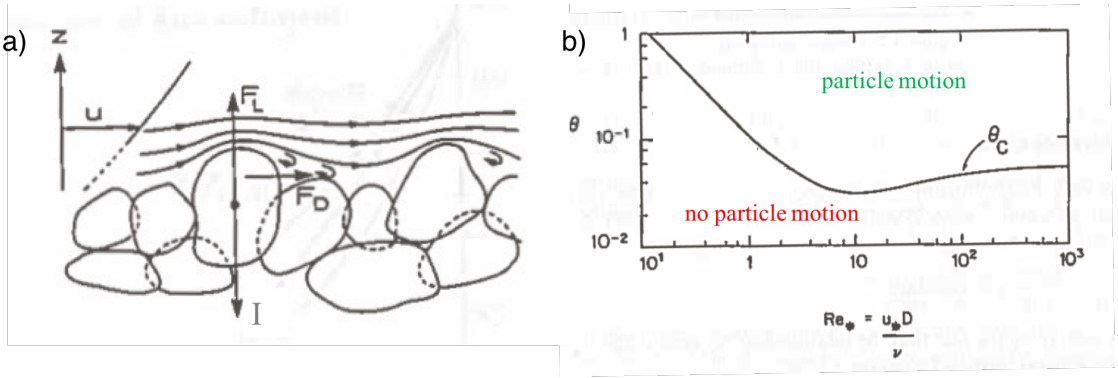

Figure 2.6 – (a) In case of steady flow over a bed, a grain particle at the boundary of the bed experiences a lift force F_L, a drag force F_D and a stabilizing force related to the immersed weight I. The directions of the forces are indicated by the arrows and the streamlines of the flow are shown as well. Adapted from Fredsøe and Deigaard (1992). (b) The Shields threshold curve showing the critical Shields parameter θ_c as a function of the grain Reynolds number Re. For Shield parameter θ larger than θ_c (curve), the grain particles start to move. Adapted from Dyer (1986).

with c_L the lift coefficient. Due to the similar expression for the drag force and lift force, the forces are combined in the total driving force,

$$F_d = \frac{1}{2}\,\rho\, c_D \frac{\pi}{4}\, d^2 (\alpha\, u_*)^2 \tag{2.8}$$

with u_* the friction velocity, c_D is the dimensionless drag and lift coefficient and $\alpha\, u_*$ is the friction velocity at the distance of the order of magnitude d from the bed.

The stabilizing force F_S is given by

$$F_S = \rho\, g(s-1)\, \frac{\pi}{6}\, d^3 \tan(\phi) = I \tan(\phi). \tag{2.9}$$

The submerged weight I is the difference between the force of gravity acting downwards and the buoyancy force acting upwards. The maximum friction between the grain and surrounding grains is measured by the factor $\tan(\phi)$ (Fredsøe and Deigaard, 1992).

The particles start to move when the friction velocity exceeds the critical friction velocity u_{*c}, which is determined by the balance of the driving force and stabilizing force

$$\frac{u_{*c}^2}{(s-1)g\, d} = \frac{4\mu_s}{3c_D\, \alpha} \tag{2.10}$$

The parameter on the left-hand-side is the critical Shields parameter θ_c,

$$\theta_c = \frac{u_{*c}^2}{(s-1)g\, d} = \frac{\tau_c^2}{\rho(s-1)g\, d} \tag{2.11}$$

Shields (1936) found a value of 0.05 for the constant on the right-hand-side of Equation (2.10), which depends weakly on the grain Reynolds number Re. The grain Reynolds number is defined as

$$Re = \frac{u_*\, d}{\nu} \tag{2.12}$$

with ν the kinematic viscosity of the fluid. The dependency of the critical Shields parameter on the Reynolds number is seen in the right panel of Figure 2.6, which shows the Shields threshold curve. When the Shields parameter θ exceeds the critical value θ_c (curve), the grain particles starts to move.

When the friction velocity u_* exceeds the critical friction velocity u_{*c}, sand is eroded from the bed and available for sand transport. The sediment starts to roll and bounce over the bed, which is called the bedload transport. The sediment is still in contact with the bed and responds fast to to changes in the velocity. The sand transport is calculated by multiplying the sand concentration by the flow velocity. In case of bedload, experimental data suggests that concentration of sediment is proportional to the shear stress τ (Wright et al., 1999), which is proportional to the velocity squared (Equation 2.5). Therefore, the bedload transport is proportional to the cube of the friction velocity,

$$\vec{Q_b} \propto \vec{u_*}^3. \tag{2.13}$$

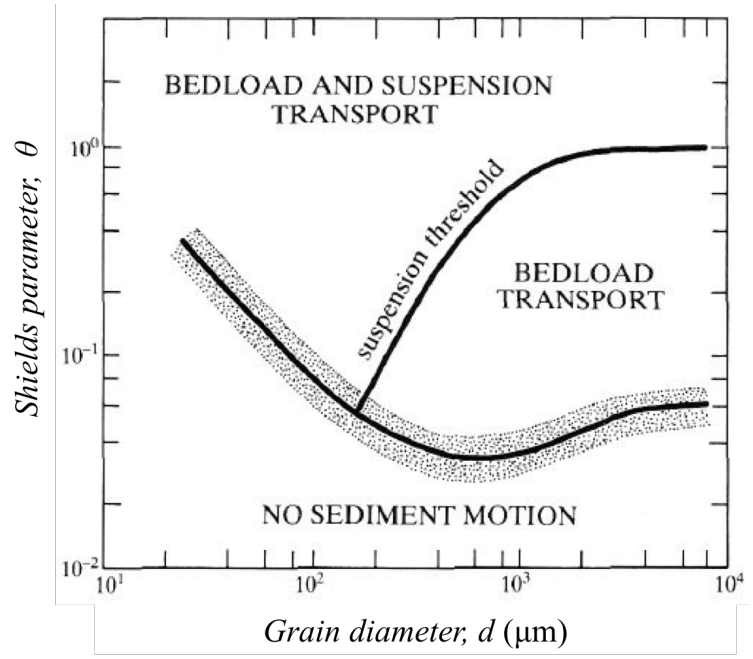

Figure 2.7 – The Shields parameter θ as function of the grain diameter d with the threshold of sediment motion and the suspension threshold. Adapted from Allen (1985)

When the friction velocity is approximately equal to the fall velocity of the particles ($W_S/u_* \sim 1$), the sediment is suspended and is no longer in contact with the bed. Once the particles are suspended, there is a competition between stirring by turbulent eddies to keep the sediment in suspension and settling of sediment due to gravity (van Rijn, 2013). The suspended sediment transport is obtained by integrating the flow velocity and the suspended sediment concentration over the whole water column,

$$\vec{Q}_s = \int \vec{u}(z)\, c(z)\, \mathrm{d}z. \tag{2.14}$$

Three different regimes are distinguished related to the transport of sediment, as illustrated in Figure 2.7. No sand transport takes place in the case that the Shields parameter is smaller than the threshold of sediment motion. Only bedload is transported when the Shields parameter is larger than the threshold of sediment motion, but smaller than the suspension threshold. When the Shields parameter exceeds the suspension threshold, both suspended sediment transport and bedload transport take place.

Transport mechanisms

As mentioned in the introduction, the sand is stirred by the waves and transported by the waves and currents. The dominant direction of the current in the coastal zone is offshore, related to the undertow. The sand is transported onshore by the non-linearities in the wave velocity and acceleration. For a symmetric wave, the onshore transport under the wave crest is balanced by the offshore transport under the wave trough, resulting in zero net transport over a wave period. In case of skewed and asymmetric waves, the transport under the crest

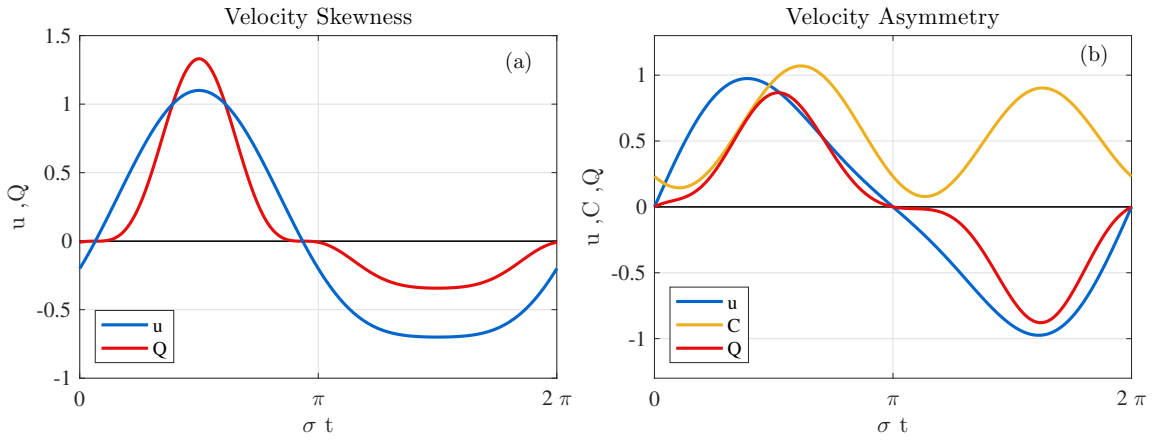

Figure 2.8 – (a) An example of the net onshore transport due to velocity skewness. The bedload transport is computed as $Q = \alpha u^3$ with $\alpha = 1$ s^2/m. (b) An example of the net onshore transport due to velocity asymmetry. The transport is computed by multiplying the velocity u by the concentration C.

is larger, leading to net onshore transport. A skewed wave shape results in a skewed velocity, and for this reason wave skewness is also called velocity skewness. The maximum flow velocity under the wave crest is higher than the maximum flow velocity under the trough. Therefore, more sand is transported under the wave crest, when the flow velocity is directed onshore (Ruessink et al., 2011). In Figure 2.8 the flow velocity of a skewed wave is plotted together with the bedload transport transport $Q = \alpha u^3$ with $\alpha = 1$ s^2/m. The transport under the crest is larger than the transport under the trough resulting in net transport in the onshore direction.

Asymmetric waves result in an asymmetric velocity. Sand is transported in the onshore direction, although the peak flow under the crest and the trough are the same for asymmetric waves. This is related to the local settling lag: it takes time to erode and settle fine suspended sediment. The local settling lag causes a time lag between the maximum in flow velocity u and the maximum sediment concentration C, as shown in Figure 2.8. The peak in the concentration due to the wave crest occurs early in the crest phase. Therefore, all the sand is transported during the crest phase. This is not the case for the peak concentration in the wave trough, which occurs at end of the trough phase. Not all sand stirred by the peak-trough velocity can be transported during the trough phase, some of the sediment is transported during the crest phase (Ruessink et al., 2011). The results is net transport in the onshore direction.

The fourth transport mechanism mentioned in the introduction was the diffusive transport, which accounts for the bed slope effects. The bed slope influences the threshold of sand movement and the bed slope may change the magnitude and/or direction of the transport (Fredsøe and Deigaard, 1992). The critical shear stress changes for grains on a bed with a slope, due to changes in the direction of the driving forces and the stabilizing force. The driving forces increase and the stabilizing force decreases, because the force related to gravity also has a horizontal component when the particle is on a slope. This results in a smaller

critical shear stress for particles on a bed with a slope compared to a bed with no slope. A bed load particle moves in a different direction than the flow in case of a slope perpendicular to the flow direction. The sand particles have the tendency to move downslope instead of in the flow direction.

Cross-shore distribution of the sand transport

Since the transport of sand depends on the hydrodynamics, it will change in the cross-shore direction. In deep water the waves are symmetric and do not feel the bottom resulting in no stirring and no transport of sand. When the waves start to feel the bottom in the transition zone, the sand is stirred by the orbital wave velocity indicated by the circles in Figure 2.1. The water is still quite deep in this zone, therefore the flow velocity at the bottom is small leading exclusively to bedload transport. At the end of the transition zone, just before the surf zone, the waves become skewed and transport is onshore directed. Above the bar and in the surf zone, the waves are asymmetric and start to break leading to an increase in the offshore directed current. The breaking waves stir sand. Therefore, a lot of sand is available for transport above the bar and in the surf zone. The transport under asymmetric waves is onshore directed and competes with the offshore sand transport by the undertow. Overall, the transport in the surf zone is onshore directed for a few breaking waves and offshore directed for many breaking waves.

2.2 Modelling waves and currents in the coastal zone

Water motion can be separated into currents, waves and turbulence. The spatial scale of a current ranges from 100 meters to a kilometre with a time scale of 10 minutes to an hour. Waves have a time scale of around 10 seconds with spatial scales from 1 to 10 meters. Turbulence, random oscillatory water motion, has a time scale smaller than 0.1 second and small spatial scales (1 mm to 1 cm).

There are two types of models used for modelling waves and currents in the sea that solve different temporal and spatial scales: phase-averaged models and phase-resolving models. Turbulence is not solved but parametrized in both types of models, because small spatial and temporal scales are necessary to solve turbulence. In the phase-averaged models, for example Delft3D (Lesser et al., 2004) and SWAN (Booij et al., 1999), the turbulence and the waves are averaged. The models include equations for the currents combined with equations for the phase averaged properties of waves, i.e. the frequency, wave number, wave angle and wave energy. The statistics of the sea surface are computed, which means that for every grid point the energy spectra are computed. This type of model is used for larger domains and deep to intermediate water depths. In shallow water and close to the shore, phase-resolving models are used, like the Boussinesq models (Boussinesq, 1872) and the SWASH model (Zijlema et al., 2011). In these models, the waves are resolved instead of using the statistical properties of the waves, since the sea surface is computed as a function of distance and time. The phase-resolving models can only be used on a smaller domain, because the model grid needs to be fine enough to solve all wavelengths.

The Boussinesq models only work in relative shallow water when the water depth is small compared to the wave length, because the models are based on the depth-integrated wave equations and do not resolve the vertical. The vertical is resolved by the SWASH model (Zijlema and Stelling, 2005; Zijlema et al., 2011), which is faster and more powerful than other Boussinesq-type wave mode. For these reasons, the SWASH model is used in this research project to model the waves and currents in the coastal zone. The SWASH model is based on the non-linear shallow water equations, which are applicable in the case of

- *quasi-shallow water:* In case of shallow water, the horizontal length scale L is assumed to be much greater than the vertical length scale H: $L \gg H$. Because the SWASH model also resolves the vertical, it is applicable in slightly deeper waters, hence the term quasi-shallow water.

- *the density of water ρ is constant:* In case of a constant water density, the continuity equation reduces to

$$\nabla \cdot \vec{u} = \frac{\partial u}{\partial x} + \frac{\partial v}{\partial y} + \frac{\partial w}{\partial z} = 0, \tag{2.15}$$

  with the total velocity vector $\vec{u} = (u, v, w)$, where u and v are the horizontal velocity components in the x and y direction, and w is the vertical velocity in the z direction. Scaling the continuity and using $L \gg H$ it follows that vertical velocity is much smaller than the horizontal velocities: $u, v \gg w$.

- *the water motion is quasi-hydrostatic:* The pressure p in the water can be split in the hydrostatic pressure p_h and non-hydrostatic pressure q: $p = p_h + q$. The hydrostatic pressure is described by the hydrostatic balance

$$\frac{\partial p_h}{\partial z} = -\rho g. \tag{2.16}$$

  The hydrostatic pressure is the pressure exerted by the fluid in equilibrium due to the force of gravity. The vertical accelerations in the fluid are forced by the horizontal divergence of the velocity field (Equation 2.15) and the non-hydrostatic pressure, e.g. the acceleration due to orbital wave motion is the result of the wave-induced pressure.

The Coriolis force is neglected in the SWASH model, which is justified in case of small length and time scales. The length scale on which rotation becomes important is given by the Rossby radius of deformation R, which is the ratio of the phase speed in shallow water and the Coriolis parameter f. The Coriolis parameter f is related to the Earth's rotation rate Ω and the latitude φ as $f = 2\pi\Omega \sin(\varphi)$, which has a typical value of 10^{-4} s^{-1}. The Rossby radius of deformation for a water depth of 10 m is

$$R = \frac{\sqrt{gh}}{f} = \frac{\sqrt{9.81 \cdot 10}}{10^{-4}} \approx 10 \text{ km}.$$

Currents, the type of water motion with the largest spatial scale, are usually smaller than 1 km in the coastal zone. Therefore, the Coriolis force can be neglected.

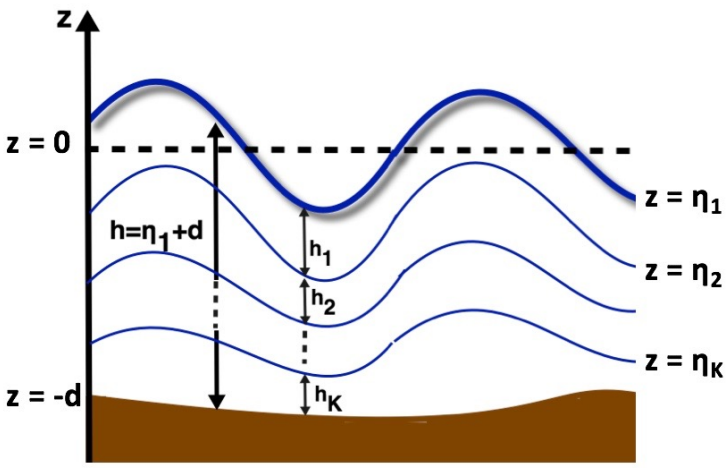

Figure 2.9 – The layered model of the sea where the upper surface of layer k is given by $z = \eta_k$ and the thickness of the layer is given by h_k. The total water depth h is the sum of the sea surface elevation of the top layer η_1 and the still water depth d.

2.2.1 Governing equations

The SWASH model considers K different layers with varying thickness h_k. The index k refers to the number of the layer, with $k = 1$ the top layer and $k = K$ the bottom layer. The upper surface of each layer is given by $z = \eta_k$, which is shown in Figure 2.9. The total water depth h is the sum of the still water depth d and the sea surface elevation η_1. The upper surfaces η_k are a function of the horizontal coordinates x and y, the vertical coordinate z and the time t. In each layer, the layer-averaged horizontal velocities u_k and v_k are computed, together with the layer-averaged hydrostatic pressure p_k, the layer-averaged non-hydrostatic pressure q_k and the layer-averaged vertical velocity w_k.

The continuity equation

In shallow water, the continuity equation in layer k is given by

$$\frac{\partial \eta_k}{\partial t} - \frac{\partial \eta_{k+1}}{\partial t} + \frac{\partial}{\partial x}\left(h_k\, u_k\right) + \frac{\partial}{\partial y}\left(h_k\, v_k\right) = 0, \tag{2.17}$$

with $h_k = (\eta_k - \eta_{k-1})$ is the depth of layer k. For the bottom layer ($k = K$), the term η_{k+1} equals the still water depth d. The continuity equation describes the conservation of mass.

The horizontal momentum equations

The non-linear quasi-shallow water momentum equations are obtained by vertically integrating the Navier-Stokes equation,

$$\frac{\partial \vec{u}}{\partial t} + \left(\vec{u} \cdot \nabla\right) \vec{u} = -\frac{1}{\rho}\nabla p + \vec{g} + \frac{1}{\rho}\nabla \cdot \boldsymbol{\tau}, \tag{2.18}$$

where p is the total pressure in the fluid and $\boldsymbol{\tau}$ is the deviatoric stress tensor. The terms on the left-hand side are the inertial forces consisting of the local time derivative of the velocity

vector and the advection term. The forcing terms on the right-hand side are the pressure gradient, the body force due to gravity and the viscous forces related to the rate of change of deformation over time, respectively.

Vertically integrating Equation 2.18 for each layer results in the non-linear quasi-shallow water momentum equations for a layer-averaged, quasi-hydrostatic, free-surface flow, which are based on the equations of Zijlema et al. (2011).

$$\frac{\partial u_k}{\partial t} + u_k\frac{\partial u_k}{\partial x} + v_k\frac{\partial u_k}{\partial y} + g\frac{\partial(\eta_k - \eta_{k+1})}{\partial x} + \frac{1}{h_k}\int_{\eta_{k+1}}^{\eta_k}\frac{\partial q}{\partial x}\,\mathrm{d}z = \frac{1}{h_k}\left(\tau_{\eta_k,x} - \tau_{\eta_{k+1},x}\right) + \frac{1}{h_k}\left(\frac{\partial h_k\,\tau_{xx,k}}{\partial x} + \frac{\partial h_k\,\tau_{xy,k}}{\partial y}\right), \tag{2.19}$$

$$\frac{\partial v_k}{\partial t} + u_k\frac{\partial v_k}{\partial x} + v_k\frac{\partial v_k}{\partial y} + g\frac{\partial(\eta_k - \eta_{k+1})}{\partial y} + \frac{1}{h_k}\int_{\eta_{k+1}}^{\eta_k}\frac{\partial q}{\partial y}\,\mathrm{d}z = \frac{1}{h_k}\left(\tau_{\eta_k,y} - \tau_{\eta_{k+1},y}\right) + \frac{1}{h_k}\left(\frac{\partial h_k\,\tau_{yx,k}}{\partial x} + \frac{\partial h_k\,\tau_{yy,k}}{\partial y}\right), \tag{2.20}$$

where $\vec{\tau_{\eta_k}}$ is the stress on the upper surface of layer k, $\vec{\tau_{\eta_{k+1}}}$ is the stress on the bottom surface of layer k, and $\tau_{xx,k}, \tau_{xy,k}, \tau_{yx,k}$ and $\tau_{yy,k}$ are the horizontal turbulent stresses of layer k. The first three terms in the momentum equations are the advection terms, followed by the hydrostatic pressure forcing and the integral of the non-hydrostatic pressure gradient, which will be solved in the next section. The first term on the right hand side of the momentum equations is the stress that is exerted on layer k by the adjacent layers $(k+1,\ k-1)$ and the last term is related to the horizontal turbulent stresses.

The hydrostatic pressure forcing term is derived by vertically integrating the hydrostatic balance (Equation 2.16) over layer k.

$$\int_{\eta_{k+1}}^{\eta_k} p_h\,\mathrm{d}z = \int_{\eta_{k+1}}^{\eta_k}\rho g\,\mathrm{d}z \tag{2.21}$$

$$p_h|_{z=\eta_k} - p_h|_{z=\eta_{k+1}} = \rho g(\eta_k - \eta_{k+1}). \tag{2.22}$$

Since the hydrostatic pressure depends linearly on the vertical coordinate z, the layer averaged hydrostatic pressure p_k is defined as,

$$p_k = \frac{1}{2}(p_h|_{z=\eta_k} - p_h|_{z=\eta_{k+1}}) = \frac{1}{2}\rho g(\eta_k - \eta_{k+1}), \tag{2.23}$$

The Navier-Stokes equation included the gradient of the pressure, which in case of the vertically integrated quasi-shallow water equations becomes

$$\frac{1}{\rho}\nabla p_k = \frac{1}{2}g\nabla(\eta_k - \eta_{k+1}) \tag{2.24}$$

which is the fourth term in the momentum equations (Equation 2.19 and Equation 2.20).

The adjacent layers ($k+1,\ k-1$) exert a stress on layer k, indicated by $\vec{\tau_{\eta_k}}$ and $\vec{\tau_{\eta_{k+1}}}$. For the top layer ($k=1$), the stress $\vec{\tau_{\eta_1}}$ equals the wind shear stress $\vec{\tau_w}$, which is related to the wind speed at 10 m height $\vec{U}_{10}$ as

$$\vec{\tau}_w = \rho_{air}\ C_d\ \vec{U}_{10}|\vec{U}_{10}| \tag{2.25}$$

with ρ_{air} the density of air and C_d the dimensionless drag coefficient. For the bottom layer ($k=K$), the stress $\vec{\tau_{\eta_{K-1}}}$ equals the bottom stress $\vec{\tau}_b$, which accounts for bottom friction. The bottom stress $\vec{\tau}_b$ is given by

$$\vec{\tau}_b = c_f\,\vec{u_K}|\vec{u_K}| \tag{2.26}$$

where c_f is dimensionless bottom friction coefficient and $\vec{u_K} = (u_K, v_K)$ is the layer-averaged horizontal velocity of the bottom layer. The dimensionless bottom friction coefficient c_f is related to the total water depth through the Manning's roughness coefficient n as,

$$c_f = \frac{n^2 g}{h^{1/3}} \tag{2.27}$$

When waves break, turbulence is generated resulting in turbulent fluctuations in the momentum equations. This is included in the last term of the momentum equations through the turbulent stresses. The horizontal eddy viscosity ν_t accounts for the turbulent mixing and dissipation caused by wave breaking and determines the scale at which dissipation due to wave breaking takes place. (Zijlema et al., 2011). The horizontal turbulent stresses are related to the depth-averaged horizontal velocities and the horizontal eddy viscosity as

$$\tau_{xx,k} = 2\nu_t \frac{\partial u_k}{\partial x}, \quad \tau_{xy,k} = \tau_{yx,k} = \nu_t \left(\frac{\partial v_k}{\partial x} + \frac{\partial u_k}{\partial y} \right), \quad \tau_{yy,k} = 2\nu_t \frac{\partial v_k}{\partial y}.$$

Equations for the non-hydrostatic pressure and the vertical velocity

To obtain a set of closed equations for the five variables u_k, v_k, p_k, q_k and w_k, two additional equations are needed. An expression for the integral over the gradient of the non-hydrostatic pressure in the momentum equations is needed, as well as an equation to calculate the vertical velocity. Firstly, a derivation of the integral over the gradient of the non-hydrostatic pressure is shown for the x direction (it works similar in the y direction). Using Leibniz' rule of integration, the integral can be written as

$$\int_{\eta_{k+1}}^{\eta_k} \frac{\partial q}{\partial x}\ \mathrm{d}z = \frac{\partial}{\partial x} \int_{\eta_{k+1}}^{\eta_k} q\ \mathrm{d}z - q|_{z=\eta_k} \frac{\partial \eta_k}{\partial x} - q|_{z=\eta_{k+1}} \frac{\partial \eta_{k+1}}{\partial x} \tag{2.28}$$

Following Stelling and Zijlema (2003), the integral is approximated by

$$\int_{\eta_{k+1}}^{\eta_k} q\ \mathrm{d}z \approx \frac{1}{2} h_k \left(q|_{z=\eta_k} + q|_{z=\eta_{k+1}} \right) \approx \frac{1}{4} h_k\, q_k, \tag{2.29}$$

which can be used to determine the layer-averaged non-hydrostatic pressure q_k. Combining Equations (2.28) and (2.29), results in

$$\int_{\eta_{k+1}}^{\eta_k} \frac{\partial q}{\partial x}\ \mathrm{d}z \approx \frac{1}{2} \frac{\partial}{\partial x} \left(h_k \left[q|_{z=\eta_k} + q|_{z=\eta_{k+1}} \right] \right) - q|_{z=\eta_k} \frac{\partial \eta_k}{\partial x} - q|_{z=\eta_{k+1}} \frac{\partial \eta_{k+1}}{\partial x}. \tag{2.30}$$

Applying the Keller-box method (Lam and Simpson, 1976):

$$\frac{q_k|_{z=\eta_k} - q|_{z=\eta_{k+1}}}{h_k} = \frac{1}{2}\frac{\partial q}{\partial z}|_{z=\eta_k} + \frac{1}{2}\frac{\partial q}{\partial z}|_{z=\eta_{k+1}}. \tag{2.31}$$

The vertical velocity at the upper surface of the layer w_{η_k} and the bottom surface of the layer $w_{\eta_{k+1}}$ are described by the vertical momentum equation, given by

$$\frac{\partial w_{\eta_k}}{\partial t} + \frac{\partial q}{\partial z}|_{z=\eta_k} = 0 \; ; \qquad \frac{\partial w_{\eta_{k+1}}}{\partial t} + \frac{\partial q}{\partial z}|_{z=\eta_{k+1}} = 0. \tag{2.32}$$

Combing the vertical momentum equations with Equation (2.31) results in

$$\frac{\partial w_{\eta_k}}{\partial t} + \frac{\partial w_{\eta_{k+1}}}{\partial t} = \frac{2}{h_k}\left(q|_{z=\eta_k} - q|_{z=\eta_{k+1}}\right). \tag{2.33}$$

Secondly, to solve the non-hydrostatic pressure, an additional equation for the vertical velocity is needed. The vertical velocity at the top and bottom of the layer can be determined from the continuity equation

$$\nabla \cdot \vec{u} = 0 \quad \rightarrow \quad \frac{\partial u_k}{\partial x} + \frac{\partial v_k}{\partial y} + \frac{w_{\eta_k} - w_{\eta_{k+1}}}{h_k}. \tag{2.34}$$

The kinematic boundary condition at the bottom layer $k = K$ is given by

$$w_{\eta_{k+1}} = -u_k \frac{\partial d}{\partial x} - v_k \frac{\partial d}{\partial y} \quad \text{on} \quad z = -d. \tag{2.35}$$

When the horizontal layer-averaged velocities are known, the vertical velocity at the upper surface of the layers can be found using the kinematic boundary condition and Equation (2.34). The boundary condition at the upper surface is given by the non-hydrostatic pressure, which equals zero on the sea surface:

$$q = 0 \quad \text{on} \quad z = \eta_1. \tag{2.36}$$

Once the vertical velocities on the surfaces are known, Equation (2.33) can be used to compute the non-hydrostatic pressure at the bottom surface of the top layer and subsequently the non-hydrostatic pressure at all the surfaces. Using the non-hydrostatic pressure at all the surfaces, the integral in the momentum equations can be computed using Equation 2.30.

2.2.2 Boundary conditions

Waves enter the model domain at the seaward boundary. A random wave field is generated using two statistical distributions of wave characteristics. The Rayleigh distribution is used to describe the occurrence of various wave heights in the wave field and the JONSWAP spectrum is used to determine how the energy is distributed over the wave frequencies.

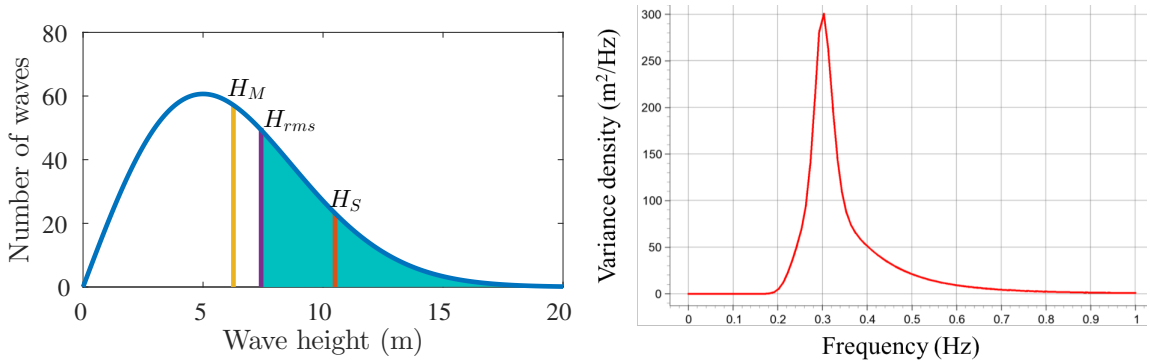

Figure 2.10 – (a) A Rayleigh distribution of wave heights with the mean wave height H_M, the root-mean square wave height H_{rms} and the significant wave height H_S. The coloured area indicates the highest one-third of the waves. (b) The JONSWAP spectrum for a peak frequency of 0.3 Hz and $\alpha = 0.081$.

The Rayleigh distribution of wave heights

In a random wave field, the waves have various wave heights. The individual wave heights follow a Rayleigh distribution (Holthuijsen, 2007), which is shown by the blue curve in Figure 2.10. The coloured area indicates the highest one-third of waves and is used to determine the significant wave height H_S, which is defined as the mean of the highest one-third of waves in the wave record. The mean wave height H_M, the mean over all waves, and the significant wave height H_S are indicated in yellow and orange respectively. Using the Rayleigh distribution, the significant wave height can easily be calculated from the standard deviation SD of a time series of the sea surface elevation η,

$$H_S = 4\ SD(\eta). \tag{2.37}$$

The SWASH model inverts this procedure and creates a time series of the sea surface elevation at the seaward boundary using only the significant wave height H_S as an input variable.

The wave energy is proportional to the root-mean-square wave height H_{rms}, defined as

$$H_{rms} = \left(\frac{1}{N} \sum_{i=1}^{N} H_i^2 \right)^{1/2},$$

with N the total number of waves in the time series and the index i indicates the number of the measured wave in a time series, so $i = 1$ corresponds to the first wave measured. The root-mean-square wave height H_{rms} is plotted in purple in Figure 2.10 and is related to the significant wave height H_S by $H_{rms} = \frac{1}{2}\sqrt{2}H_S$ (Holthuijsen, 2007).

The JONSWAP wave spectrum

A fast Fourier transform of a times series of the sea surface elevation is used to obtain the variance density spectrum, which shows the distribution of the power over the different frequencies. From the variance density spectra, the peak frequency f_p can be determined,

which is the frequency with the highest energy density. In the SWASH model, the peak frequency is used to create a variance density spectrum. This is done by using the JONSWAP spectrum, which describes how the energy is distributed over the various wave frequencies. Hasselmann et al. (1973) determined the variance density spectrum at various distances from the coast during the JOint North Sea WAve Project (JONSWAP). It was observed that the wave spectrum is never fully developed due to non-linear wave-wave interactions. The spectrum is limited by the fetch, which is the length of water over which the wind has blown. The variance energy density E described by the JONSWAP spectrum is given by

$$E(\sigma) = \alpha g^2 f^{-5} \exp\left[\frac{-5}{4}(\frac{f}{f_p})^{-4}\right] \gamma^{\exp\left[-\frac{(f-f_p)^2}{2(f_p/s)^2}\right]} \tag{2.38}$$

where the peak enhancement factor γ is 3.3, α determines the total variance of the wave field and the bandwidth of peak enhancement s is 0.07 for frequencies is smaller than the peak frequency f_p and 0.09 for frequencies larger than f_p. The JONSWAP spectrum is illustrated in Figure 2.10 for a peak frequency of 0.3 Hz and $\alpha = 0.081$.

Combining the Rayleigh distribution and the JONSWAP distribution, the SWASH model creates a random wave field using only two input variables: the wave height (H_S or H_{rms}) and the peak period T_p, which is the inverse of the peak frequency. Figure 2.11 shows an example of a time series of the sea surface elevation η created by the SWASH model.

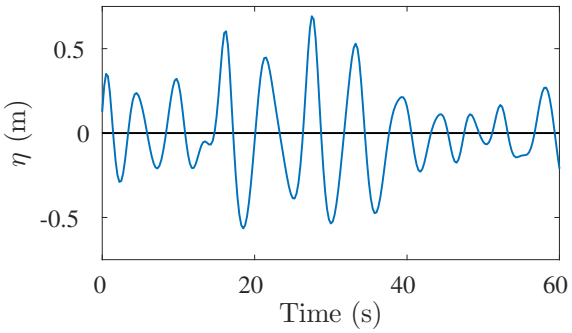

Figure 2.11 – An example of a time series of the sea surface elevation η created by the SWASH model using a significant wave height H_S of 1 m and a peak period T_p of 6 seconds.

2.2.3 Coupling between the water motion and the sand transport equations

This section explains how the wave velocity and mean current (variables necessary to calculate the sand transport) are determined from the output of the SWASH model. The SWASH model calculates the layer-averaged horizontal velocities u_k and v_k. Only the cross-shore sand transport is computed in this research product, as mentioned in the introduction. Therefore, the SWASH model is used in the 1D setting, which means that v_k is set equal to zero everywhere.

The coupling between the water motion modelled by the SWASH model and the sand transport model is schematically shown in Figure 2.12 As described in the background information, the friction velocity is an important variable for the moving and stirring of sand. For that reason, the velocity of the bottom layer ($k = K$) is used to calculate the sand transport. The current U_C is calculated by taking the time average over 30 minutes of the total velocity U_t, which equals the layer-averaged velocity of the bottom layer u_K. The wave velocity U_W is defined as the difference between the total velocity and the current

$$U_t = U_C + U_W \quad \text{with} \quad U_C = \langle U_t \rangle \tag{2.39}$$

where the brackets $\langle\rangle$ indicate the time average over 30 minutes. The wave velocity is split in a velocity contribution by the long waves, also called low-frequency waves or infragravity waves, and the short waves, also called high-frequency waves. The low-frequency wave velocity U_{LF} and the high-frequency wave velocity U_{HF} are determined using a fast Fourier transform filter. The frequencies between 0.005 and 0.05 Hz are defined as those of the low frequency waves and the frequencies between 0.05 Hz and 1 Hz are defined as those of high frequency waves.

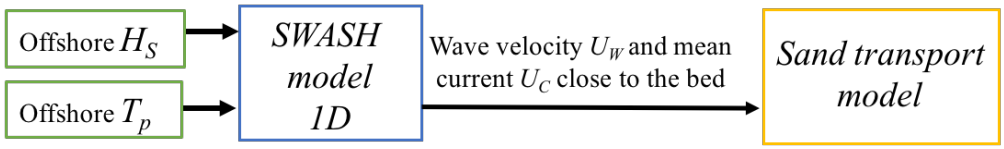

Figure 2.12 – Schematic view of the coupling between the water motion modelled by the SWASH model and the sand transport model, with the significant wave height H_S and the peak period T_p.

2.3 Sand transport equations

From the SWASH model, the wave-velocity and the current close to the bed are obtained. To calculate the sand transport, the concentration of sand in the water column is needed. The sand transport models use a parametrization of the concentration, which is usually based on the flow velocity. The first attempts to model the onshore sand transport and sandbar migration were based on models using the bottom stress. The sediment transport rate was determined from the bottom shear stress using, for example, the Meyer-Peter Mueller power law (Ribberink, 1998), which gives a relation between the sediment transport rate and the Shields parameter. The time-averaged sediment transport rate has a velocity U dependency between U^3 and U^4. The onshore sand bar migration was not predicted by those early models because the total velocity (current + wave velocity) was used (Roelvink and Stive, 1989; Gallagher et al., 1998). Hsu et al. (2006) were able to model the onshore sandbar migration using an energetics model that separates the transport associated with solely the orbital wave velocities from the transport by the mean current, which also includes the interaction with the oscillatory current. However, the transport by the orbital velocities did not include the acceleration-driven transport. Dubarbier et al. (2015) adapted the model of Hsu et al. (2006)

by adding the acceleration-skewness induced transport. However, they also combined the transport of currents and waves again and separated the transport in bedload and suspended load transport. Since we are interested in the transport rate by the different mechanisms, it is useful to separate the transport by the wave orbital velocity from the transport associated with the mean current. Fernández-Mora et al. (2015) used the sediment transport description given by Hsu et al. (2006) for the transport due to waves and the transport due to currents, which is complemented by the acceleration-skewness transport based on the model of Hoefel and Elgar (2003). Fernández-Mora et al. (2015) also added the diffusive sediment transport to the model to include the effect of the bed slope and to avoid the development of unrealistic bedforms.

In this research project the formulas of Fernández-Mora et al. (2015) are used because it separates the effect of transport by currents, wave skewness and wave asymmetry. The formulas are only applicable in the case of alongshore uniformity. It is assumed that the alongshore currents are small, and therefore they are not included in the sand transport formulas. The threshold of sediment movement, for example the critical shear stress or the critical friction velocity, is not included in the formulas adapted from Hsu et al. (2006), which means that sediment starts to move at a low flow velocity. A threshold acceleration is included in the skewness-acceleration transport. Fernández-Mora et al. (2015) neglects the settling lag effects, which means that transport related to advection by the Stokes drift is not included as was done in Henderson and Allen (2004). The sand transport formulas are shown in the next subsections for each of the four mechanisms separately.

2.3.1 Transport by the waves

The sand transport by the waves Q_V is related to the velocity skewness mechanism. The sand is stirred by the high frequency wave velocity and transported by the high frequency waves. The transport by the waves is given by

$$Q_V(x) = \frac{C_W}{(s-1)g}\left[\frac{\epsilon_B}{\tan\phi}\left\langle |U_{HF}(x,t)|^2\, U_{HF}(x,t)\right\rangle + \frac{\epsilon_S}{W_S}\left\langle |U_{HF}(x,t)|^3\, U_{HF}(x,t)\right\rangle\right] \quad (2.40)$$

with the transport efficiency factors for bed-load ϵ_B and suspended sediment ϵ_S, set to 0.015 and 0.135, and the wave friction coefficient C_W is determined by calibration. The first term between the brackets is the bed-load transport, proportional to the third power of the velocity, and the second term is the suspended sand transport, proportional to the fourth power of the velocity. The bedload transport is related to the friction angle, which is set to 16.7 ° in which case the $\tan(\phi)$ equals 0.3. The low value of the friction angle is used because sand on the sea bed is oversaturated by the surrounding seawater. The concentration of the suspended load depends on the fall velocity. Therefore, the parametrization of the suspended sand transport includes the fall velocity.

2.3.2 Acceleration skewness

The acceleration-driven transport Q_A is related to the acceleration skewness mechanism. The flow acceleration a is defined as the total time derivative of the total flow velocity U_t

$$a = \frac{dU_t}{dt}. \tag{2.41}$$

This acceleration-driven transport is given by,

$$Q_A = \begin{cases} K_a(a_{spike} - sign(a_{spike})a_{cr}), & a_{spike} \geq a_{cr} \\ 0, & a_{spike} < a_{cr} \end{cases} \tag{2.42}$$

with a_{cr} the threshold acceleration and K_a is a calibration constant (in m s) that accounts for the contribution of both bed load and suspended load. The term a_{spike} is related to the acceleration skewness and calculated from the acceleration:

$$a_{spike} = \frac{\langle a(t)^3 \rangle}{\langle a(t)^2 \rangle}.$$

Net sand transport by the wave acceleration occurs when the acceleration skewness a_{spike} is larger than the threshold acceleration a_{cr}, which is set to 0.5 m/s^2 following Fernández-Mora et al. (2015).

2.3.3 Transport by currents

The transport due to the current Q_C is usually offshore directed, because the undertow is offshore directed. The transport equation is quite similar to the sand transport by the waves. The sand is stirred by the total velocity, so the wave stirring by the waves is included. Once the sand is available, only the transport by the current U_C is computed. The transport equation of sand by currents is given by,

$$Q_C(x) = \frac{C_C}{(s-1)g} \left[\frac{\epsilon_B}{\tan\phi} \left\langle |U_t(x,t)|^2 \right\rangle U_C(x) + \frac{\epsilon_S}{W_S} \left\langle |U_t(x,t)|^3 \right\rangle U_C(x) \right] \tag{2.43}$$

with C_C the current friction coefficient, which is determined by calibration.

2.3.4 The diffusive transport

The diffusive transport Q_D makes sure that no unrealistic shapes are formed in the bed profile. Sand has the tendency to move downslope and the slope of the bed profile (dz_b/dx, with z_b the bed height) has a maximum related to the friction angle. The diffusive transport Q_D is given by,

$$Q_D = \lambda_d \, \nu(x) \left(\frac{1}{\tan\phi - dz_b/dx} \right) \left(\frac{dz_b/dx}{\tan\phi} \right) \tag{2.44}$$

where λ_d is a calibration constant. The function $\nu(x)$ is modified from the expression of Fernández-Mora et al. (2015) into

$$\nu(x) = H_{rms} \left(\frac{D_w}{\rho_s} \right)^{1/3}.$$

with D_w the wave dissipation. The diffusive transport accounts for the bed slope effects, which are large over the steep bottoms in the breaking zone (Fernández-Mora et al., 2015). The function $\nu(x)$ enhances the diffusive transport at the location of wave breaking, because this is the location with the highest wave height H_{rms} and most energy dissipation due to wave breaking D_w. The energy dissipation is calculated following Thornton and Guza (1983):

$$D_w = \frac{3B^3\rho g}{32\sqrt{\pi}\gamma_b^2}\frac{\sigma H_{rms}^5}{d^3}\left(1-\left[1+\left(\frac{H_{rms}}{\gamma_b d}\right)^2\right]^{-2.5}\right)$$

where d is the still water depth, B describes the type of wave breaking and γ_b is the critical value of the normalised wave height. The parameters B and γ_b are set so that $B^3 = 1.1$ and γ_b=0.5, which are the values Fernández-Mora et al. (2015) used for wave heights below 1.5 m.

2.4 Bed evolution

The four transport mechanisms are combined to obtain the total cross-shore transport Q_{tot},

$$Q_{tot} = Q_V + Q_A + Q_C + Q_D \tag{2.45}$$

The gradient of the total cross-shore transport is used to determine the change in the bed height z_b following Fernández-Mora et al. (2015),

$$(1-p)\frac{\partial z_b}{\partial t} + \frac{\partial Q_{tot}}{\partial x} = 0 \tag{2.46}$$

with p the porosity of sand. This equation for the cross-sediment transport only holds in case of alongshore uniformity. The porosity p is a measure for the packing of grains, which affects the stability of the grains located at the boundary of the bed (Dyer, 1986). It is harder to move a grain particle when the sand is densely packed compared to the case when the sand is more loosely packed. The porosity is included in the bed level change equation, because the state of packing also affects the way the sediment is deposited. Denser packing of sand deposition occurs when the bed is subject to wave and current activity, compared to a looser packing when the sand settles from suspension in calm water (Dyer, 1986). The porosity is set to 0.4 following Fernández-Mora et al. (2015).

Chapter 3: Material and methods

3.1 Field campaign

Field data were collected during a campaign by Utrecht University in collaboration with the University of Copenhagen, in autumn 2016 at Vejers beach in Denmerk. Vejers beach is located at the Danish North Sea coast (see Figure 3.1). The average annual offshore significant wave height is $H_S = 1.3$ m with a mean wave period $T = 4 - 5$ s, but during storms the wave heights can be up to $H_S = 6.5$ m with periods in excess of 10 s. Vejers beach has a semi-diurnal tide with a spring tidal range of 1.2 m (Aagaard et al., 2013) and a neap tidal range of 0.6 m (Jensen et al., 2009). The slope of the swash zone is generally steep with a mean slope of approximately 0.026 (Jensen et al., 2009) compared to a slope of around 0.008 in the surf zone and transition zone (Aagaard et al., 2013). Following the Australian beach state model of Wright and Short (1984), the beach state of Vejers is classified as intermediate (Aagaard et al., 2013). The beach profile of Vejers beach consists of three or four sand bars, with generally steep landward and seaward slopes (Aagaard, 2011; Aagaard et al., 2013). The troughs between the bars are relatively deep and the height difference between the bar crest and trough can be up to 3 m. This means that after the waves break due to the shallow water above the bar, they can re-shoal again in the trough (Aagaard, 2011). Jensen et al. (2009) reported a mean grain size in the swash zone of 230 μm, while Aagaard (2011) reported a

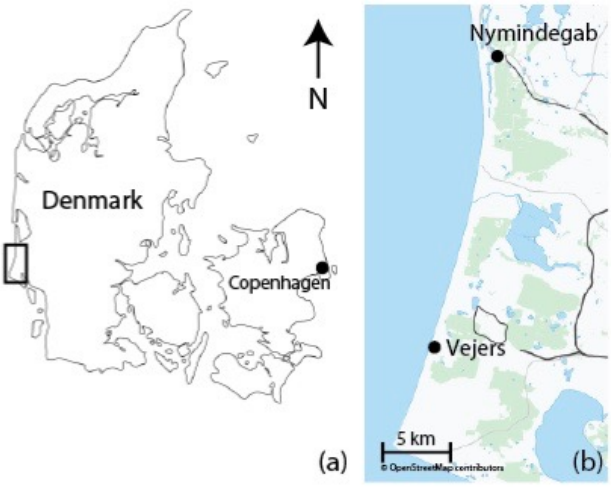

Figure 3.1 – **(a)** The study site in Denmark. **(b)** The location of the field site in Vejers and the wave buoy in Nymindegab. Adapted from Brinkkemper et al. (2017).

mean grain size of 180 μm. During the field campaign, the mean grain size was determined at multiple locations and multiple dates. The results are shown in Section 3.1.2.

The field campaign started at 19 September and lasted until 10 October 2016. The campaign was focused on the low to moderate wave energy conditions at the intertidal part of the beach. The energy conditions during the first 10 days of the campaign were low to moderate, resulting in onshore bar migration and accretion of the beach. This period of low energy conditions was followed by a large storm, which resulted in offshore sand transport and flattening of the beach profile. The field campaign ended with 10 days of low energy conditions and extreme low water resulting again in onshore bar migration and accretion of the beach. Time series of the significant wave height H_S, the offshore wave angle α and the water level WL during the field campaign are shown in Figure 3.2. The offshore significant wave height H_S and wave angle α are obtained from a wave buoy located at Nymindegab (for location see Figure 3.1) at a water depth of 16 m and are shown in black. The significant wave height H_S from a wave gauge located at the edge of the surf zone is shown in blue. The bottom panel of Figure 3.2(a) shows the times series of the water level with respect to Normaal Amsterdams Peil (NAP) at the wave gauge. During the field campaign the average offshore significant wave height H_S was 1.13 m. Two specific periods are highlighted in Figure 3.2. The red area shows the period of storm with wave heights over 4 m. From the offshore wave angle α, it appears that the storm moved from south to north. The yellow area indicates the period of extreme low water. The high water level is below the average water level and at some moments the wave gauge is not submerged in water during low tide showing as missing data.

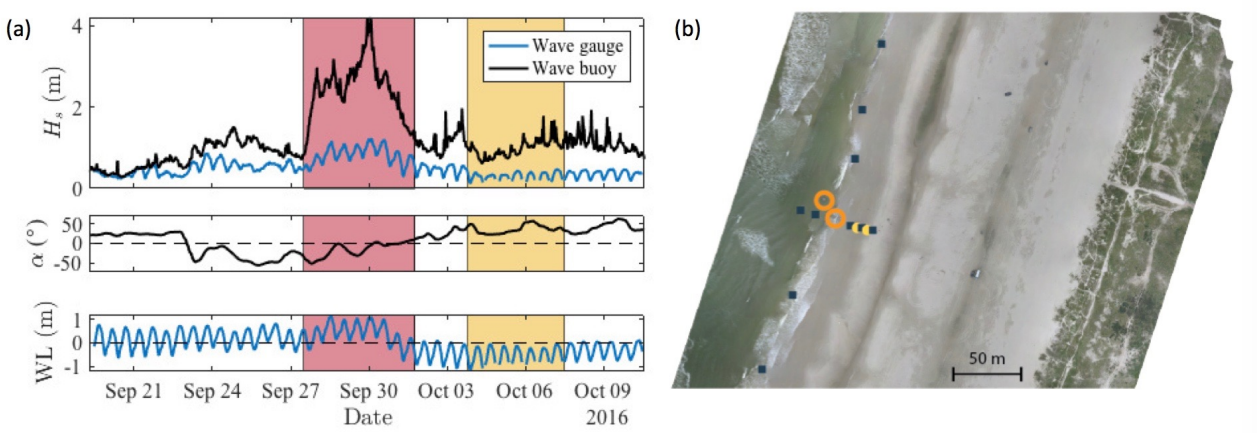

Figure 3.2 – **(a)** Time series of the significant wave height H_S, the offshore wave angle α and the mean water level (WL) during the field campaign. The offshore wave data from the wave buoy is shown in black and the data from the wave gauge located at the edge of the surf zone is shown in blue. A storm occurred during the period highlighted in red. The yellow area indicates a period with extremely low water levels when the high waters were below the average water level during the field campaign. **(b)** An orthophoto of the field site where the symbols indicate the locations of the wave gauges (blue squares), the two smaller frames (yellow circles) and the two larger frames (orange circles). Adapted from Brinkkemper et al. (2017).

3.1.1 Set-up and instrumentation

An orthophoto of the field site is presented in Figure 3.2. The instruments were placed in the intertidal area from -1 m to 1 m above sea level over a cross-shore distance x of 50 m and an along-shore distance y of 200 m. The wave gauges are shown as blue squares in the orthophoto. In the alongshore direction, five wave gauges were placed close to the shoreline during low water. A cross-shore instrument array was located in the intertidal area consisting of five wave gauges (wave gauge 1 is located most seaward), one main frame (frame 1) and two smaller frames (frame 2 and frame 3). The smaller frames are indicated by the yellow circles and the main frame is located at the orange circle. The orange circle slightly north of the cross-shore array is a larger frame from the University of Copenhagen. Only the data of the cross-shore instrument array is analysed in this thesis, because the hydrodynamical model is one-dimensional. Figure 3.3 shows a photo of the cross-shore instrument array and the cross-shore location of the frames and wave gauges in the cross-shore array. The cross-shore distance x is defined 0 at the top of the dune and increases towards the sea.

The smaller frames are equipped with a pressure sensor (5 cm above the bed), an electromagnetic flow meter (15 cm above the bed) and an array of three optical back scatter sensors (5 cm, 10 cm and 15 cm above the bed). The main frame consisted of a pressure sensor (5 cm), an array of five optical back scatter sensors with two additional sensors (2 cm, 5 cm, 8 cm, 13 cm, 15 cm, 25 cm, 30 cm), three Acoustic Doppler velocimeters (20 cm, 25 cm and 30 cm), an acoustic backscatter system (55 cm) and a 3D sonar (50 cm). Daily DGPS surveys were done from the low water line to the end of the swash zone during high water to obtain the cross-shore beach profiles.

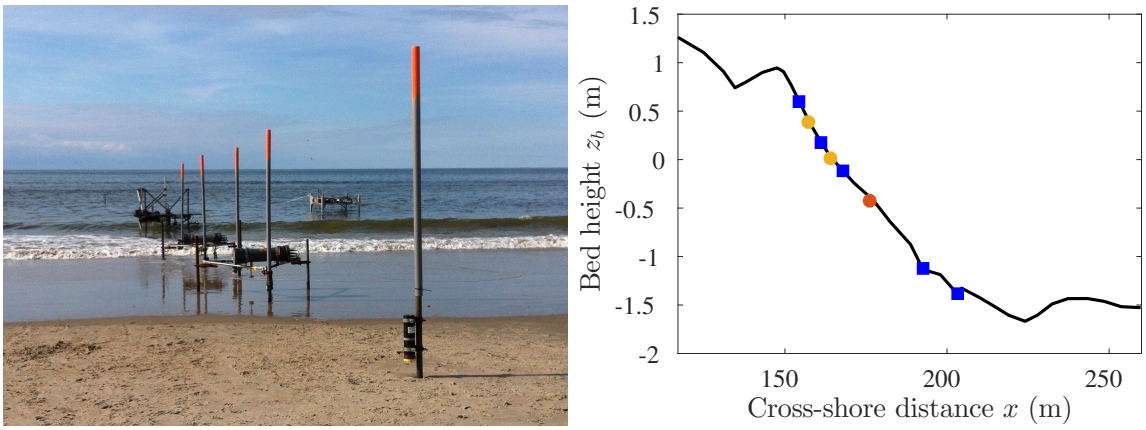

(a) Photo of the cross-shore array **(b)** Location of the frames and wave gauges.

Figure 3.3 – **(a)** A photo of the cross-shore instrument array during high water. The constructions of the smaller frames are shaped like a triangle. The PVC pipes are put on top of the wave gauges. The frame of the University of Copenhagen is located to the right of the instrument array. **(b)** The bed profile at the start of the field campaign (19-09-2016) with the location of the wave gauges (blue squares), the smaller frames (yellow circles) and the main frame (orange circle).

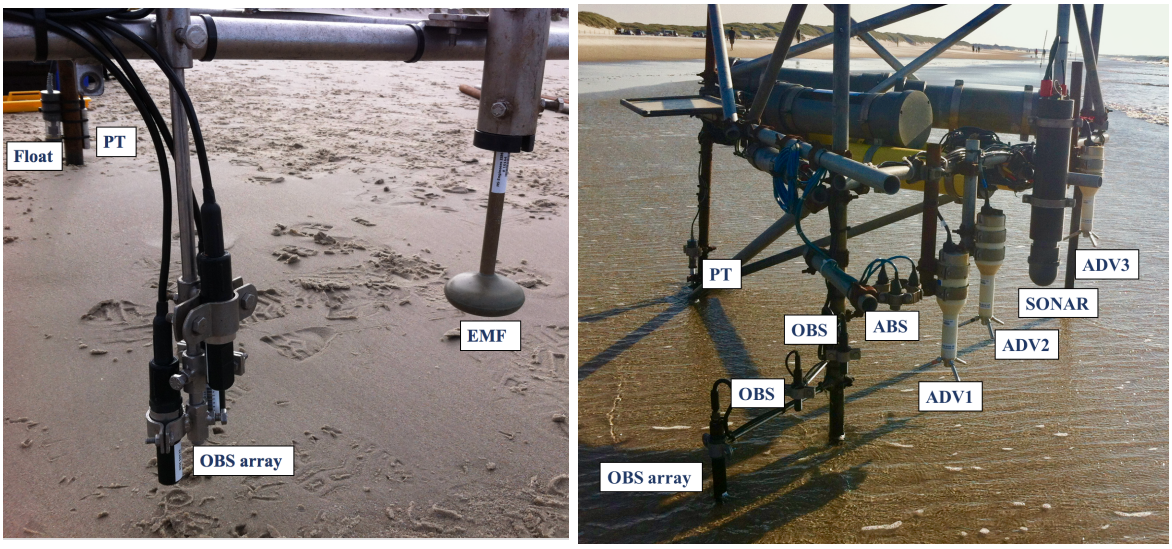

(a) Smaller frame **(b)** Main frame

Figure 3.4 – The positions of the instruments on the frames: the float, pressure sensor (PT), electromagnetic flow meter (EMF), optical backscatter sensor (OBS), Acoustic Doppler velocimeter (ADV), acoustic backscatter system (ABS) and a 3D sonar.

Instruments

Figure 3.4 shows two photos of the position of the instruments on the frames. A floating device was attached to the frames and was checked every 30 minutes. When the float was submerged, the frames started to measure and the measurements stop at the end of the 30 minutes period where the float fell dry. The majority of the instruments measure with a frequency of 4 Hz, except the wave gauges and the Acoustic Doppler Velocimeters that measured with 5 Hz and 10 Hz, respectively. The next list explains shortly how the instruments work and what physical quantity is measured.

- *Pressure sensor.* The pressure of the water induces a mechanical strain, which deforms the piezoresistor located inside the pressure sensors of the frames. This deformation changes the piezoresistors' electrical resistance (Adams and Layton, 2009), resulting in a change in the output voltage in case of a pressure change. The pressure sensor measures the total pressure, which is the sum of the local air pressure and the water pressure. The water pressure p is determined by subtracting the local air pressure from the measured pressure and it is subsequently converted into the water level using

$$p = \rho g(-z + \eta R) \tag{3.1}$$

  where R is a factor that accounts for damping. This first part of the equation is related to the hydrostatic balance (Equation 2.16). The second term is the damping term which accounts for the damping of the sea surface fluctuations towards the bottom. The damping factor R depends on the wave frequency and the wave number (Dobson, 1971). The mean water depth can be determined from the water pressure, as well as the sea surface elevation over time which is used to obtain the wave periods and wave heights.

- *Wave gauge.* A wave gauge is a device that contains a pressure sensor, batteries and memory used for data storage. A wave gauge measures the subsurface water pressure, which is converted to the water level variations as explained in the description of the pressure sensor.

- *Electromagnetic flow meter* (EMF). Sea water is electrically conductive, because particles with an electric charge, like salt, are dissolved in sea water. The sensor of the EMF generates a magnetic field. Faraday's law states that the voltage in a conductor E is given by

$$E = U\,B\,L, \tag{3.2}$$

  where U is the velocity of the conductor (in this case the water), B the magnetic field strength and L the length of the conductor. When the magnetic field generated by the sensor and the length of the conductor are known, the velocity of the water can be computed from the measured voltage. The EMF used during the field campaign consists of two conductors, so the velocity in the x and y direction was measured.

- *Optical backscatter sensor* (OBS). An OBS measures the turbidity using infra-red light scattered from suspended matter. The turbidity is a measure for the clarity of water and is used to determine the suspended sediment concentration. The OBS has a diode that emits an infra-red light beam, which is reflected by the suspended particles and the reflection is measured by the detector in the OBS. Due to irregular shapes of the particles, the light beam is not reflected in a straight path towards the detector but with a slight deflection, which is called light scattering. The sensor measured the infra-red scattering of the particles at an angle of 140° to 160°. The scatter strength is integrated over the angles leading to an output voltage, where a high voltage means a large suspended sediment concentration. The size, composition and shape of the suspended particles influence the signal of the OBS sensor (Van Rijn et al., 2000). Therefore, the OBS needs to be calibrated with the sediment of the study area to transfer the output voltage to a suspended sediment concentration.

- *Acoustic Doppler Velocimeter* (ADV). An ADV measures the water velocity using Doppler shift. Sound waves with a certain frequency are transmitted by the ADV and reflected by particles in the water. The reflected sound waves are measured by the ADV. The movement of the particles with respect to the ADV results in a Doppler shift in frequency of the emitted and received sound waves (Van Rijn et al., 2000). The Doppler shift is measured and from this the water velocity is calculated. The ADV has three beams, so the velocity in the x, y and z direction was measured.

- *Acoustic backscatter system* (ABS) is used to determine the location of the bottom. The ABS transmits an acoustic signal towards the bed, where it is reflected. The reflection by the bed is measured. The location of the bed is determined from the time difference between transmitting the signal and measuring the reflected signal.

- *3D sonar.* The 3D sonar emits sound waves and measures the reflection of the sound waves to find the height of the sand bed. The 3D sensor scans a horizontal strip of the

land and repeats this for every angle to obtain a 3D image of the bed underneath the 3D sensor.

3.1.2 Grain size

During the fieldwork campaign at different days, multiple sand samples were taken at the locations of the frames and the wave gauges. The samples were sieved to determine the medium grain size d_{50}. Using the GRADISTAT software of Blott and Pye (2001), the grain size distribution and the d_{50} value of each sample were determined. The d_{50} as function of the location for different days is shown in Figure 3.5a. The grain size d_{50} at Vejers beach during the campaign varied between 180 μm and 240 μm. The mean grain size of the samples is 210 μm with a standard deviation of 12 μm, which are shown in Figure 3.5b as red and black dashed horizontal lines respectively.

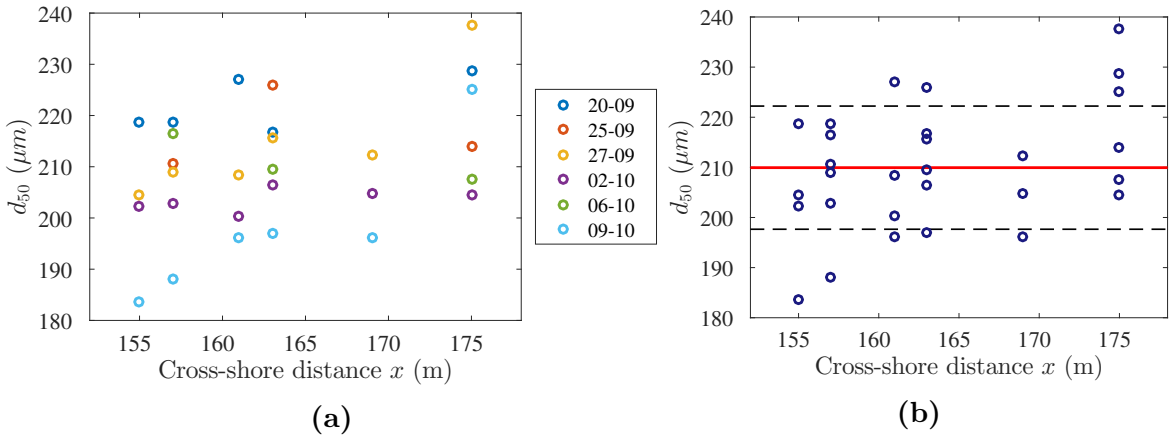

Figure 3.5 – **(a)** The medium grain size d_{50} of the samples that were taken at different cross-shore locations on different days. **(b)** The blue circles are the medium grain sizes of the samples. The mean grain size of 210 μm during the field campaign is indicated by the horizontal red line and the standard deviation of 12 μm is indicated by the black dashed horizontal lines.

3.1.3 The measured bed level change

The bed level change measured during the field campaign is shown in Figure 3.6. The left panel of Figure 3.6 shows the cross-shore bed profiles at four different days. The right panel shows the bed level difference Δz between the measured cross-shore profile and the reference profile of 02-10-2016, as a function of the cross-shore distance and time. At the start of the field campaign, the beach profile contained a steep intertidal bar. During the first 10 days of the campaign, the intertidal bar steepened and moved onshore under the low energy conditions. From 28-09-2016 to 02-10-2016, the high energy conditions during the storm resulted in the disappearance of the inter tidal bar and the beach profile became completely flat. During the low energy conditions that followed the storm, a new intertidal bar formed and migrated in the onshore direction.

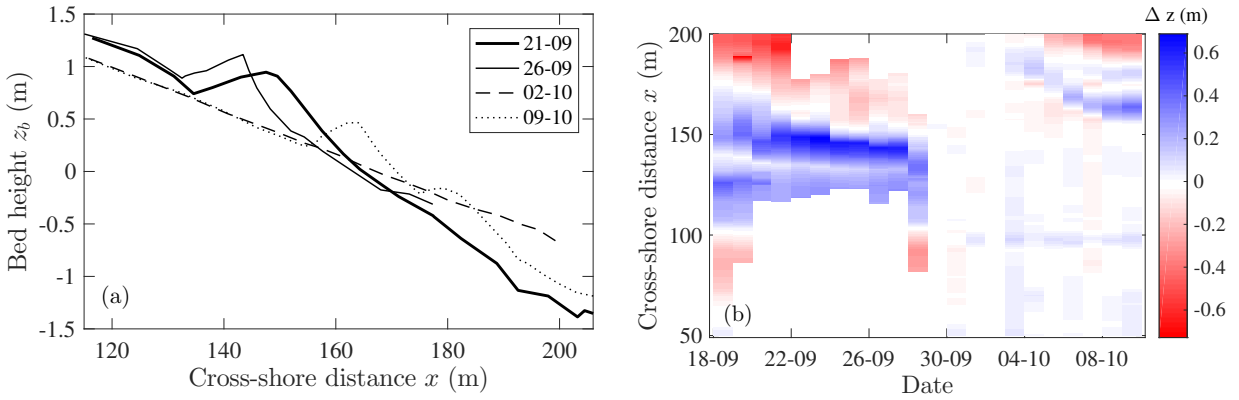

Figure 3.6 – **(a)** The cross-shore profile at the location of the instrument array on different days. **(b)** The bed level difference $\Delta z = z_b(x,t) - z_{b,ref}(x)$, where z_b is the bed height on day t as function of the cross-shore distance x and $z_{b,ref}(x)$ is the reference bed height, which is the bed height on 02-10-2016 as function of the cross-shore distance x.

3.1.4 Data selection and data processing

All the field data were calibrated by technicians of the department of Physical Geography (Utrecht University). The ADV signals of 10 Hz were interpolated to a 4 Hz signal, so all the instruments on the frames have the same output frequency. The velocity close to the bed is important for the sand transport, and for that reason only the velocity data of the lowest ADV of the main frame (ADV 1) is analysed. The measured flow velocities were split in a mean current, high-frequency wave velocity and low-frequency wave velocity, as was done for the modelled flow velocities (see Section 2.2.3). The fast Fourier transform filter was also applied to the time series of the sea surface elevation. Only the high-frequency sea surface elevation η_{HF} is used to determine the significant wave height, wave asymmetry and wave skewness. The significant wave height was calculated using Equation 2.37. The skewness and asymmetry are determined using the skewness function of Matlab, of which details are presented in Appendix B. The skewness and asymmetry of the velocity were computed using the high-frequency wave velocity.

From the field data, two periods were selected based on data availability and the energy conditions. In the total data set during low to moderate energy conditions, frame 1 to 3 were only submerged for two high tides. These periods are from the time period before the storm. Table 3.1 shows the offshore significant wave height H_S, the still water level and the peak period T_p for the two periods. The offshore significant wave height H_S is obtained from the wave buoy and the peak period T_p is determined from the time series of the sea surface elevation at wave gauge 1. The still water level (STW) is the average water surface elevation compared to NAP, which changes due to the effect of the tides. The STW is calculated by subtracting the measured bed height z_b at wave gauge 1 from the average water depth d over 30 minutes at wave gauge 1, so $STW = d - z_b$.

Period	Date	H_s (m)	Still water level (m)	T_p (s)
P1	2016-09-25 21:30	1.04	0.66	6.21
P2	2016-09-26 9:00	0.96	0.72	6.11

Table 3.1 – The offshore significant wave height H_S, the still water level (STW) and the peak period T_p from the field data for the two selected periods.

3.2 The hydrodynamical model SWASH

3.2.1 Model setup

The hydrodynamical model SWASH will be used to simulate the water motion at Vejers beach during the field campaign. All the simulations are done in one dimension, such that the cross-shore direction is considered. The time integration is explicit with a minimum Courant number of 0.001 and a maximum Courant number of 0.5. Bottom friction is added using the Manning's roughness coefficient n, which has a default value of 0.019 $m^{1/3}s$. The value of the Manning's roughness coefficient is calibrated. The wind forcing is not included in the model simulations. The three most important input variables of the SWASH model are the computational grid including a bathymetry, the initial conditions and the boundary conditions.

The same reference point for the cross-shore distance x is used for the SWASH model and the field data. Therefore, $x = 0$ corresponds to the top of the dune and x increases towards the sea. The computational grid starts at a cross-shore distance of 100 m, which is before the start of the intertidal area around 150 m. The grid has a length of 1900 m with a grid size Δx of 1 m. The SWASH model has four vertical layers of equal thickness, which means that each layer equals one fourth of the total water depth h. The depths of the layers vary along the computational grid in the same way the total water depth varies. Layers of equal thickness are also called σ-layers, where σ is an independent variable that represent a scaled water pressure. In the σ-coordinate system, each vertical layer has the same thickness below every point on the water surface.

The input bathymetry of the SWASH model is a reconstruction of the GPS surveys during the field campaign and the adapted bathymetry of Vejers beach in 2010. The GPS surveys measured the bed height from the dunes to the low water line, which means that the largest part of the bathymetry during the field campaign is unknown. However, the complete bathymetry of Vejers beach was measured in 2010 from the dunes to 5 km offshore. The bathymetry of 2010 needs to be adapted to the situation in September 2016 which is part of the calibration process and will be discussed in the next section. Figure 3.7 shows an example of a reconstructed bathymetry that was used as input for the SWASH model. The horizontal velocity u is chosen positive when directed towards the shore. The effect of the tides is included in the still water depth (STW). Figure 3.7 depicts the situation during high water, when the still water depth is higher than the NAP level (dashed line).

The initial conditions are set to zero, thus at time $t = 0$ s there are no flow velocities

and no waves. Waves enter the domain at the seaward boundary, where a random wave field is created by the JONSWAP spectrum. The offshore significant wave height H_S from the wave buoy and the peak period T_p from wave gauge 1 are used as input variables of the JONSWAP spectrum. A time series of the measured sea surface elevation cannot be used as boundary condition at the seaward boundary because the wave height and the wave shape change significantly from the seaward boundary towards the coast (see Section 2.1.1). The sea surface elevation is only measured in the surf zone, when the wave shape has already changed from symmetric to skewed and/or asymmetric and the waves start to break. It takes roughly 5 minutes before the short waves travel from the seaward boundary in the model towards the coast. A spin-up of 20 minutes is used to make sure that the short and long waves travelled to the coast, were reflected, and reached the seaward boundary again. No reflection occurs at the seaward boundary due to the imposed boundary conditions. The landward boundary is not a fixed boundary. The SWASH model determines the shoreline by determining which cells are wet or dry. The simulations were done with a time step of 0.025 second and over 30 minutes, which is the same length as the bins of field data. The total simulation time is 50 minutes: 20 minutes spin-up time and 30 minutes for the real simulation.

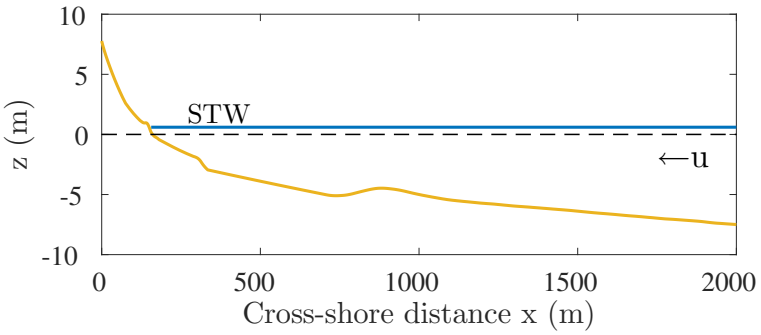

Figure 3.7 – An example of a bed profile in yellow used as input bathymetry for the SWASH model. The velocity u is chosen to be positive towards the shore and the still water depth (STW) is the average water level over 30 minutes with respect to NAP determined from observations.

Model output

The root-mean-square wave height H_{rms}, the averaged water depth d and the flow velocities are used to calculate the sand transport (see Section 2.3). Therefore, these three variables are stored by the SWASH model. The root-mean-square wave height and the averaged water depth are determined from the final 30 minutes of simulation and saved at every grid point. The flow velocities of the four layers are saved with an output frequency of 4 Hz over a cross-shore distance of 620 m starting at 100 m. The velocities are not saved over the whole domain to limit required data storage. Seaward of $x = 550$ m, the current becomes zero and the flow velocities are small indicating the location of the edge of the transition zone. No sand is transported seaward of the transition zone, therefore, the flow velocities are not saved seaward of this point. The location of the edge of the transition zone depends on the still water depth and the offshore wave height. To make sure that the velocity is stored from

the coast to the edge of the transition zone at all times, the velocity data is stored until a cross-shore distance x of 720 m. The model output is compared with the field data to determine the performance of the model. For comparison with the field data, the sea surface elevation is stored with an output frequency of 4 Hz at the locations of the wave gauges and frames in the cross-shore instrument array. An output frequency of 4 Hz was chosen because it is the same frequency as the instruments on the frames. A frequency of 4 Hz is also large enough to resolve non-linearities in the velocity and sea surface elevation.

3.2.2 Calibration method

The input bathymetry

The first part of the calibration process is to obtain an input bathymetry, which is a reconstruction of the GPS surveys and the bathymetry of 2010. It turned out that the bathymetry of Vejers beach measured in 2010 needed to be adapted to the situation of autumn 2016, which is done in four different ways. Five bed profiles are considered in the calibration process, the original bathymetry of 2010 (VJ2010) and four profiles with different adaptations to the bathymetry of 2010. Figure 3.8 shows the bathymetry of 2010 in black together with the four adapted bed profiles. The original bathymetry has a steep bar over a cross-shore distance of around 400 to 700 m, which is removed in the four profiles. The bed height of the beach and the near-shore zone (x =0 m to 280 m) is also removed to avoid sudden jumps in the bed profile, since the GPS surveys measured the bed height z_b of the beach face and the near-shore zone ($x = 0 - 187$ m). The B1 profile (see Figure 3.8) was obtained by combining the GPS survey with the 2010 bathymetry, excluding the bar and the near-shore zone, and applying a moving mean over 5 points. The profile increases linearly from $x = 700$ m to 340 m where it aligns with the VJ2010 profile until a distance $x = 280$ m, followed by a linear increase to the GPS survey measurements. The B2 profile increases linearly from $x = 700$ m to the GPS measurements, so this profile does not include any kind of bar or change in bed slope. The M40 profile is obtained by removing the bar from the VJ2010 profile and subsequently applying a moving mean over 40 points. After this, the bed height is removed in the near-shore before it is combined with the GPS survey data. A subtidal bar was observed during the field campaign and was measured during the last part of the field campaign when the water levels were low. The bar measured on the 4th of October was added to the B1 profile to obtain the BAR profile. The bathymetry during the field campaign is best represented by the BAR profile because the BAR profile was created using the largest number of GPS survey points.

The calibration parameters

Next to the input bathymetry, the values of the Manning's roughness parameter n and the two wave breaking parameters α and β need to be calibrated for the SWASH model. The wave breaking parameters α and β induce wave breaking in the SWASH model, which is necessary in case of less than 10 vertical layers (Smit et al., 2013). The default values of these parameters are n=0.019 $\mathrm{m}^{1/3}$s, $\alpha = 0.6$ and $\beta = 0.3$.

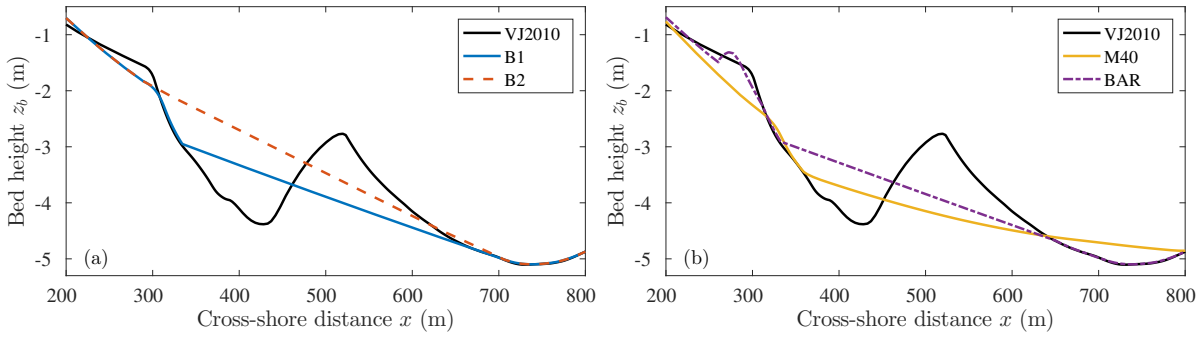

Figure 3.8 – The five near-shore bed profiles used for calibration of the SWASH model. The measured bathymetry of Vejers beach in 2010 (VJ2010) is shown in black, together with (a) the B1 profile and the B2 profile, and (b) the M40 profile and the BAR profile.

For different combinations of these parameters, the field data and the model output are compared for the two selected periods (P1 and P2) on the six variables: the significant wave height H_S, current U_C, wave skewness, wave asymmetry, the skewness of the high-frequency velocity and the asymmetry of the high-frequency velocity. The comparison is based on the root-mean-square error and the cross-shore distribution of the variable. The normalised root-mean-square error E_{rms} of variable y is calculated as

$$E_{rms,y} = \sqrt{\frac{\sum_{i=1}^{N}(\hat{y}_i - y_i)^2}{N\ var(y)}}, \tag{3.3}$$

with $\hat{y}_i$ the variable from the field data, y_i the value of variable determined from the model output, N the number of observation points and $var(y)$ the variance of variable y. The number of observation points is the sum of the data points in the cross-shore distance (8 in total in the cross-shore instrument array) multiplied by the time periods used for calibration. The field data of wave gauge 5 and frame 3, the locations closest to the beach, were not used in the comparison because the results here were unrealistic because of a small water depth. Therefore, the amount of observations points N equals 12 ($N = (8-2) \times 2 = 12$ for the wave height, wave skewness and wave asymmetry and N equals 4 ($N = (3-1) \times 2 = 4$) for the current, the skewness and asymmetry of the velocity. To compare the root-mean-square error of the different variables, the error is normalised by the square root of the variance (var) of variable y,

$$var(y) = \frac{1}{N}\sum_{i=1}^{N} y_i^2 \tag{3.4}$$

The variance is an indication of the spread of the model output and is used as an indication of the typical values of the variables. When the root-mean-square error is normalised, the errors for the different values can be compared although the variables normally differ in magnitude and units. The total normalised root-mean-square error $E_{rms,tot}$ is defined as the variance of

the normalised root-mean-square errors of the six variables ($Y = 6$),

$$E_{rms,tot} = \sqrt{\frac{1}{Y}\sum_{i=1}^{Y} {E_{rms,y}}^2} \tag{3.5}$$

The root-mean-square error is a measure of the accuracy of the model and includes information over the average error together with the variation in the errors. When the root-mean-square error increases, the difference between the measurements and the model output increases. For that reason, the ideal value of E_{rms} is zero. Normalising the root-mean-square error by the variance, the normalised root-mean-square error also contains information about the spreading of the model. The normalised root-mean-square error increases in case of small spread of the model output. In case of a large spread, the error can be caused by the natural spreading of the variables. While in case of no spreading, the error is more significant and the normalised E_{rms} increases.

The flow velocity changes in direction and magnitude with height in the water column. Therefore, the modelled flow velocity and the measured flow velocity need to be compared at the same height. Figure 3.9 shows the measured mean current in red at the height above the bed h_b of the instrument for frame 1 and frame 2, the frames used for calibration. The modelled mean current of the four layers are shown in blue, where the height above the bed corresponds to the middle of the layers. Comparing the height of the instruments with the height of the layers, the middle of layer 3 is closest to the instrument height for both frames. Therefore, the flow velocities of layer 3 are used to compute the mean current and both the skewness and asymmetry of the high-frequency velocity. The height of layer 3 is around 0.25 m and 0.15 cm above the bed at the location of frame 1 and frame 2, respectively.

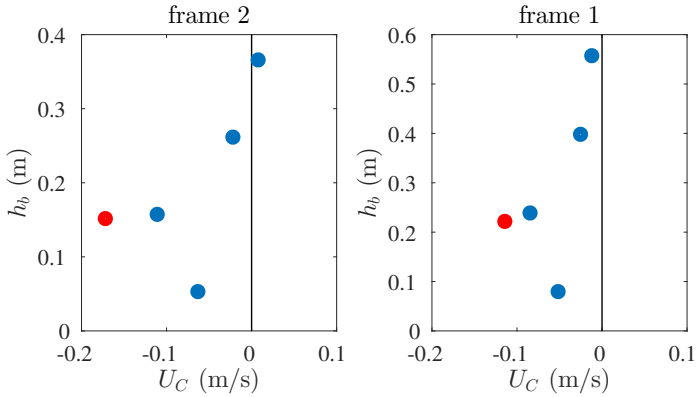

Figure 3.9 – The measured mean current U_C at the height above the bed h_b of the instrument in red for frame 1 and frame 2. The modelled mean currents of the four layers are plotted in blue, where the height above the bed corresponds to the middle of the layers. The instrument height is closest to the height of layer 3.

Figure 3.10 shows a schematic view of the calibration method of the SWASH model, together with the coupling between the SWASH model and the sand transport model. The calibration of the SWASH model is done by adjusting the variables independently and comparing

the model output with the field data. First, the input bathymetry is calibrated. The best bed profile will be chosen based on the value of the total normalised root-mean-square error $E_{rms,tot}$ and comparison of the cross-shore distribution of the variables. The input bathymetry influences the location of wave breaking and the values of the six variables because they all depend on the water depth and the location of a sandbar. For that reason, the cross-shore distribution of the model output is compared to the field data to determine whether the location of a local maximum or minimum compares and if the model shows a decrease or increase of the variables towards the coast. The best bed profile is the profile with a small $E_{rms,tot}$ and a cross-shore distribution of the variables that compares well with the field data.

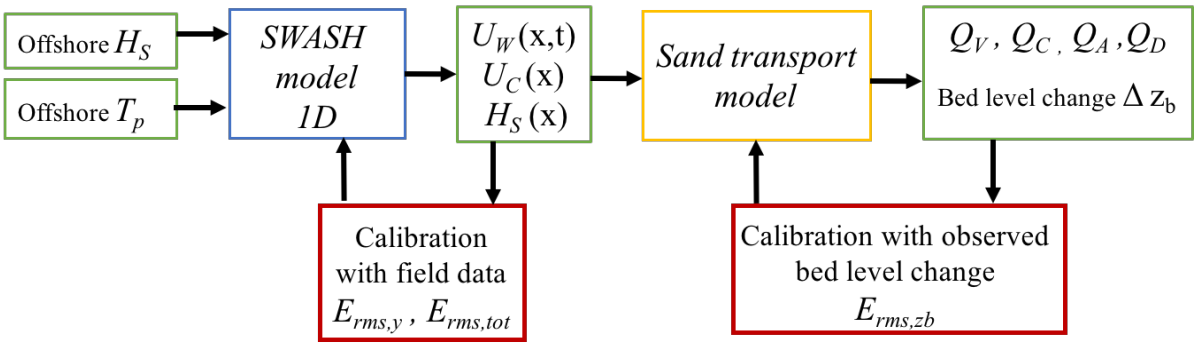

Figure 3.10 – Schematic view of the coupling between the hydrodynamical SWASH model and the sand transport model together with the calibration methods, with the significant wave height H_S, the peak period T_p, the wave velocity U_W, the current U_C, the transport by the waves Q_V, the transport by the currents Q_C, the acceleration-driven transport Q_A, the diffusive transport Q_D and the root-mean-square error E_{rms}.

When the optimal bed profile is determined, the best values of the wave breaking parameters β will be found using nine combinations of the persistence parameter β and the steepness parameter α: the default values ($\beta = 0.3$, $\alpha = 0.6$), an increase of 0.1 and a decrease of 0.1 of the default values. The combination with the smallest total root-mean-square error is the best value of the persistence parameter β. The best value of the steepness parameter α is determined in combination with the Manning's roughness coefficient n. For the calibration of the Manning's roughness coefficient is varied between 0.011 and 0.023 $\mathrm{m}^{1/3}\mathrm{s}$ in steps of 4×10^{-3} $\mathrm{m}^{1/3}\mathrm{s}$. Again, the wave breaking parameter α is varied between 0.5 and 0.7, but now in steps of 0.05. The combination with the smallest total root-mean-square error is chosen as best values for the Manning's roughness coefficient n and the steepness parameter α.

3.2.3 Comparison of the SWASH output with the field data

The model output of the SWASH model of the simulation with the best bed profile and the best fit parameters is compared to the field data by the cross-shore distributions of the six variables and the wave profile. The wave profile is determined from the modelled and measured high frequency sea surface elevation. The variance density spectra are computed from the sea surface elevation time series using a fast Fourier transformation. The variance density spectra are used to compare the peak frequencies of the field data and the model

output, and also to see if the energy is similarly distributed over the frequencies in the model and the data. The wave profile is also compared using the phase-averaged sea surface elevation. First, the downward zero-crossings in the sea surface elevation are determined to identify all the individual waves of the time series. Thereafter, each wave is divided into 20 parts. For all the identified waves, the mean sea surface elevation is computed for each part, resulting in the phase-averaged sea surface elevation.

3.3 Sand transport model and bed level change

3.3.1 Computation of the sand transport and the bed level change

The SWASH model output includes the root-mean-square wave height H_{rms} and the average water depth d over 30 minutes of simulation together with the flow velocities of the four layers as a function of time and the cross-shore distance. This is used to calculate the four transport components averaged over 30 minutes as a function of distance: the transport by the waves Q_V, the transport by joint waves and currents Q_C, the acceleration-driven transport Q_A and the diffusive transport Q_D. The total cross-shore sand transport Q_{tot} is calculated as a function of distance using Equation (2.45). The bed level change over 30 minutes Δz_b is computed from the total transport by integrating Equation 2.46 over time,

$$\Delta z_b = -\frac{1}{1-p}\int \frac{dQ_{tot}}{dx}\ \mathrm{d}t. \tag{3.6}$$

Since the total transport is time independent, the integral can be simplified to

$$\Delta z_b = -\frac{1}{1-p}\frac{dQ_{tot}}{dx}\Delta t. \tag{3.7}$$

where Δt is 30 minutes.

3.3.2 Calibration method

Each of the four sand transport terms contains a calibration constant. The ranges of the parameters considered are: the wave friction coefficient C_W from 0 to 10^{-2}, the current friction coefficient C_C from from 0 to 10^{-4}, the calibration constant of the acceleration-driven transport Ka from 0 to 10^{-5} and the coefficient of the diffusive transport λ_d from 0 to 10^{-6}. To calibrate the sand transport model, the modelled bed level change in the near-shore zone is compared to the measured bed level change. The measured bed level change as function of the cross-shore distance x is the difference between the GPS survey on 25-09 and on 26-09. The bed level height z_b was measured at slightly different locations on both days, so the GPS data of 26-09 was interpolated to the same locations as the GPS data of 25-09 before the measured bed level change was calculated. The GPS surveys were performed at 14:00 on 25-09 and at 15:30 on 26-09, which means that the bed level change determined from the GPS surveys is measured over a total time period of 25.5 hours.

To model the bed level change over 25.5 hours, the total time period of 25.5 hours is split

in 52 periods of 30 minutes. For every 30 minutes the still water depth, significant wave height and peak period are determined from the field data and used as input of the SWASH model (see Appendix C). The bed profile at the start of the simulation, a combination of the calibrated bathymetry and the GPS measurements on 25-09, is used as input for the first simulation period in the SWASH model starting at 14:00. The bed level change over 25.5 hours is simulated by a joint composition of the SWASH model and the sand transport model, following the consecutive steps.
1) Run the SWASH model with the still water depth, significant wave height and peak period determined from the field data. The simulation time is again 50 minutes: 20 minutes of spin up time and 30 minutes of actual simulation.
2) Use the flow velocities, the significant wave height and averaged water depth from the SWASH output as input for the sand transport model.
3) Calculate the total transport Q_{tot} and the corresponding bed level change Δz_b over the 30 minutes of simulation.
4) Create a new bed profile by adding the calculated bed level change to the bed profile at start of the simulation period.
5) Use the new bed profile as input for the next simulation period in the SWASH model and start again at 1.

The modelled bed level change over 25.5 hours is compared to the measured bed level change based on the root-mean-square error of the bed level change $E_{rms,zb}$,

$$E_{rms,zb} = \sqrt{\frac{\sum_{i=1}^{M}(\Delta\hat{z}_{b,i} - \Delta z_{b,i})^2}{M}}, \tag{3.8}$$

where the sum is over the measurement points in the cross-shore direction and the measured bed level change $\Delta\hat{z}_{b,i}$ as a function of the cross-shore distance, the modelled bed level change $\Delta z_{b,i}$ and the number of measurement points M. The modelled bed level change is interpolated to the grid of the GPS survey data of 25-09, which contained 21 points ($M = 21$). The set of calibration constants resulting in the smallest root-mean-square error are considered the best fit parameters.

3.3.3 The effect of the different transport mechanisms

The best fit parameters of the sand transport model are used to quantify the sand transport during fair weather conditions at Vejers beach related to the transport by waves Q_V, the transport by joint waves and currents Q_C, the acceleration-driven transport Q_A and the diffusive transport Q_D related to the presence of bed slopes. The significance of the four transports are evaluated as a function of time and distance, to determine which of the transports has the largest contribution during low tide and high tide, in the surf zone and above the bar.

Chapter 4: Results

4.1 Performance hydrodynamical SWASH model

4.1.1 Calibration results

Bed profile

Simulations with the hydrodynamical model SWASH are done for the five designed bed profiles using the default values of the Manning's friction coefficient n and the wave breaking parameters α and β. The performance of the SWASH model for the various bed profiles is tested based on the normalised root-mean-square error E_{rms} (Equation 3.3) of the model output and the field data of the periods P1 and P2. The E_{rms} is calculated for six variables: the significant wave height H_S, the mean current U_C, the asymmetry (AS) and skewness (SK) of the high frequency sea surface elevation η_{HF}, as well as for the high frequency wave-velocity U_{HF}. The normalised root-mean-square errors of the six variables for the different bed profiles are shown in Table 4.1, where the bold values correspond to the smallest normalised root-mean-square error E_{rms} for each variable.

The total E_{rms} is smallest for the BAR profile, the only bed profile with an $E_{rms,tot}$ smaller than 1. The BAR profile has the smallest error of the five profile for the mean current and the skewness of the high frequency wave velocity. However, the BAR profile's errors in the

Table 4.1 – The normalised root-mean-square error E_{rms} of the significant wave height H_S, the mean current U_C, the asymmetry AS and the skewness SK of the high frequency sea surface elevation η_{HF} and the high frequency wave velocity U_{HF} for the five calibration profiles. The total E_{rms} is the variance of the six errors (Equation 3.5). The bold values correspond to the smallest E_{rms} for each variable. The simulations were performed using n=0.019 $m^{1/3}s$, $\alpha = 0.6$ and $\beta = 0.3$ for period P1 and P2 (see Table 3.1).

Bed profile	E_{rms} H_S	E_{rms} U_C	E_{rms} AS of η_{HF}	E_{rms} SK of η_{HF}	E_{rms} AS of U_{HF}	E_{rms} SK of U_{HF}	$E_{rms,tot}$
BAR	0.42	**0.40**	0.62	**0.83**	0.39	1.95	**0.94**
M40	0.18	1.07	0.57	1.55	0.97	**1.69**	1.13
VJ2010	0.16	0.61	**0.47**	1.36	0.32	1.96	1.03
B2	**0.05**	0.94	0.52	1.05	0.90	2.09	1.12
B1	**0.05**	0.80	0.51	1.31	**0.15**	1.91	1.02

significant wave height and the asymmetry determined from the sea surface elevation are the largest of all the profiles. The B1 profile has also a small total E_{rms} and performs best of the five profiles on modelling the significant wave height, but has a large error for the mean current. The mean current and the significant wave height are important input variables of the sand transport model, therefore the cross-shore distribution of these two variables is investigated for the BAR profile and the B1 profile. Figure 4.1 shows the significant wave height H_S and the current U_C of the field data in blue at the locations of the cross-shore instrument array during the period P1, from 21:30 till 22:00 on 25-09-2016 (see Table 3.1). The modelled significant wave height and mean current are also plotted for the B1 profile and the BAR profile in respectively orange and purple. The significant wave height H_S close to the coast is simulated better in case of the B1 profile (orange) than in case of the BAR profile. However, the simulation with the B1 profile overestimates the wave height at the two most seaward located measurement points. The simulation with the BAR profile underestimates the wave height close to the shore and overestimates the wave height in the seaward measurement point. Regarding the mean current U_C, the field data show a local extremum at the location of frame 2 ($x = 165$ m). This local extremum is also seen in the modelled mean current of the B1 profile, but not in the mean current of the BAR profile. Because the BAR profile is not able to simulate the local extremum in the mean current, the B1 profile is used as input bathymetry of the SWASH model. Recall that the BAR profile includes the inner sand bar that was measured at the end of the campaign, while the surf zone bathymetry of the B1 profile is not based on measurements and does not include an inner bar. The effect of the inner bar in the BAR profile on the sand transport mechanisms is discussed in Section 5.4.

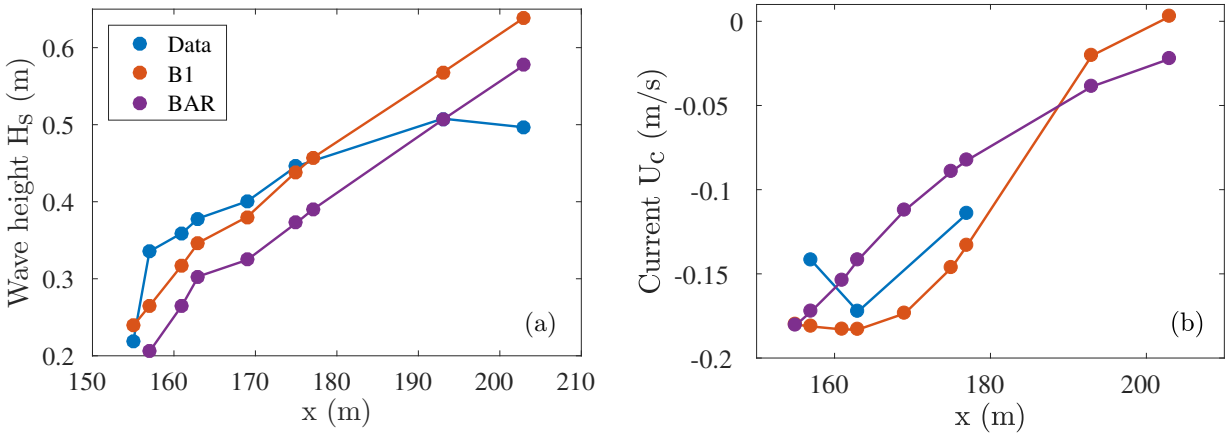

Figure 4.1 – Comparison of the field data and the hydrodynamical SWASH model for period P1, i.e. 21:30 till 22:00 on 25-09-2016 (see Table 3.1). (a) The significant wave height H_S at the location of the cross-shore instrument array of the field data (blue), the model data of the B1 profile (orange) and the model data of the BAR2 profile (purple). (b) The mean current U_C at 0.2 m depth at the location of the cross-shore instrument array of the field data (blue), the model data of the B1 profile (orange) and the model data of the BAR2 profile (purple).

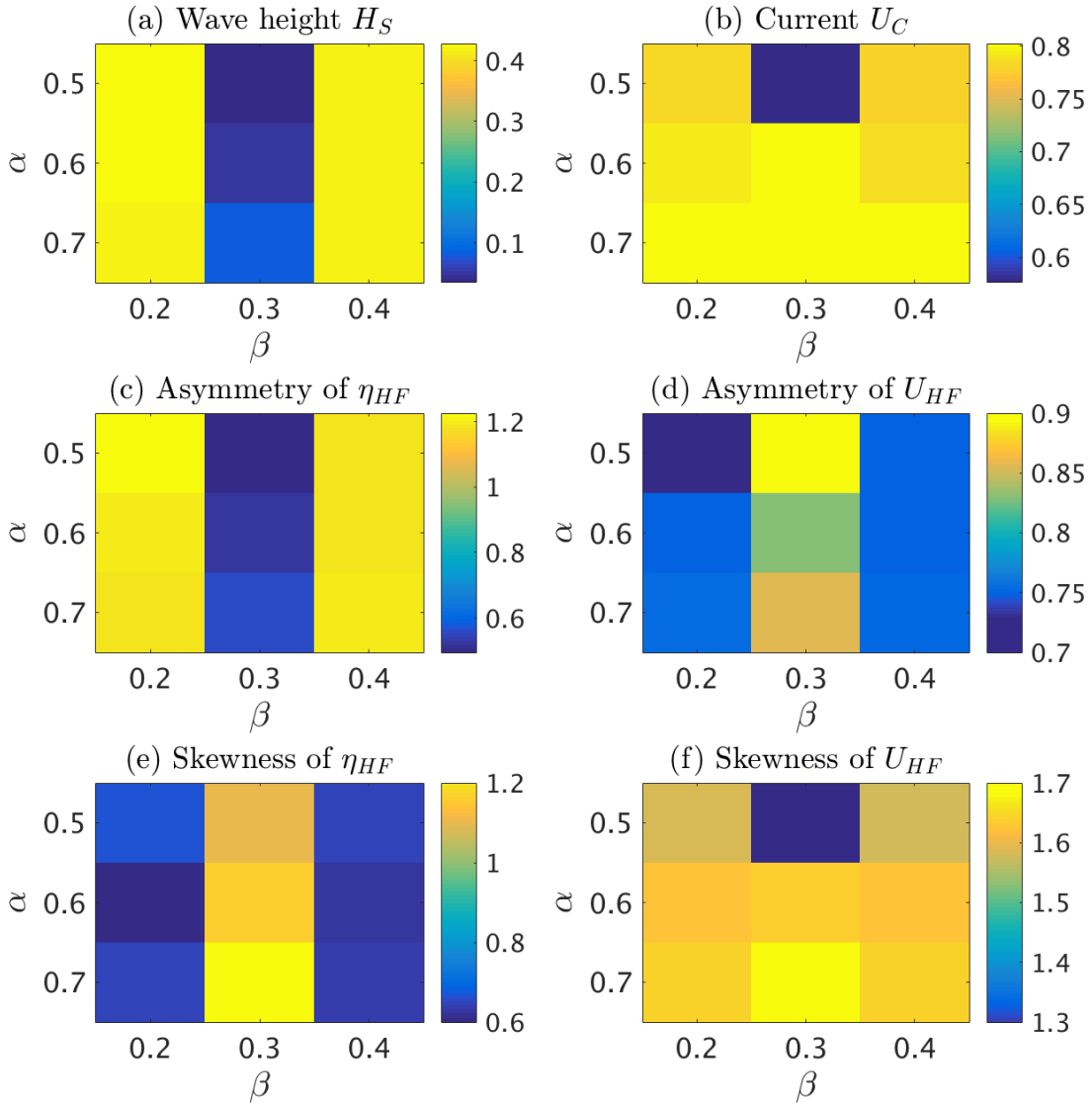

Figure 4.2 – (a) Colour plot of the normalised root-mean-square error E_{rms} of the significant wave height H_S for three values of the wave breaking parameters α and β, using the B1 profile with a constant roughness coefficient $n = 0.019$ m$^{-1/3}$s. See Table 3.1 for the other input parameters of the SWASH model. (b) As (a), but for the current U_C. (c) As (a), but for the asymmetry of the high frequency sea surface elevation η_{HF}. (d) As (a), but for the asymmetry of the high frequency wave velocity U_{HF}. (e) As (a), but for the wave skewness of the high frequency sea surface elevation η_{HF}. (f) As (a), but for the skewness of the high frequency wave velocity U_{HF}.

The wave breaking parameters

Simulations with the SWASH model are done with three different values of the wave breaking parameters α (0.5, 0.6, 0.7) and β (0.2, 0.3, 0.4). The normalised root-mean-square error E_{rms} is determined for the nine combinations of the wave breaking parameters α and β separately for the six variables and the results are shown in Figure 4.2. Note that the colour bars have a different scale. In cases where $\beta = 0.3$, the E_{rms} is minimal for the wave height H_S, the current U_C, the asymmetry of the high frequency sea surface elevation η_{HF} and the skewness of the high frequency wave velocity U_{HF}. Contrary to the E_{rms} of the asymmetry of the high frequency wave velocity U_{HF} and the skewness of the sea surface elevation η_{HF}, which are maximal for the cases where $\beta = 0.3$. The discrepancy between the modelled and measured skewness of the sea surface elevation in cases where $\beta = 0.3$ is due to the overall overestimation of the skewness by the SWASH model. The waves are higher and the mean current is smaller in the simulations where $\beta = 0.3$ compared to other simulations. Therefore, less waves are breaking in the cases where $\beta = 0.3$, resulting in more asymmetric waves at the location of the instrument array. Because of the overall overestimation of the skewness, the increase in the skewness leads to a large root-mean square error E_{rms}. In spite of the large E_{rms} of the asymmetry of U_{HF} and the skewness of η_{HF}, the total E_{rms} is smallest for the cases where $\beta = 0.3$. Hence a value of 0.3 for the persistence parameter β is used to determine the best combination of the steepness parameter α and the roughness coefficient n in the next section.

The combination of wave breaking and friction

Simulations are done for five different values of the wave breaking parameter α (0.5, 0.55, 0.6, 0.65, 0.7) and for four different values of the bottom friction coefficient n (0.011, 0.015, 0.019, 0.023 $\mathrm{m}^{-1/3}\mathrm{s}$). Figure 4.3 shows the total normalised root-mean-square error $E_{rms,tot}$. Recall that the $E_{rms,tot}$ is the variance of the $E_{rms,y}$ of the six variables, which are separately plotted in Figure 4.4. The simulation where $\alpha = 0.5$ and n=0.011 $\mathrm{m}^{-1/3}\mathrm{s}$ performs best with the smallest total root-mean-square error $E_{rms,tot}$. Values of $\alpha = 0.5$ and n=0.011 $\mathrm{m}^{-1/3}\mathrm{s}$ yield the best fit parameters and will be used in combination with the B1 profile and $\beta = 0.3$ for the simulations.

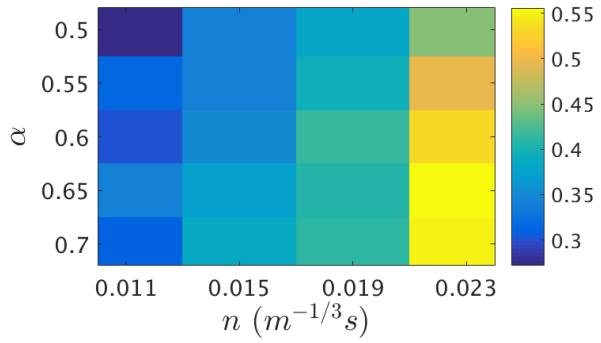

Figure 4.3 – Colour plot of the total normalised root-mean-square error $E_{rms,tot}$ for four values of the Manning's roughness coefficient n and five values of the steepness parameter α, using the B1 profile and a constant persistence parameter $\beta = 0.3$.

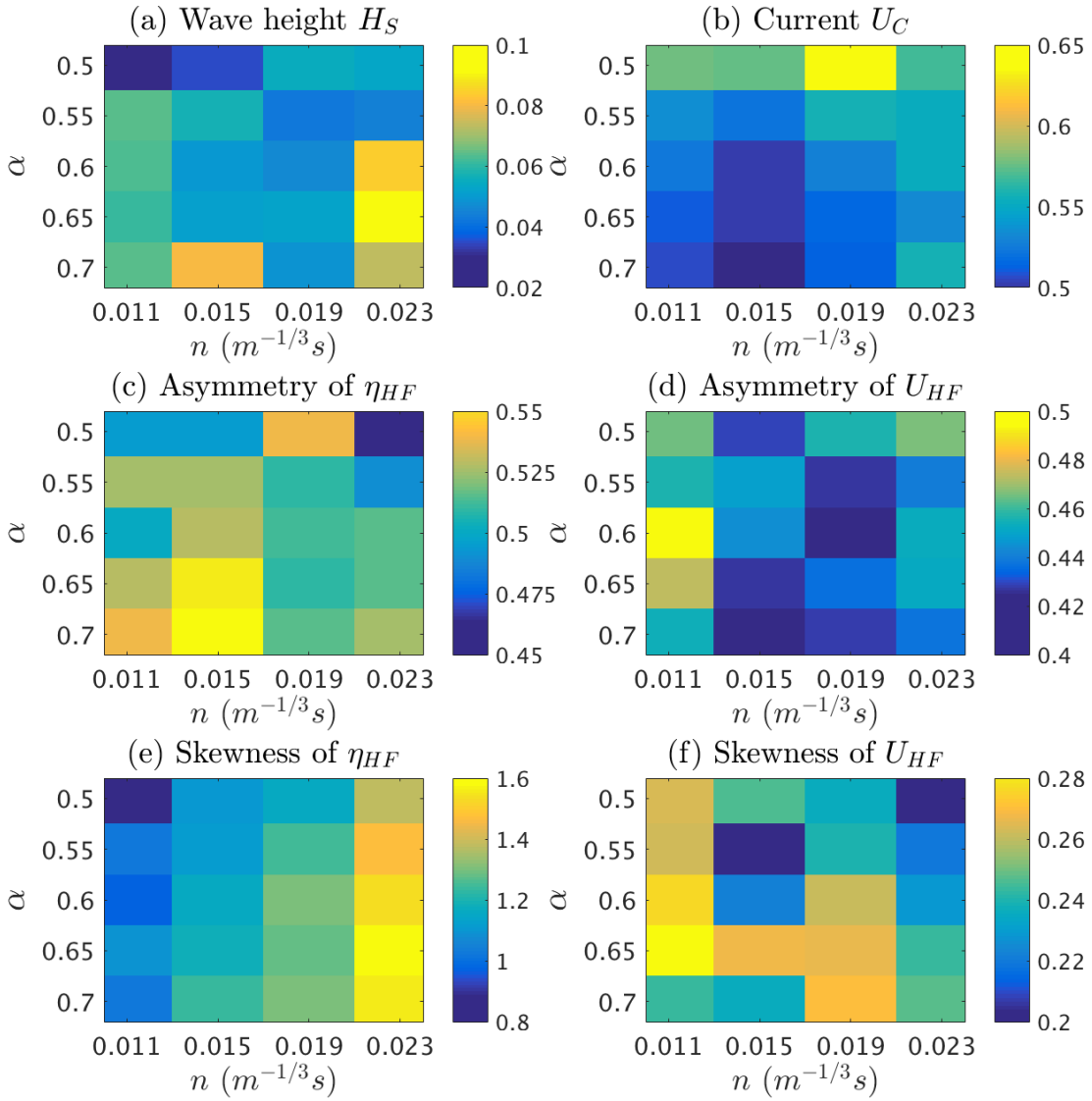

Figure 4.4 – (a) Colour plot of the normalised root-mean-square error E_{rms} of the significant wave height H_S for four values of the Manning's roughness coefficient n and five values of the steepness parameter α, using the B1 profile with a constant persistence parameter $\beta = 0.3$. See Table 3.1 for the other input parameters of the SWASH model. (b) As (a), but for the current U_C. (c) As (a), but for the asymmetry of the high frequency sea surface elevation η_{HF}. (d) As (a), but for the asymmetry of the high frequency wave velocity U_{HF}. (e) As (a), but for the wave skewness of the high frequency sea surface elevation η_{HF}. (f) As (a), but for the skewness of the high frequency wave velocity U_{HF}.

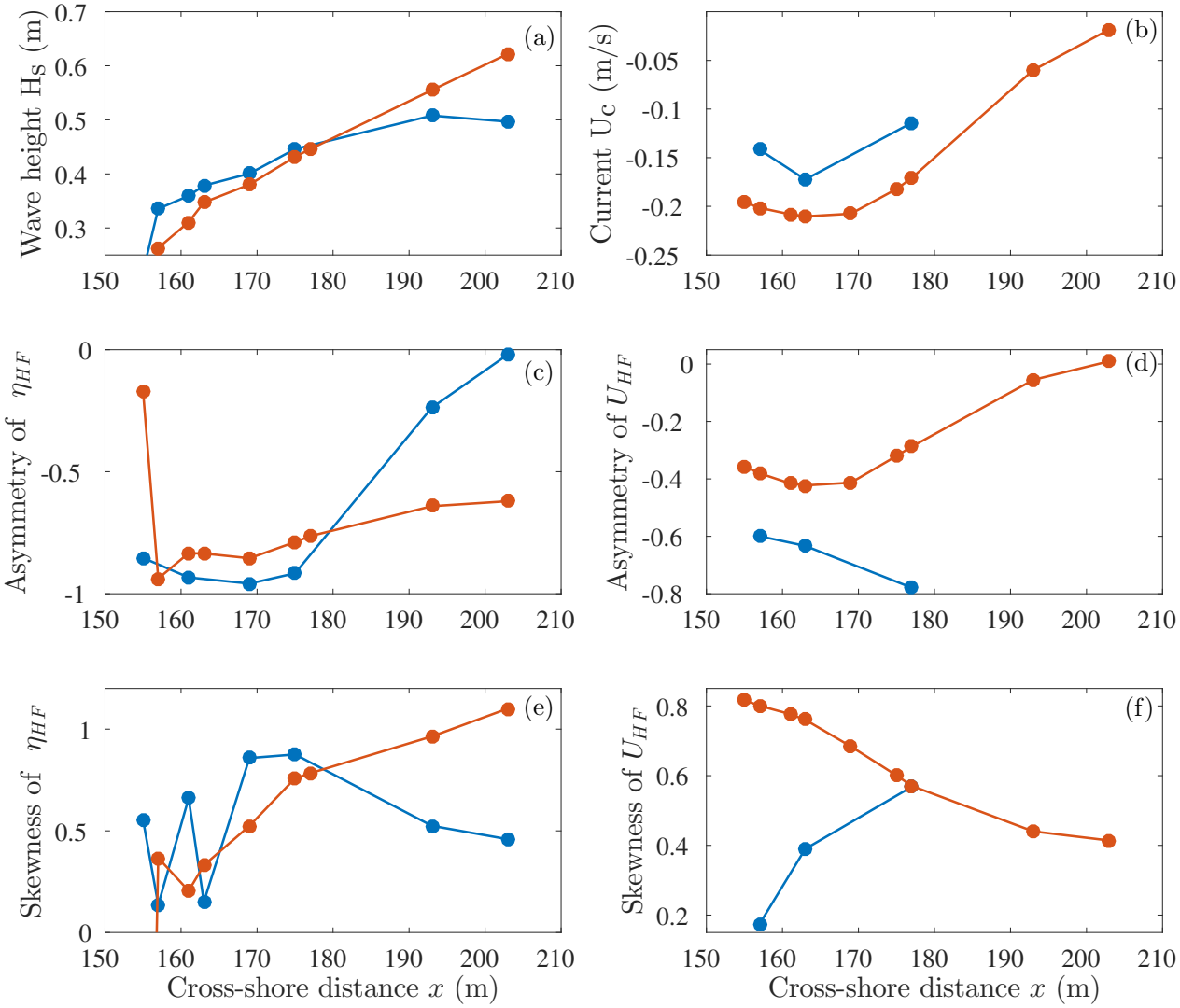

Figure 4.5 – (a) Comparison for period P1 of the significant wave height H_S of the field data in blue and the model output in orange, using the best fit parameters Manning's roughness coefficient $n = 0.011$ m$^{-1/3}$, steepness parameter $\alpha = 0.5$ and persistence parameter $\beta = 0.3$. (b) As (a), but for the current U_C. The modelled velocity of layer 3 is used to determine the current, because the height of this layer corresponds to the height of the velocity measurements. (c) As (a), but for the asymmetry determined from the high frequency sea surface elevation η_{HF}. (d) As (a), but for the asymmetry determined from the high frequency wave velocity U_{HF} of layer 3. (e) As (a), but for the skewness determined from the high frequency sea surface elevation η_{HF}. (f) As (a), but for the skewness determined from the high frequency wave velocity U_{HF} of layer 3.

4.1.2 Comparison of the SWASH output with the field data

The model output of the simulation with best fit parameters in $\alpha = 0.5$, $\beta = 0.3$ and n=0.011 m$^{-1/3}$s is compared with the field data. The results of period P1, from 21:30 to 22:00 on 25-09-2016 (see Table 3.1), are shown in this section, the comparison was also done for period P2, which can be found in Appendix D. The six hydrodynamical variables (H_S, U_C, $AS_{\eta,HF}$, $AS_{U,HF}$, $SK_{\eta,HF}$, $SK_{U,HF}$) at the locations of the cross-shore measurement are shown in Figure 4.5. The field data is plotted in blue and the model output is plotted in orange. Comparing the modelled current with the best fit parameters to the case with the default values in Figure 4.1, the modelled current in case of the default parameters compared better with the field data than the modelled current using the best fit parameters. This is also observed in the normalised root-mean-square of the current (Figure 4.4). The error in the current is larger in case of the best fit parameters (α=0.5, n=0.011 m$^{-1/3}$s) compared to the default values (α=0.6, n=0.011 m$^{-1/3}$s). Although the total root-mean-square error is smaller and overall the six variables are modelled better using the best fit parameters, the individual variables are not necessary modelled better using the best fit parameters.

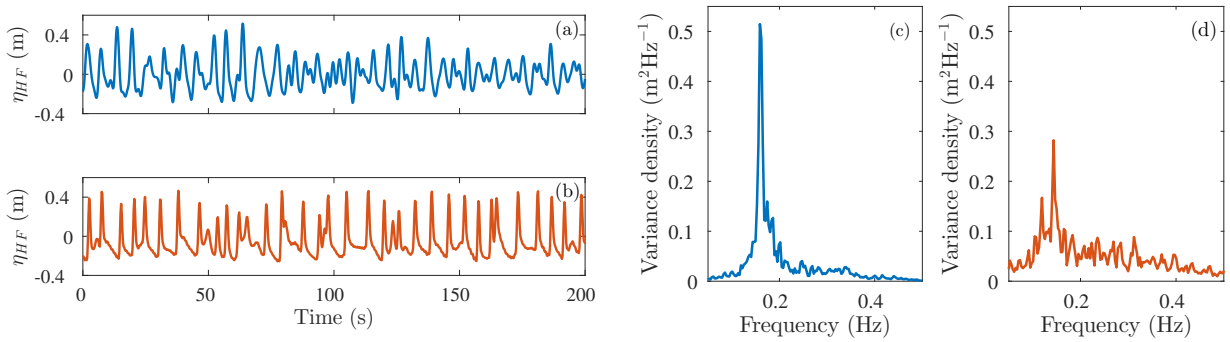

Figure 4.6 – The high frequency sea surface elevation at wave gauge 1 for period P1, i.e. from 21:30 to 22:00 on 25-09-2016, from (a) the field data and (b) the SWASH model. (c) The high frequency wave spectrum, the variance density versus the frequency, determined from the sea surface elevation time series of the field data and (d) As (c), but for the model output.

Figure 4.6 shows the measured and modelled high frequency sea surface elevation at wave gauge 1 in respectively blue and orange. The data of wave gauge 1 is selected, because this is the most seaward location where wave breaking is minimal. The variance energy density spectra are determined from the time series and shown in Figure 4.6. The peak frequency f_p of the field data is 0.16 Hz, which is higher than the peak frequency of the model (f_p=0.14 Hz). A clear frequency peak is absent in the wave spectrum of the modelled sea surface elevation, most of the wave energy is located in the lower frequencies. The modelled wave profile differs from the measured wave profile. The modelled waves are peaky and appear to be less random than the measured waves. The phase-averaged sea surface elevation is determined as explained in Section 3.2.3. Figure 4.7 shows the phase-averaged wave shape at the locations of the instrument array. The field data is shown in blue and the model data is shown in orange. In the model data, the trough is shallow and long, contrary to the crest

which is high and small (peaked). The discrepancy in wave shape between the model output and field data is largest at the locations of wave gauge 1 (a) and wave gauge 2 (b).

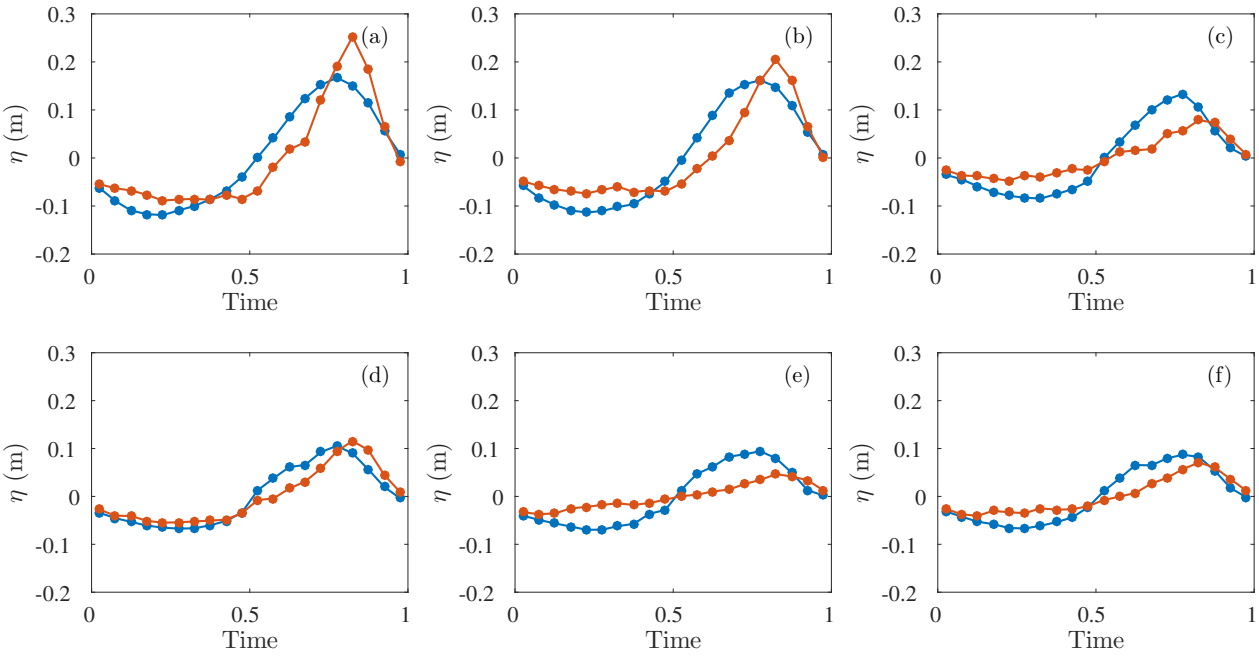

Figure 4.7 – The phase averaged sea surface elevation (for explanation see Section 3.2.3) at the locations of the instrument array for period P1, i.e. from 21:30 to 22:00 on 25-09-2016. The field data and the SWASH model output are plotted in respectively blue and orange. Figures are labelled from the most seaward measurement location towards the shore, with (a) wave gauge 1 (b) wave gauge 2 (c) frame 1 (d) wave gauge 3 (e) frame 2 (f) wave gauge 4.

4.2 The bed level change and the calibration results of the sand transport model

The root-mean-square error of the measured and modelled bed level change $E_{rms,zb}$ turned out to be minimal ($E_{rms,zb} = 0.0595$ m) for the best fit parameter $C_W = 5 \times 10^{-4}$, $C_C = 2 \times 10^{-3}$, $Ka = 1 \times 10^{-5}$ (m s), $\lambda_d = 5 \times 10^{-7}$. The B1 profile combined with the GPS data of 14:00 on 25-09-2016 was used as bed profile at the start of the simulation, which ended 25.5 hours later at 15:30 on 26-09-2016. The top panel of Figure 4.8 shows the bed profile at the start of the simulation (in black) together with the bed profile at the end of the simulation (in red). The berm around a cross-shore distance x of 150 m has steepened. The slope increased and a deeper trough is observed at the seaward side of the berm. In the middle panel of Figure 4.8, the measured bed level change over 25.5 hours is shown in blue and the modelled bed level change for the best fit parameters is shown in red. The model is able to reproduce the peak in the bed level change around 150 m, but the peak in the modelled bed level change is smaller. The trough in the bed level change is located more seaward in the model compared to the measured bed level change. The bottom panel of Figure 4.8 shows a colour plot of the

bed level change over 30 minutes as a function of the cross-shore distance x and time. The red colours indicate erosion and blue colours indicate accretion. The location of the shoreline varies over a cross-shore distance of 140 m to 200 m, which is related to the tides. Most of the bed level change occurs at the shoreline, with accretion of sand at the landward side of the shoreline and erosion of sand at the seaward side of the shoreline.

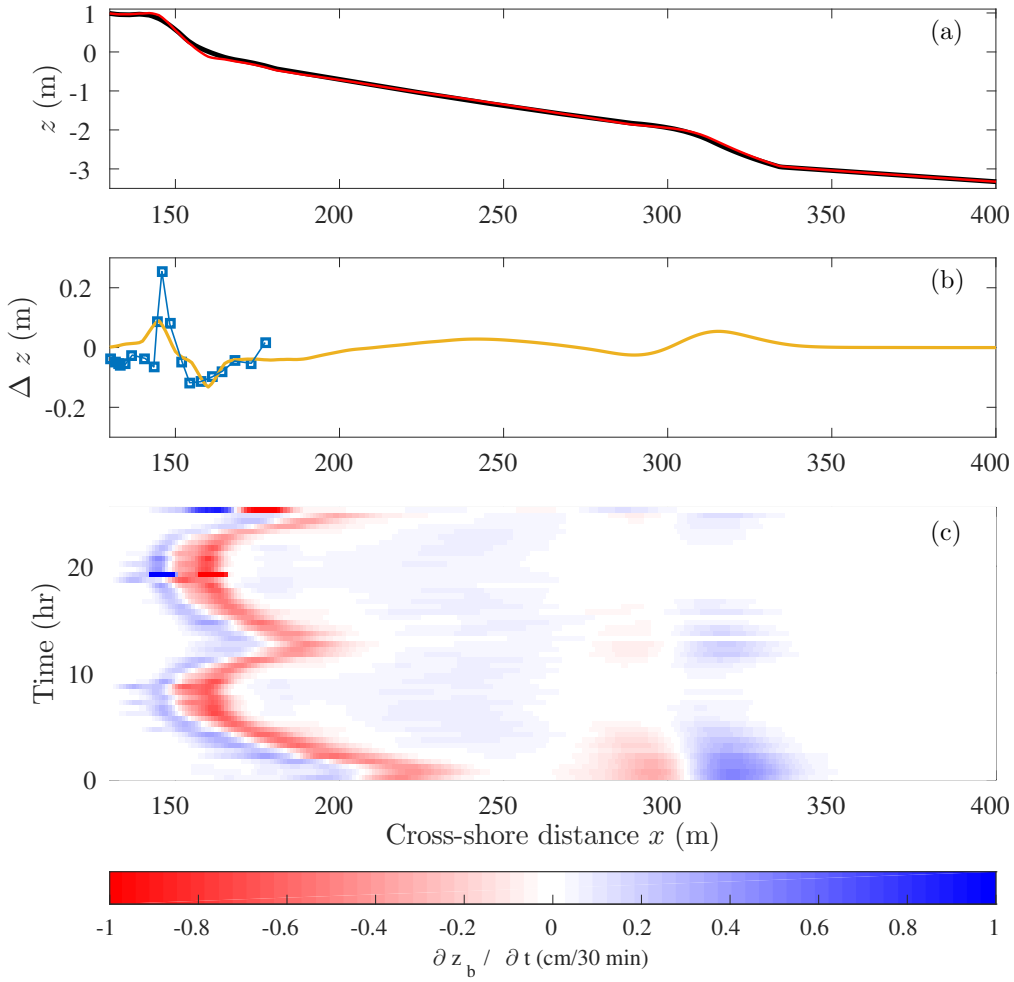

Figure 4.8 – (a) The bed profile at the start (14:00 25-09-2016) and end (15:30 26-09-2016) of the simulation in respectively black and red for the best fit parameters $C_W = 5 \times 10^{-4}$, $C_C = 2 \times 10^{-3}$, $Ka = 1 \times 10^{-5}$ (m s), $\lambda_d = 5 \times 10^{-7}$. (b) The measured and modelled bed level change over 25.5 hours in respectively blue and yellow. The measured bed level change is the difference between the GPS measurements on 25-09 and the interpolated GPS measurements of 26-09. (c) The modelled bed level change over 30 minutes as a function of the cross-shore distance x and the time. Positive values (blue) correspond to accretion and negative values (red) correspond to erosion.

4.3 The effect of the different transport terms

The total transport for the best fit parameter $C_W = 5 \times 10^{-4}$, $C_C = 2 \times 10^{-3}$, $Ka = 1 \times 10^{-5}$ (m s), $\lambda_d = 5 \times 10^{-7}$ is plotted in Figure 4.9 as a function of the cross-shore distance x and time. The contribution of the four components of the total transport are also shown in Figure 4.9 together with the bed profile at the start of the simulation to show the location of the berm around 150 m and the bar between 300 m and 350 m. The total transport Q_{tot} is onshore directed at the shoreline and seaward from x=330 m. In between the total transport is offshore directed. The transport due to waves Q_V and the acceleration-driven transport Q_A are only onshore directed, contrary to the diffusive transport Q_D that is solely offshore directed. The transport due to currents Q_C is offshore directed except at the shoreline. The unexpected onshore directed transport due to currents at the shoreline is due to model errors, since the sand transport model is not build for the swash zone along the shoreline. The acceleration-driven transport Q_A is small compared to Q_V and Q_C. The diffusive transport Q_D is extremely weak with a factor 100 smaller than the other transport terms.

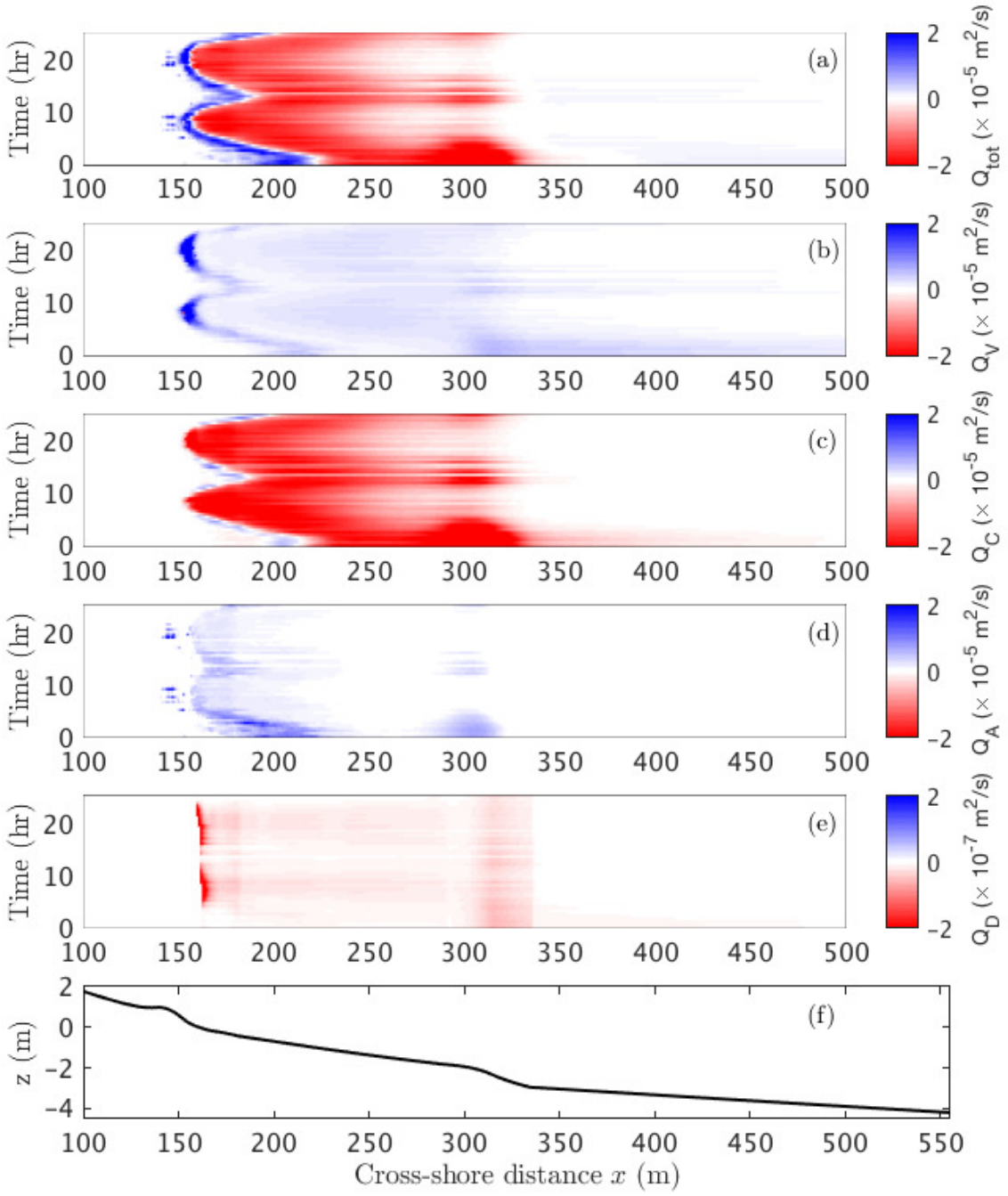

Figure 4.9 – (a) The total transport Q_{tot} as function of the cross-shore distance x and time for the best fit parameters $C_W = 5 \times 10^{-4}$, $C_C = 2 \times 10^{-3}$, $Ka = 1 \times 10^{-5}$, $\lambda_d = 5 \times 10^{-7}$. Blue colours indicate onshore transport and red colours indicate offshore transport. The transport driven by each terms of the total transport: (b) the transport due to waves Q_V, (c) the transport due currents Q_C, (d) acceleration driven transport Q_A and (e) the diffusive transport Q_D. (f) The bed profile at the start of the simulation (25-09-2016).

Chapter 5: Discussion

5.1 The hydrodynamics

5.1.1 Phase-averaged sea surface elevation

In Section 4.1.2, the modelled high frequency sea surface elevation was compared to the measured high frequency sea surface elevation. The waves in de model were more asymmetric and less random, which was also seen in the phase-averaged sea surface elevation. This might be due to the large distance (2 km) over which the waves travel from the seaward boundary towards the coast in the model. This gives the modelled waves a long time to become asymmetric. This issue is analysed by splitting the 2 km domain into an offshore part (x between 500 m and 2000 m), and a zone close to coast ($x < 500$ m). IIt is hypothesised that the wave asymmetry in the model decreases when only symmetric waves enter this zone close to beach. In the offshore domain, the waves still enter on the seaward boundary based on a JONSWAP spectrum with wave height from buoy. At a cross-shore distance x of 500 m, the significant wave height H_S and peak period T_p are determined. The wave height and period at $x = 500$ m are used as input variables for a JONSWAP spectrum at the seaward boundary of the smaller domain. This ensured that only symmetric waves enter the small domain in the modelling exercise. The simulations were performed using the B1 profile and the best fit parameters $\alpha = 0.5$, $\beta = 0.3$ and $n = 0.011$ m$^{-1/3}$s.

Figure 5.1 compares of the field data (blue, top panel), the model output of the original domain with a length of 2 km (orange, middle panel) and model output of the small domain with a length of 500 m (purple, bottom panel) for period P1. The blue and orange data correspond to the same data as Figure 4.6. The time series of the high frequency sea surface elevation η_{HF} show that the model output in case of the small domain compares well with the model output of the original domain. In both cases, the waves in the model output are more asymmetric and less random compared to the field data. In the right panel, the phase-averaged sea surface elevation is shown for the field data and the model for the two different domains. The peak in the wave frequency spectrum is smaller for the model with a domain length of 500 m and compares better with the field data than the model output with the original domain of 2 km. The trough is still long and shallow in the case of the small domain, which does not agree with the field data. Figure 5.2 shows the variance energy density wave spectra, with the field data and model output of the original domain in blue and orange respectively. The variance density spectrum of the model output of the small domain is shown in purple. The spectrum of the small model domain does not show a clear peak: the spectral

peak collapsed. Most of the energy is located in the low frequency domain. The modelled sea surface elevation did not become less peaky in case of the small model domain where only symmetric waves enter at $x = 500$ m. The waves become quickly asymmetric when they enter the domain. This shows that the sea surface variations are locally determined, as was earlier found by Doering and Bowen (1995).

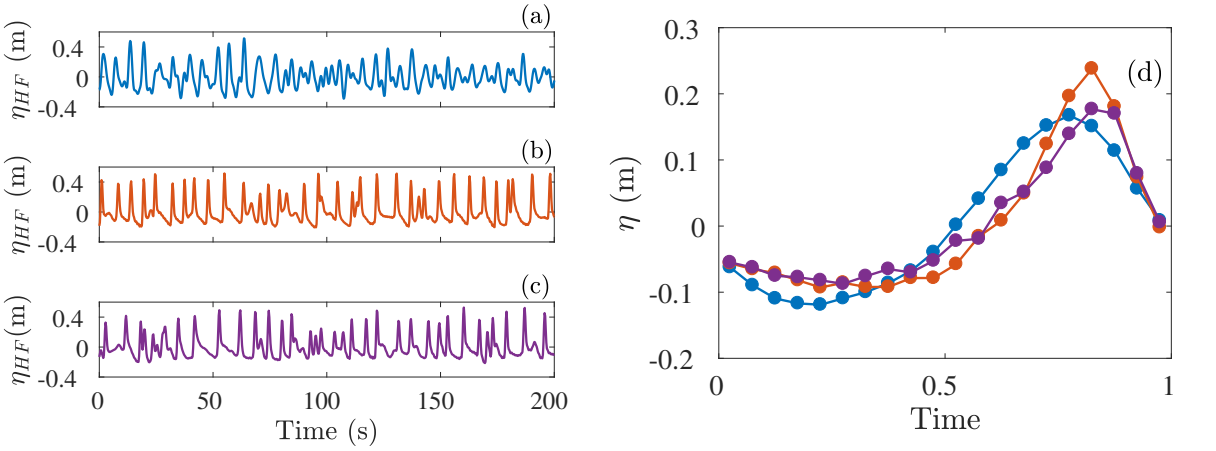

Figure 5.1 – The sea surface elevation time series of (a) the field data, (b) the model domain of 2 km and (c) the model domain of 500 m. (d) The average wave shape over 30 minutes for the three cases, where the colours correspond to the colours of the sea surface elevation. The model runs were done with $\alpha = 0.5$, $\beta = 0.3$ and $n = 0.011$ m$^{-1/3}$s for period $P1$, i.e. from 21:30 to 22:00 on 25-09-2016.

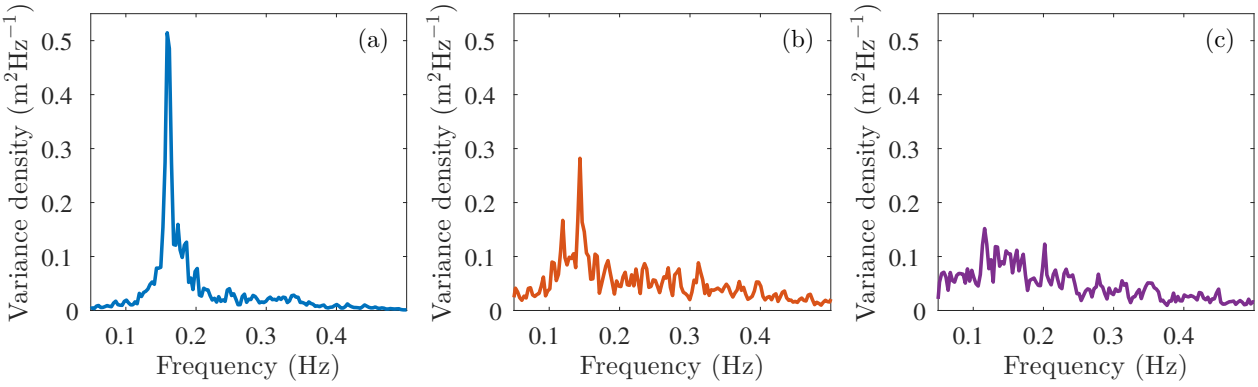

Figure 5.2 – The variance energy density spectra obtained from the sea surface elevation time series shown in Figure 5.1 of the three cases (a) the field data, (b) the model domain of 2 km and (c) the model domain of 500 m.

The collapse of the spectral peak in the smaller model domain is shown in Figure 5.3. The variance density spectra are plotted at different distances from the shore, from a cross-shore distance x of 450 m (a) to 200 m (e). In panels (a) to (d), the peak frequency is 0.16 Hz. In panel (b) at a cross-shore distance of 350 m, a second peak is found at a frequency of 0.14 Hz. The peak completely collapsed in panel (e), at a cross-shore distance x of 200 m, which

is at the same location as wave gauge 1. The peak frequency at the offshore boundary is still found in the variance density spectrum at a cross-shore distance of 225 m, panel (d), but not at a distance of 200 m. This might be related to the breaking of waves, which starts at around a cross-shore distance of 200 m.

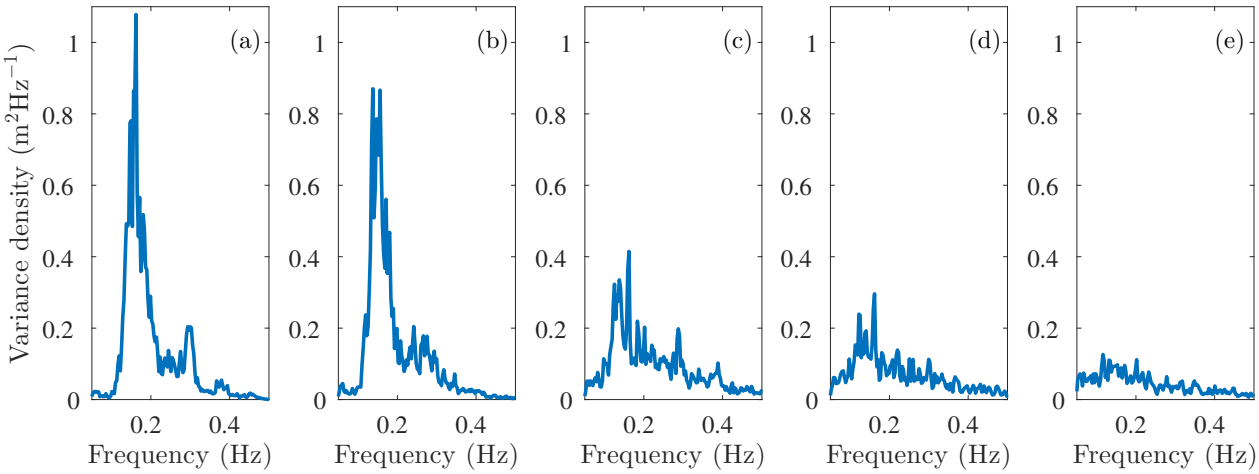

Figure 5.3 – The variance energy density spectra at different distance from the coast determined from the model output using the smaller domain of 500 m and the parameters $\alpha = 0.5$, $\beta = 0.3$ and $n = 0.011$ m$^{-1/3}$s for period $P1$, i.e. from 21:30 to 22:00 on 25-09-2016. (a) 450 m, (b) 350 m, (c) 250 m (d) 225 m (e) 200 m.

5.1.2 Model-data comparison of the hydrodynamical variables

The hydrodynamical variables determined from the field data are plotted in blue in Figure 4.5, together with the model output in orange. The measured significant wave height H_S increases from wave gauge 1 to wave gauge 2, followed by a decrease towards the shore. This means that the point of wave breaking is located landward of wave gauge 2. The modelled significant wave height H_S decreases from wave gauge 1 towards the shore, therefore the point of wave breaking is located seaward of wave gauge 1. The modelled and measured current is offshore directed. The modelled offshore directed current is related to the undertow (Svendsen, 1984). The measured offshore current is weaker than the modelled current. This night be due to the location of the instrument array, which can be located in a meander of the alongshore current or in the landward branch of a rip current (Masselink et al., 2014). An alongshore current can also result in a weaker cross-shore current. This will be discussed in Section 5.3.1. A local extremum in the measured current U_C is observed at the location of wave gauge 2. This local extremum is also observed in the modelled current around 160 m. The asymmetry of the high frequency sea surface elevation η_{HF} increases in absolute value towards the coast. An increase in the wave asymmetry towards the coast was also found by Elgar and Guza (1985) and Ruessink et al. (2012).

The modelled skewness of the high frequency sea surface elevation η_{HF} slightly increases from wave gauge 1 to wave gauge 2, followed by a decrease towards the shore. In the field data, the skewness first increases towards frame 3 followed by a decrease towards the shore.

Elgar and Guza (1985) found that the maximum of the skewness is located more seaward than the maximum in the wave asymmetry, which is also true for both the field data and the model data. Ruessink et al. (2012) found that the skewness is largest in the transition zone and decreases towards the coast when the waves start to break. The discrepancy in the wave asymmetry and skewness determined for the sea surface elevation between the field data and the model is caused by the difference in location of wave breaking. The asymmetry increases and the skewness decreases landward of the point of wave breaking. Because this point is located more seaward in the model than in the observations, the skewness starts to decrease and the asymmetry starts to increase more seaward in the model compared to the field data. The skewness and the asymmetry determined from the modelled high frequency velocity do not agree with the field data. The difference in the values can be related to the underestimation of the mean current by the model, but this cannot explain the difference in cross-shore distribution of the skewness. The skewness determined from the velocity decreases towards the shore in the field data, while the model output shows an increase towards the shore. This is also seen in the data and model output of period P2 in Appendix D.

A previous comparison between the SWASH model output and field data was done by Brinkkemper (2013) for a field campaign at the Dutch coast near Egmond aan Zee. Brinkkemper (2013) used only one vertical layer in the SWASH model, but a smaller spatial grid size of 0.2 m compared to 1 m in this study. Good agreement was found between the modelled and measured high frequency wave heights. The asymmetry and skewness determined from the modelled sea surface elevation agreed less with the model. Brinkkemper (2013) concluded that this might be due to the already high non-linearity of the time-series used at the seaward boundary. The effect of the non-linearity in the sea surface elevation at the sea boundary was investigated in Section 5.1.1, where it was concluded that the skewness and asymmetry are not determined by the boundary conditions, but are locally determined. The modelled asymmetry and skewness agreed better with the data at more seaward locations compared to the locations close to the shoreline. In some cases, investigated by Brinkkemper (2013), the modelled asymmetry increased towards the coast contrary to the field data that decreased towards the coast. This was also found for the skewness in this study. The root-mean-square error of the modelled and measured skewness and asymmetry is largest close to the shoreline. Brinkkemper (2013) also compared the wave energy spectra of the model output and the observations. The spectra were very similar, except for the low-frequencies. The energy-density for the low-frequencies was over-predicted, which was also found in this study. The spectral peak decreases significantly from the seaward boundary towards the coast, due to energy transfer to the lower frequencies. At the location of the measurement array, the spectral peak has collapsed because all the energy transferred to the lower frequencies.

The discrepancy between the cross-shore distribution of the modelled and observed skewness determined from the velocity has obvious consequences. The velocity skewness and velocity asymmetry are the two mechanisms resulting in onshore sand transport. The intrawave orbital motion needs to be described realistically (Ruessink et al., 2012) in order to achieve realistic results of the sand transport simulations. In the study of Fernández-Mora et al. (2015), the modelled velocity and acceleration skewness showed a similar spatial pattern compared to the observations. Fernández-Mora et al. (2015) used the intrawave orbital

velocity parametrization of Ruessink et al. (2012) instead of modelling the wave velocities with a hydrodynamical model. The parametrization of Ruessink et al. (2012) simulates the asymmetry and skewness realistically and was also used by Dubarbier et al. (2015). However, the idea of this research project was to simulate the velocity of every wave separately and rather than the use of a parametrization of the wave velocity. An alternative to the SWASH model for solving the wave-velocities are Boussinesq-type models. The Boussinesq model of Bayram and Larson (2000) was able to model the sea surface time series in good agreement with field measurements. However, these simulations were performed 125 to 150 m from the shoreline, compared to 10 to 70 m from the shoreline as was done in this research project. Overall, studies that compare the velocity skewness and asymmetry from model simulation with field data are scarce. Since the velocity skewness and asymmetry are important to simulate the sand transport realistically, it is recommended to improve the model simulation of the wave velocity in the surf zone and validate the modelled velocity skewness and asymmetry with field data.

5.2 The effect of the different sand transport mechanisms

The contribution of the four sand transport mechanisms to the total transport was shown in Figure 4.9. The figures have the same values in the colour bar, except the diffusive transport Q_D which is two orders of magnitude smaller than the other mechanisms. The diffusive transport is offshore directed in the whole domain. This finding contrasts Dubarbier et al. (2015), who found onshore directed transport due to slope effects at the shoreline. The difference is possibly due to the steep berm in the bed profile, which was did not exist in the bed profile of Dubarbier et al. (2015).

The transport due to waves Q_V and the acceleration-driven transport Q_A are onshore directed, which was also found by Dubarbier et al. (2015). The transport due to waves Q_V starts further offshore compared to the acceleration driven transport Q_A. This is related to the cross-shore distribution of the skewness and asymmetry, waves first become skewed in the shoaling zone before they become asymmetric in the surf zone (Elgar and Guza, 1985; Ruessink et al., 2012). The magnitude of transport due to the waves is larger than the acceleration-driven transport, leading to an important finding that the velocity skewness transport mechanism dominates over the velocity asymmetry mechanism.

The transport due to currents is offshore directed, except at the shoreline where Q_C is onshore directed. This is not supported by the simulations of Dubarbier et al. (2015), who found offshore transport due to currents at the shoreline. The sand transport model was not build to simulate the processes in the swash zone, which can explain the discrepancy in the direction of Q_C at the shoreline. Transport by the currents starts more onshore compared to the transport due to waves. The transport is driven by the undertow which increases when waves start to break. This happens landward of the shoaling zone in the surf zone.

In the shoaling zone, the total transport is dominated by the onshore transport due to

waves. The total transport in the surf zone is offshore directed and dominated by the transport due to currents. Close to the beach, the total transport is onshore directed. The main contribution is the transport due to the waves, but the acceleration-driven transport and transport by currents also contribute to the onshore directed transport close to the beach. These findings can be compared to the findings of Fernández-Mora et al. (2015), who found that the shoaling zone was dominated by velocity skewness similar as in the present study. However, the dynamics in the inner surf zone were dominated by the velocity asymmetry in the study of Fernández-Mora et al. (2015) contrary to currents as was found in the present study. The difference might be caused by the overall small contribution of the velocity asymmetry transport in my simulations.

The moving shoreline over time is observed in Figure 4.9 that shows the periods of high water and low water. In the domain from 300 m to 350 m, the direction of transport depends on the water level. During low water, the offshore transport by currents dominates while during high water the onshore transport by the waves dominates. The dependency on the water level is related to the location of wave breaking and was also found by Dubarbier et al. (2015). During low water, sand is transported above the bar around 300 m. The transport above this bar is most clear at the start of the simulation and is dominated by the offshore transport by currents, which could indicate wave breaking above the bar. The bed level change as function of time and cross-shore distance in Figure 4.8 shows that this transport results in slight erosion at the landward side of the bar and accretion at the seaward side of the bar, leading to flattening of the bar and slight offshore bar migration.

5.3 Limitations in the method

The aim of this thesis was to model the sand transport at Vejers beach in Denmark during low energy conditions. To achieve this goal, a combination of the hydrodynamic SWASH model and a newly build sand transport model was used. The limitations in the field data and the sand transport model are discussed, followed by the limitations related to the model assumptions of the SWASH model.

The field data was collected over a period of 4 weeks, which was not necessary for this research project where only two tidal cycles are modelled. The spatial resolution of the field data was scarce, especially the velocity was only measured at three points over a distance of 20 m. The bed level measurements only extended till the end of the intertidal zone. No bathymetric data further than a cross-shore distance of 185 m was available for the modelled period. Therefore, the model already starts with an inaccuracy in the input bathymetry which will result in an error in the sand transport model. The influence of the bed profile on the hydrodynamics and the sand transport is discussed in more detail in Section 5.4. In this research project, the calibration of the hydrodynamic model and the sand transport model is done using field data over a cross-shore distance of only 50 m in the intertidal zone. Next time it would be advised to also perform velocity, pressure and bed height measurements outside of the intertidal zone. Inside the intertidal area, the model deals with grids that are dry at some moments and wet at other moments. This can cause complications in the calibration process.

The sand transport formulas used are relative simple. Only one grain size was used instead of a mixture of grain sizes. The medium grain size during the field campaign varied between 180 μm and 240 μm. The grain size is an important sand property, since it influences the fall velocity and the critical shear stress. The settling lag of sand is not included in the sand transport formulas. The settling lag can result in onshore net transport under asymmetric waves, called the phase lag effect. Sand stirred during the trough wave phase, when the flow is offshore directed, has not settled at the end of the phase and is transported during the crest phase, when the flow is onshore directed. This effect is important for fine sand, but in case of medium sand (200 μm) the phase lag effect is of minor importance compared to the total net transport (Ruessink et al., 2011). Van der A et al. (2013) stated that phase lag effects are important of fine sand and rippled beds. No ripples were observed on 25-09-2016 and 26-09-2016 (Brinkkemper et al., 2017) and the sand at Vejers beach can be categorized as medium, which justifies excluding phase lag effects in the sand transport formulas.

The calibration of the SWASH model was done by varying the constants one by one and finding the value of that constant for which the total root-mean-square error is smallest. Varying the constants one by one means that not all combinations of the parameters are tested. With this method, there is no guarantee that the absolute minimum is found, like it is the case for the method of steepest descent (Press et al., 1987). However, this method was applied due to time limits and limited computational power.

The model simulations are only done in the cross-shore direction, which means that the alongshore processes are ignored. The shortcoming of the model related to the alongshore current and alongshore variability will be discussed below. Another process that is not included in the model is the effect of tidal currents. Tidal currents need to be considered in tidal inlets, where the currents are approximately 1 m/s. Tidal currents in the near-shore zone are small and often neglected in models. Finally, the effect of wind was not included, as is the case for most of the models and studies (e.g. Dubarbier et al., 2015; Fernández-Mora et al., 2015). An detailed analysis of the effect of the wind on the hydrodynamics is given in Appendix E.

5.3.1 Alongshore current and alongshore variability

In this model, the hydrodynamics and the sand transport are only computed in the cross-shore direction. An alongshore current can transport sand in the alongshore direction and influences the wave velocity and the current. Alongshore currents are driven by the breaking of obliquely incident waves, where the direction of the current depends on the incident wave angle (Masselink et al., 2006). The cross-shore current and wave velocity are influenced by the alongshore current through shear waves. Shear waves are alongshore propagating oscillations of the mean alongshore current with a period of a few minutes and an alongshore wavelength of a few hundred meters (Noyes et al., 2005). Shear waves are the result of a shear instability of the alongshore current (Bowen and Holman, 1989) and mix momentum across the surf zone. This results in an extra term in the Reynold stresses, which influences the flow velocities. The wave-current interaction influences the wave energy in the surf zone

and decrease sthe offshore directed current (Ozkan-Haller, 2003).

The sand transport formulas are applicable in the case of alongshore uniformity. Alongshore variations in the bathymetry influence the sand transport through the wave height and asymmetry, which are locally controlled (Doering and Bowen, 1995). Alongshore variability in the bathymetry can also generate cell circulations, for example a rip current circulation (Garnier et al., 2008; Castelle et al., 2010). A rip current circulation consists of alongshore oscillating bar where wide shallow parts are alternated by narrow deep sections (Garnier et al., 2008). The narrow deep sections are called rip channels, which have a strong offshore directed current in them. Above the shallow parts, the current is onshore directed resulting in a cell circulation that drives currents along the coast. The bar and rip channels influence the point of wave breaking and the cross-shore wave velocity. (Garnier et al., 2008)

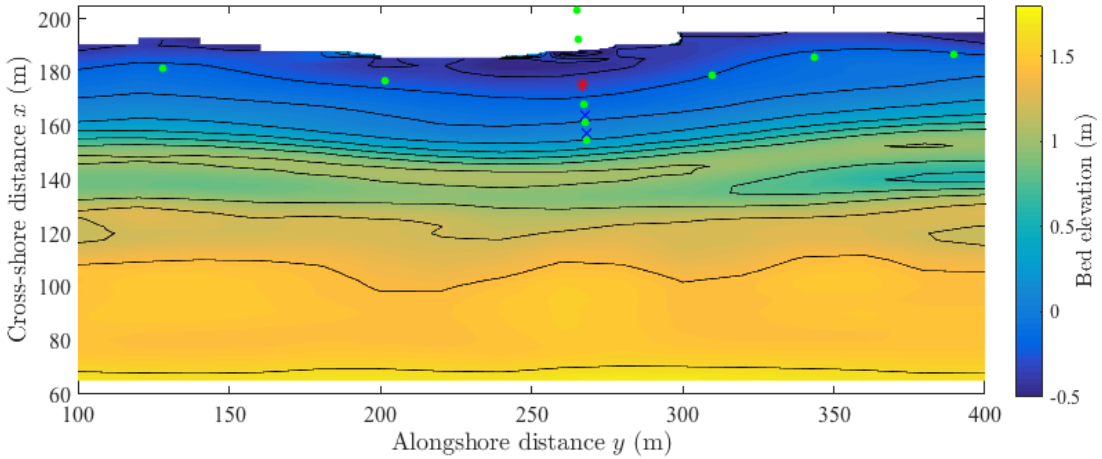

Figure 5.4 – Bathymetric map of the study area on 27-09-2016 with 0.20 m spaced contours. The locations of the instruments are indicated: wave gauges (green dots), frame 1 (red cross), frame 2 and frame 3 (blue crosses). Adapted from Naus (2017).

The alongshore variability during the field campaign was investigated by Naus (2017). In Figure 5.4, the bathymetric map of the study area on 27-09-2016 is shown. Not enough GPS data were available to make a detailed bathymetric map on 25 September or 26 September, but the alongshore bathymetry was similar to the bathymetry on 27 September. The beach was in an intermediate state, with a rhythmic bar and beach (RBB, Wright and Short, 1984). The map shows a crescentic shape of the coastline, which is also reflected in the intertidal bar (around 140-160 m in the cross-shore distance). The cross-shore instrument array was located at an embayment in the shoreline (Brinkkemper et al., 2017). The alongshore variability influenced the significant wave height H_S. The observed H_S at the instrument array was highest of the alongshore wave gauges, up to 1.8 times higher as the observed H_S of the wave gauge at a alongshore distance of 340 m.

During the simulated period from 14:00 on 25-09-2016 to 15:30 on 26-09-2016, an alongshore current V_{lsc} up to 0.60 m/s was measured (Table 5.1). The incident wave angle at the offshore

wave buoy varied between -35° to - 55° during the simulation (see Figure 3.2), which could be an explanation of the large measured alongshore current. Sand is transported along the Danish west coast towards the south. Kaergaard et al. (2012) stated that the alongshore sediment transport on the beach face at Srd. Holmslands Tange (50 km north of Vejers beach) is 2.1 million m^3/year.

Fernández-Mora et al. (2015) included the alongshore current V_{lsc} in the mean current $\vec{U}_M$ defined as

$$\vec{U}_M(x,y) = U_C(x)\,\hat{x} + V_{lsc}\,\hat{y}. \tag{5.1}$$

with U_C the mean cross-shore current. The total flow velocity $\vec{U}_T$ becomes

$$\vec{U}_T(x,y,t) = U_W(x)\,\hat{x} + U_C(x)\,\hat{x} + V_{lsc}\,\hat{y}, \tag{5.2}$$

and the equation for the sand transport by the current becomes

$$Q_C(x) = \frac{C_C}{(s-1)g}\left[\frac{\epsilon_B}{\tan\phi}\left\langle|\vec{U}_T(x,y,t)|^2\right\rangle U_C(x) + \frac{\epsilon_S}{W_S}\left\langle|\vec{U}_T(x,y,t)|^3\right\rangle U_C(x)\right]. \tag{5.3}$$

The average current over the simulation period and the three frames is 0.25 m/s. The effect of the alongshore current on the total transport and bed level change is determined using Equation 5.3 and the average current (V_{lsc}=0.25 m/s) for the first simulation period, from 14:00 to 14:30 on 25-09-2016 (see Appendix C). The total cross-shore transport Q_{tot} and the bed level change over 30 minutes Δz are shown in Figure 5.5 for the case of no alongshore current (blue) and an alongshore current of 0.25 m/s. The alongshore current increases the total offshore directed transport between 250 m and 350 m. The influence of the alongshore current on the bed level change is small. The peak in the bed level change around 350 m is slightly higher and the trough around 225 m is lower in the case of an alongshore current.

The wave-current interaction is not included in this method. The transport by the waves and the acceleration-driven transport are not affected, only the magnitude of the total transport has changed. The alongshore current influences the waves and currents in various ways. The alongshore current measured during the field campaign were significant, so it is recommended to take the alongshore current into account in future research. The method of Fernández-Mora et al. (2015) is not recommended, because it only influences the transport by the currents while the other effects of the alongshore current are neglected. The wave-current interaction can be included by doing 2D simulations in the SWASH model, computing the

Table 5.1 – The measured maximum alongshore current V_{lsc} and the measured mean alongshore current V_{lsc} over the period simulation period (14:00 25-09-2016 to 15:30 26-09-2016) at the location of the three frames.

	Frame 1	Frame 2	Frame 3
maximum V_{lsc} (m/s)	0.60	0.68	0.54
mean V_{lsc} (m/s)	0.32	0.27	0.14

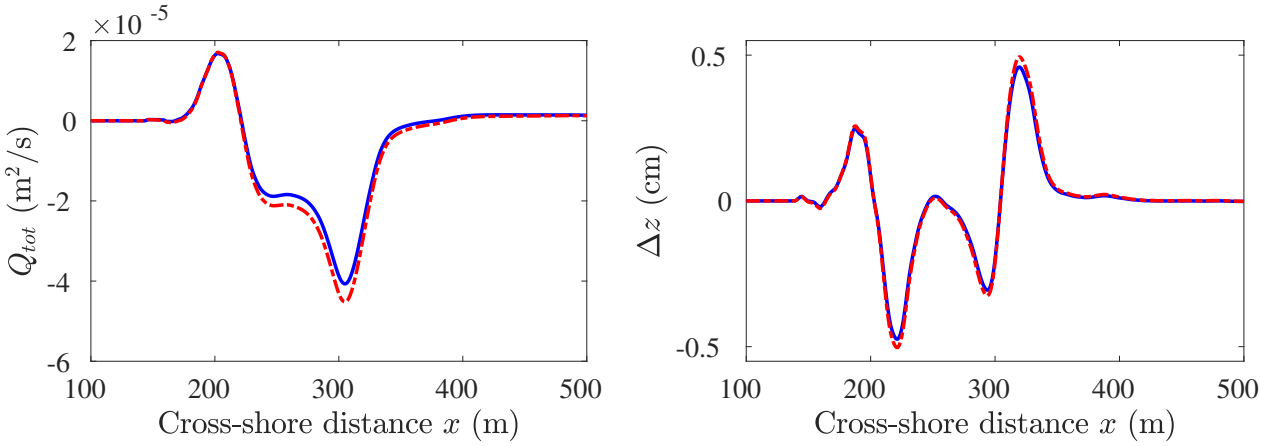

Figure 5.5 – The total cross-shore transport Q_{tot} and the bed level change over 30 minutes Δz in the case of no alongshore current (blue) and an alongshore current of 0.25 m/s (red, dashed) for the first simulation period, from 14:00 to 14:30 on 25-09-2016 (see Appendix C).

flow velocities in the alongshore and cross-shore direction. In the 2D simulations, the incident wave angle can be included in the boundary conditions at the seaward boundary. Using the SWASH model in 2D and computing the flow velocities in the alongshore and cross-shore direction is the best way to include the effect of the alongshore current. However, the 2D simulations increase the computational time and the amount of data, so more computational power and storage space would be necessary.

5.4 The influence of the bed profile on the sand transport

For the calibration of the bed profile in the SWASH model, the BAR profile had the smallest total E_{rms}, but was dismissed because of a larger error in the significant wave height and its inability to simulate the local extremum in the mean current. The calibration of the bottom friction coefficient n and the wave breaking parameters α and β was also done for the BAR profile (see Appendix F). The best fit parameters for the BAR profile are similar to the best fit parameters using the B1 profile: $\alpha = 0.6$, $\beta = 0.3$ and and $n = 0.011$ m$^{-1/3}$s. The total normalised root-mean-square error $E_{rms,tot}$ of the BAR profile did not become smaller than 0.75. The $E_{rms,tot}$ for the best fit parameters of the SWASH model with the B1 profile was 0.27, which justifies using the B1 profile.

The sand transport and bed level change is also computed for the BAR profile with the transport parameters of $C_W = 1 \times 10^{-3}$, $C_C = 1 \times 10^{-3}$, $Ka = 1 \times 10^{-5}$ (m s), $\lambda_d = 5 \times 10^{-7}$, using the best fit parameters of the SWASH model ($\alpha = 0.6$, $\beta = 0.3$, $n = 0.011$ m$^{-1/3}$s). The bed profile at the start (black) and end of the simulation (red) is shown in the top panel of Figure 5.6. In the middle panel the measured and modelled bed level change is plotted in blue and yellow respectively. The modelled bed level change does not compare well with the measured bed level change. Accretion was measured around 150 m, while model simu-

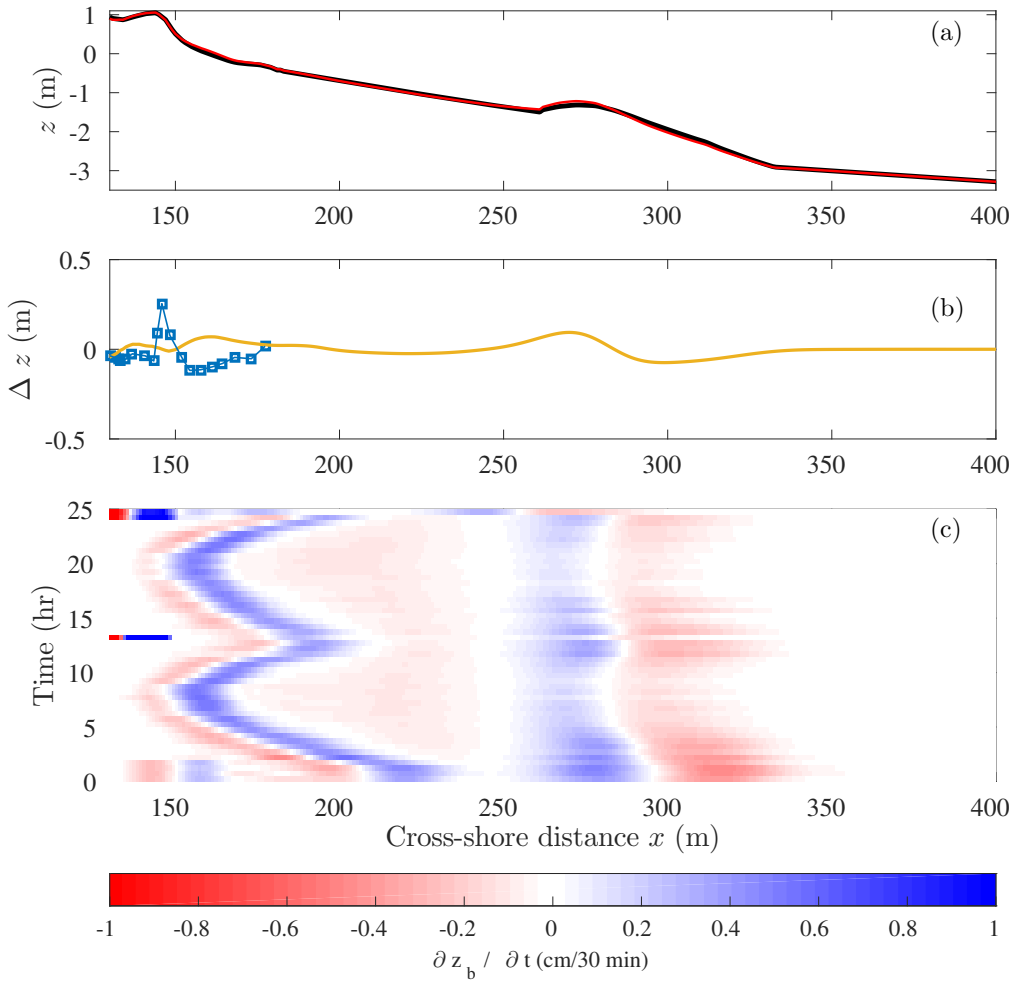

Figure 5.6 – The bed level change using the BAR profile as bathymetry using the best fit parameters $C_W = 5 \times 10^{-4}$, $C_C = 2 \times 10^{-3}$, $Ka = 1 \times 10^{-5}$ (m s), $\lambda_d = 5 \times 10^{-7}$. (a) The bed profile at the start and end of the simulation. (b) The measured and modelled bed level change over 26 hours in respectively blue and yellow. (c) The modelled bed level change over 30 minutes as a function of the cross-shore distance x and the time. Positive values (blue) correspond to accretion and negative values (red) correspond to erosion.

lates erosion at this location. Accretion occurs 30 meters seaward in the model compared to the field data. The model predicts accretion on the landward side of the bar and erosion at the seaward side of the inner bar between 250 and 350 m, leading to slight onshore bar migration. This is contrary to the slight offshore bar migration simulated using the B1 profile.

The total cross-shore transport Q_{tot} is plotted in Figure 5.7 as function of the cross-shore distance and time, together with the contribution of the four sand transport terms. The total transport at the shoreline is onshore directed, followed by offshore directed transport in the surf zone. Seaward of the bar, the transport is small and onshore directed. The transport above the bar is stronger during high water than low water.
As was found for the results of the B1 profile, the transport due to waves and asymmetry is onshore directed. The transport due to waves is larger than the acceleration-driven transport,

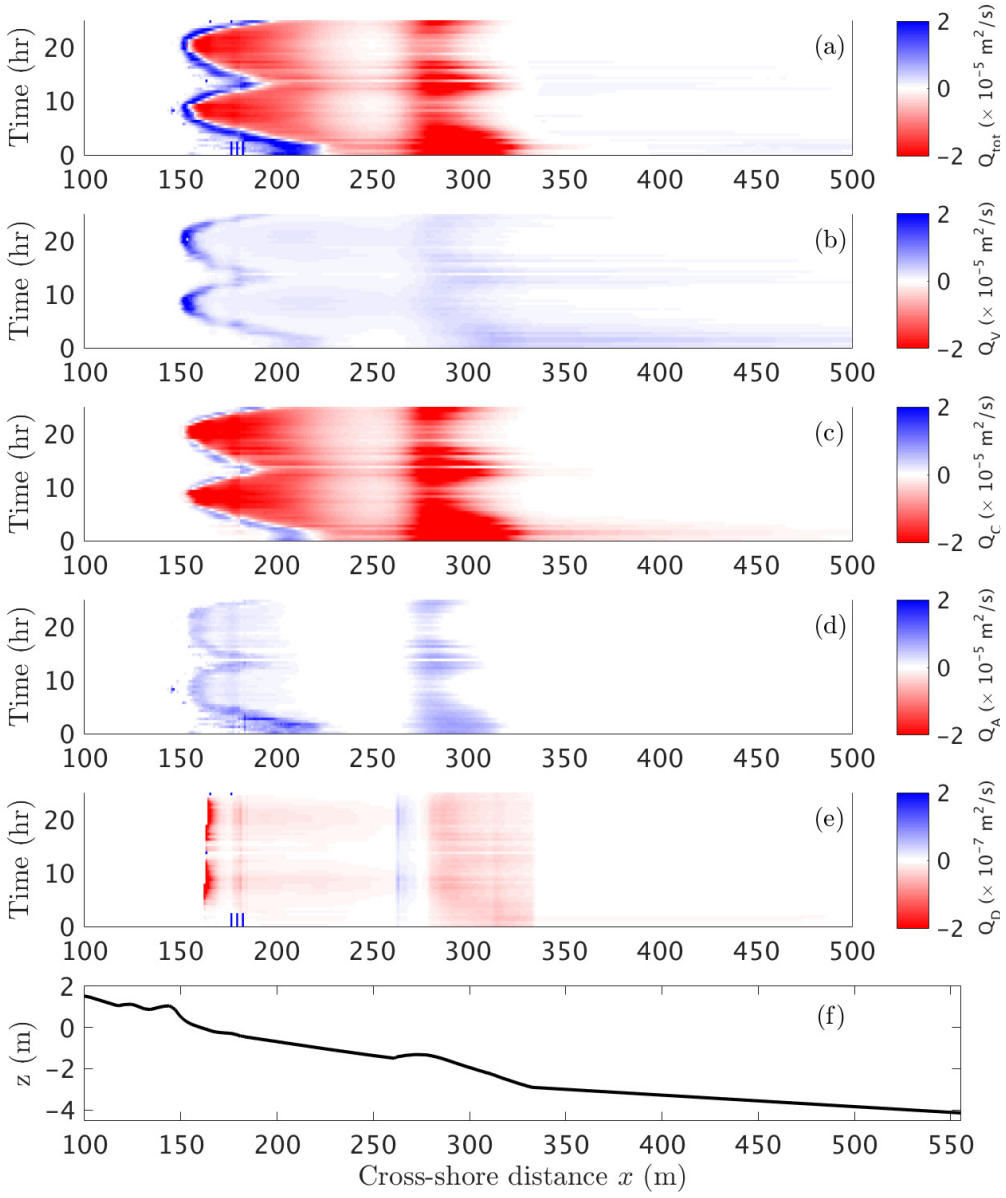

Figure 5.7 – The transport using the BAR profile as bathymetry using the best fit parameters $C_W = 5 \times 10^{-4}$, $C_C = 2 \times 10^{-3}$, $Ka = 1 \times 10^{-5}$ (m s), $\lambda_d = 5 \times 10^{-7}$. (a) The total transport Q_{tot} as function of the time and cross-shore distance x. Blue colours indicate onshore transport and red colours indicate offshore transport. The transport driven by each terms of the total transport: (b) the transport due to waves Q_V, (c) the transport due currents Q_C, (d) acceleration driven transport Q_A and (e) the diffusive transport Q_D. (f) The bed profile at the start of the simulation.

but this is because the same values of C_W and Ka are used. The transport due to currents is offshore directed, except at the shoreline which was also the case for the B1 profile. The diffusive transport is onshore directed at the landward side of the bar and offshore directed on the seaward side of the bar, leading to a sand deficit on top of the bar. This means that the diffusive transport tries to flatten the bar, as was the transport defined. However, the diffusive transport is a factor 100 smaller than the other transport terms so the bar flattening is not effective.

Due to the large bar in the BAR profile compared to the bar in the B1 profile, the transport above the bar is larger for all four terms. The transport above the bar of the BAR profile is still clearly visible in the second high water, while the transport above the bar of the B1 profile was small during the second high water. Overall, the difference in transport between the B1 profile and BAR profile is small, since the sand transport model is not calibrated for the BAR profile due to time limits. The modelled and measured bed level change do not compare well. Once the sand transport model is calibrated for the BAR profile, the sensitivity of the sand transport model to the input bed profile can be determined. However, the easiest way to decrease the uncertainty in the sand transport related to the bed profile is to measure the complete bathymetry during the field campaign. When the complete bathymetry at the start and end of the simulation period is known, the modelled and measured bed level change can be compared over a large distance and the input bed profile for the models do not need to be adapted any more.

Chapter 6: Conclusions

The relative contribution of acceleration-driven transport and the transport due to waves to the onshore sand transport during low to moderate energy conditions was investigated in a combined data-model study. Measurements of flow velocities, sand concentrations and the morphology in the intertidal area were performed over a period of 4 weeks at Vejers beach, a sandy uninterrupted coast along the Danish North sea coast. The hydrodynamical SWASH model was used to simulate the water motion and wave conditions measured during the field campaign. A sand transport model was build based on the formulas of Fernández-Mora et al. (2015) including four transport mechanisms: a) transport by the waves, b) joint action of stirring of sand by waves and transport by currents, c) the acceleration-driven transport and d) the diffusive transport. The bed level change over 25.5 hours was computed using the modelled total cross-shore sand transport and compared to the observed bed level change in order to calibrate the sand transport model. The relative contribution of the four transport mechanisms to the total cross-shore transport were evaluated as a function of time and distance.

The total normalised root-mean-square error between the model output and the field data determined the skill of the fully wave phase-resolving SWASH model for simulating the hydrodynamics at Vejers beach during fair weather conditions. The values of the best fit parameters of the SWASH model were a Manning's roughness coefficient $n = 0.011$ m$^{-1/3}$s and the wave breaking parameters $\alpha = 0.5$ and $\beta = 0.3$. For this combination of the calibration parameters and the B1 profile, the total normalised root-mean-square error was smallest with a value of 0.27. From the comparison of the SWASH model output with the field data, it was concluded that the SWASH model is able to simulate the significant wave height in good agreement with the field data. However, the simulation of the current, skewness and asymmetry of the sea surface elevation and wave velocity need to be further improved.

The root-mean-square error of the measured and modelled bed level was 0.0595 m for the best fit parameter of the sand transport model: the wave friction coefficient $C_W = 5 \times 10^{-4}$, the current friction coefficient $C_C = 2 \times 10^{-3}$, the calibration constant of the acceleration-driven transport $Ka = 1 \times 10^{-5}$ and the coefficient of the diffusive transport $\lambda_d = 5 \times 10^{-7}$. Overall, a good agreement between the modelled and observed bed level change over 25.5 hours was found. The model was able to reproduce the peak in the observed bed level change around a cross-distance of 150 m, but the peak in the modelled bed level change was smaller. Also, the trough in the modelled bed level change was located more seaward compared to the observed bed level change.

The results of the modelling exercise revealed the relative contribution of the four transport mechanisms to the total cross-shore transport and showed that the velocity skewness transport mechanism dominates over the velocity asymmetry mechanism. The direction of the total cross-shore sand transport depends on the cross-shore location and time. In the shoaling zone, the total transport is dominated by the onshore transport due to waves. While in the surf zone, the total transport is offshore directed and dominated by the transport due to currents. Close to the beach, the total transport is onshore directed. The main contribution is the transport due the waves, but the acceleration-driven transport and transport by currents also contribute to the onshore directed transport close to the beach. The results also showed that during low water, the offshore transport by currents dominates at the edge of the shoaling zone while during high water the onshore transport by the waves dominates.

The model simulations of the wave velocity in the surf zone need to be improved to achieve more realistic results of the onshore sand transport simulations. Comparisons between the velocity skewness and asymmetry determined from modelled sea surface elevation using a phase-resolving model with field data are scarce. To improve the model simulations, more data-model studies focussed on the wave non-linearities are recommended. In this research project, the calibration of the hydrodynamical model and the sand transport model is done using field data over a cross-shore distance of only 50 m in the intertidal zone. Inside the intertidal area, the model deals with grids that are dry at some moments and wet at other moments which can cause numerical complications. Field data outside of the intertidal area should be gathered to calibrate the models. Simulations with the hydrodynamical model in the alongshore and cross-shore direction need to be done to include the effect of the alongshore currents, which were strong during the field campaign. The modelled time period can be increased from 25.5 hours to a couple of days to reduce errors and investigate the dependency of the transport terms on the wave conditions.

Acknowledgement

I would like to thank my supervisor Huib de Swart for sharing his knowledge, his engagement throughout the learning process of this master thesis and his feedback. I would also like to thank Gerben Ruessink, my second supervisor, and Joost Brinkkemper for assisting me during my first field work campaign and showing how all the instruments work. Special thanks to my field work buddies Ivo and Johnny for a great field work experience and the discussions during the lunch breaks in Utrecht. I want to thank Jessica, for the lovely tea and colouring breaks. And finally, I want to thank my dad, Jessica, Pauline and Hannah for reading and correcting my thesis during their holiday.

Appendix A: Locations of the instruments in the cross-shore array

Table A.1 – The locations of the instruments in the cross-shore measurement array with y the along-shore distance and x the cross-shore distance. The cross-shore distance x is defined 0 m at the top of the dunes.

	x (m)	y (m)
Pressure sensor of Frame 1	175.49	266.67
ADV 1 of Frame 1	177.00	268.12
Frame 2	163.91	267.63
Frame 3	157.36	268.04
Wave gauge 1	203.15	264.88
Wave gauge 2	192.58	265.55
Wave gauge 3	168.09	267.41
Wave gauge 4	161.27	268.01
Wave gauge 5	154.52	268.19

Appendix B: Skewness and Asymmetry

The skewness Sk and asymmetry As are defined as

$$Sk = \frac{<\eta^3>}{<\eta^2>^{3/2}} \tag{B.1}$$

$$As = \frac{<H(\eta)^3>}{<\eta^2>^{3/2}} \tag{B.2}$$

with η the sea surface elevation and H the Hilbert transform (Elgar, 1987).

A skewness function is incorporated in Matlab. The skewness of a data set is more general defined as a measure of the asymmetry of the data around the mean μ. A data set with a negative skewness means that the data are spread out more towards the left of the mean, while a positive skewness means that the data are spread out more towards the right. The skewness of a symmetric distribution, for example a normal distribution, is zero. Following the definition of the Matlab function, the skewness of a distribution is defined as

$$s = \frac{E(x-\mu)^3}{\sigma^3} = \frac{\frac{1}{n}\sum_{i=1}^{n}(x_i - \bar{x})^3}{\left(\sqrt{\frac{1}{n}\sum_{i=1}^{n}(x_i - \bar{x})^2}\right)} \tag{B.3}$$

where μ is the mean of x, σ is the standard deviation of x, and $E(t)$ represents the expected value of the quantity t. The skewness function is also used to compute the asymmetry using the imaginary part of the Hilbert function in Matlab. For example, the asymmetry of the velocity u is computed as
As = skewness(imag(hilbert(u)))

Appendix C: Table of the input variables of the 52 periods

Table C.1 – The still water depth (STW), the significant wave height H_S and the peak period T_p for the 52 periods used in the calibration of the sand transport model.

t	Date	STW (m)	H_S (m)	T_p	t	Date	STW (m)	H_S (m)	T_p
1	25/09 14:00	-0,68	1,22	6,7	27	26/09 03:00	-0,39	1,00	6,4
2	25/09 14:30	-0,73	1,23	6,2	28	26/09 03:30	-0,32	1,01	4,2
3	25/09 15:00	-0,70	1,24	6,5	29	26/09 04:00	-0,28	0,95	6,8
4	25/09 15:30	-0,67	1,25	6,5	30	26/09 04:30	-0,23	0,96	6,3
5	25/09 16:00	-0,61	1,24	6,3	31	26/09 05:00	-0,19	0,96	5,3
6	25/09 16:30	-0,49	1,26	6,4	32	26/09 05:30	-0,13	0,96	4,9
7	25/09 17:00	-0,44	1,21	6,3	33	26/09 06:00	-0,06	0,94	7,1
8	25/09 17:30	-0,36	1,18	6,0	34	26/09 06:30	-0,01	0,94	6,1
9	25/09 18:00	-0,27	1,15	6,0	35	26/09 07:00	0,06	0,95	6,7
10	25/09 18:30	-0,21	1,11	5,7	36	26/09 07:30	0,13	0,90	6,0
11	25/09 19:00	-0,13	1,09	6,1	37	26/09 08:00	0,19	0,92	5,9
12	25/09 19:30	-0,03	1,01	6,3	38	26/09 08:30	0,25	0,89	5,2
13	25/09 20:00	0,08	0,97	6,5	39	26/09 09:00	0,31	0,96	6,1
14	25/09 20:30	0,18	1,04	6,2	40	26/09 09:30	0,34	0,95	6,3
15	25/09 21:00	0,23	1,07	6,5	41	26/09 10:00	0,37	0,91	6,2
16	25/09 21:30	0,25	1,07	6,2	42	26/09 10:30	0,36	0,92	6,5
17	25/09 22:00	0,32	0,97	6,2	43	26/09 11:00	0,35	0,90	6,4
18	25/09 22:30	0,34	1,11	6,2	44	26/09 11:30	0,29	0,92	6,5
19	25/09 23:00	0,31	1,02	6,1	45	26/09 12:00	0,20	0,93	5,9
20	25/09 23:30	0,21	0,90	6,2	46	26/09 12:30	0,09	0,94	6,3
21	26/09 00:00	0,10	0,91	6,3	47	26/09 13:00	-0,01	0,88	6,4
22	26/09 00:30	0,02	0,96	6,0	48	26/09 13:30	-0,16	0,80	6,5
23	26/09 01:00	-0,07	0,96	6,4	49	26/09 14:00	-0,30	0,81	6,7
24	26/09 01:30	-0,18	0,97	6,3	50	26/09 14:30	-0,45	0,87	5,7
25	26/09 02:00	-0,29	1,02	6,7	51	26/09 15:00	-0,56	0,88	6,2
26	26/09 02:30	-0,34	1,00	6,4	52	26/09 15:30	-0,62	0,85	5,8

Appendix D: Period P2

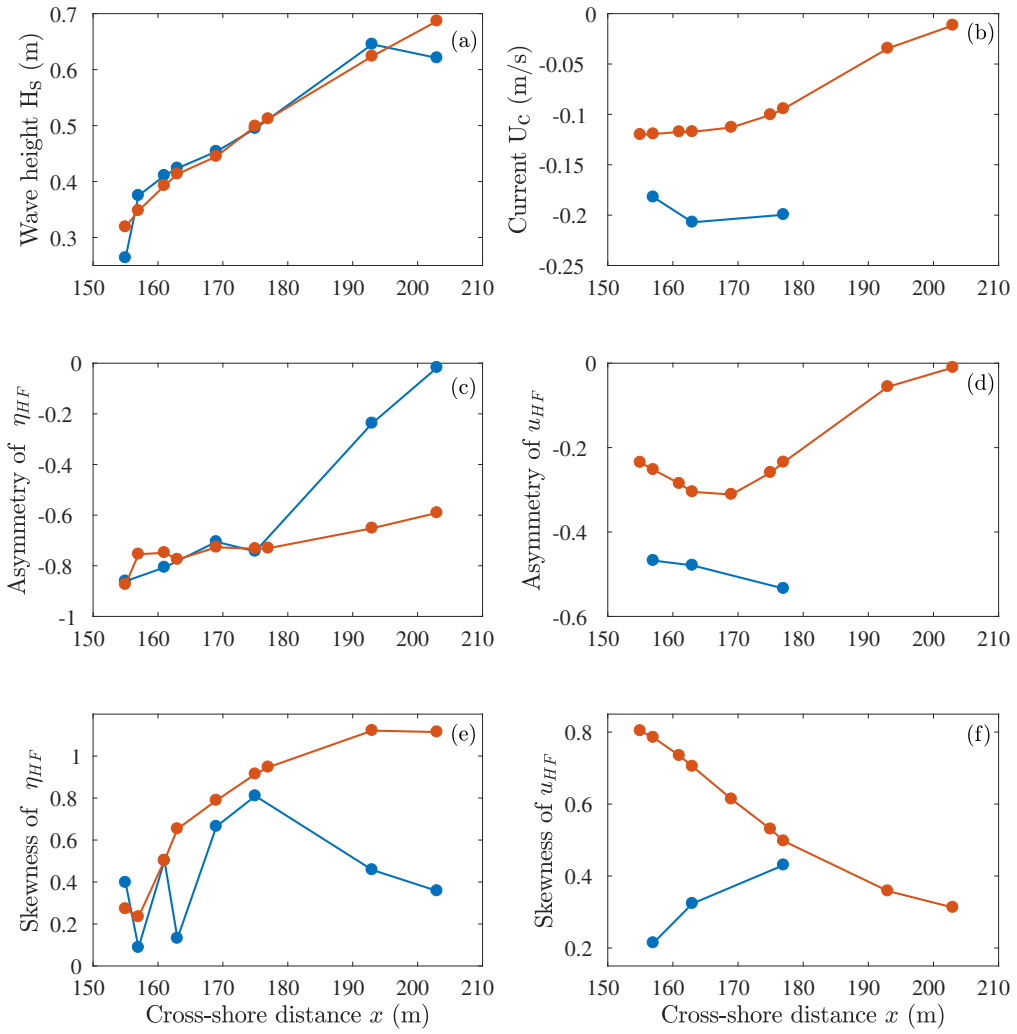

Figure D.1 – Comparison for period P2, i.e. 9:00 till 9:30 on 26-09-2016, of the hydrodynamical variables from the field data in blue and the model output in orange, using the best fit parameters Manning's roughness coefficient $n = 0.011$ m$^{-1/3}$, steepness parameter $\alpha = 0.5$ and persistence parameter $\beta = 0.3$. The six hydrodynamical variables are compared, with (a) the significant wave height H_S, (b) the mean current U_C, (c) the asymmetry determined from the high frequency sea surface elevation η_{HF}, (d) the asymmetry determined from the high frequency wave velocity u_{HF}, (e) the skewness determined from the high frequency sea surface elevation η_{HF} and (f) the skewness determined from the high frequency wave velocity u_{HF}.

Appendix E: The effect of wind

The effect of wind is not included in the model. Waves are generated by wind, which is not the case in the current model set-up where a group of random waves created with a JONSWAP spectrum enter the model at the seaward boundary. This means that no new waves are generated in the model domain of 2 km and the effect of wave growth due to wind is not included. In 1947, Sverdrup and Munk found that the wave height and wave period depend on the duration and speed of the wind. Not only waves are effected by the wind. The wind drives currents in the cross-shore and alongshore direction, influencing the hydrodynamics and the sand transport due to currents.

Wind forcing can be turned on in the SWASH model using Equation 2.25. The drag coefficient C_d has a default value of 0.002. The effect of the wind is shown by doing two simulations with a constant wind forcing, one where the wind is towards the coast and one where the wind blows away from the coast. The wind speed at 10 m height is 10 m/s, which is fairly high but makes the effect of the wind more apparent. The default values are used for the drag coefficient C_d, the Manning's roughness coefficient n and the wave breaking parameters α and β.

The high frequency sea surface elevation time series are shown in Figure 5.1 for the three cases: no wind forcing (blue), wind towards the coast (red). The significant wave height H_S and the mean current of the bottom layer U_C are also plotted in Figure E.1. The wind-driven current is onshore directed when the wind blows towards the beach, resulting in a mean current that is more onshore directed as can be seen in green. The opposite happens when the to wind blows away from the beach, so that the mean current is more offshore directed. Because the wind results in wave growth, a higher wave height was expected in case of wind forcing. However, the significant wave height H_S is lower for the simulations including wind forcing. The variance density spectra of the high frequency wave spectra are plotted in Figure E.2. The peak frequency in case of no wind forcing is 0.178 Hz. The peak frequency decreases when wind forcing is added to 0.138 Hz in case of wind towards the coast and 0.142 Hz in case of wind away from the coast. During the JONSWAP experiment by Hasselmann et al. in 1973 it was observed that the wind transfers wave energy towards lower frequencies and the frequency peak becomes sharper. The sharpening of the peak in the variance density spectrum is most apparent in the spectrum of the wind blowing away from the coast in red.

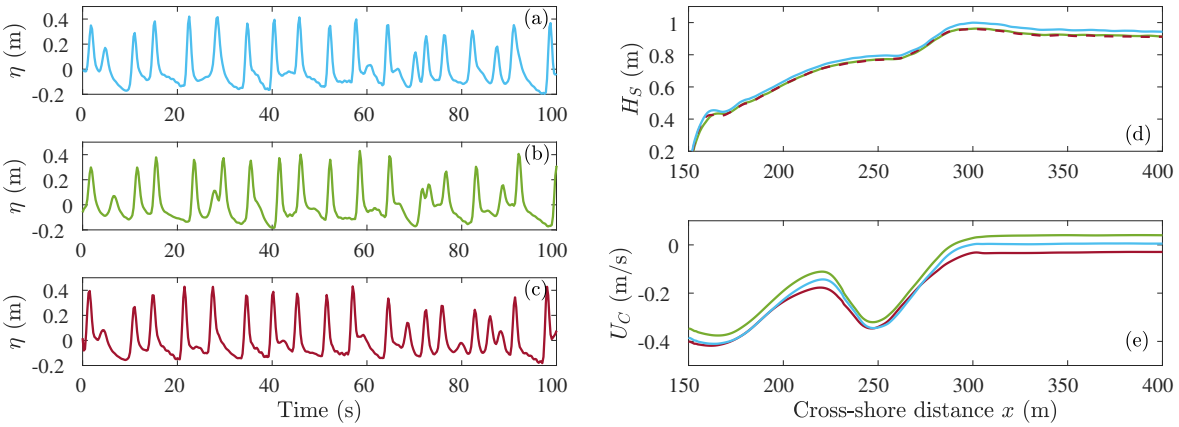

Figure E.1 – The high frequency sea surface elevation time series in case of (a) no wind, (b) wind blowing towards the coast and (c) wind blowing away from the coat. (d) The significant wave height H_S and (e) the mean current of the bottom layer U_C for the case of no wind forcing (blue), wind towards the coast (green) and wind away from the coast (red).

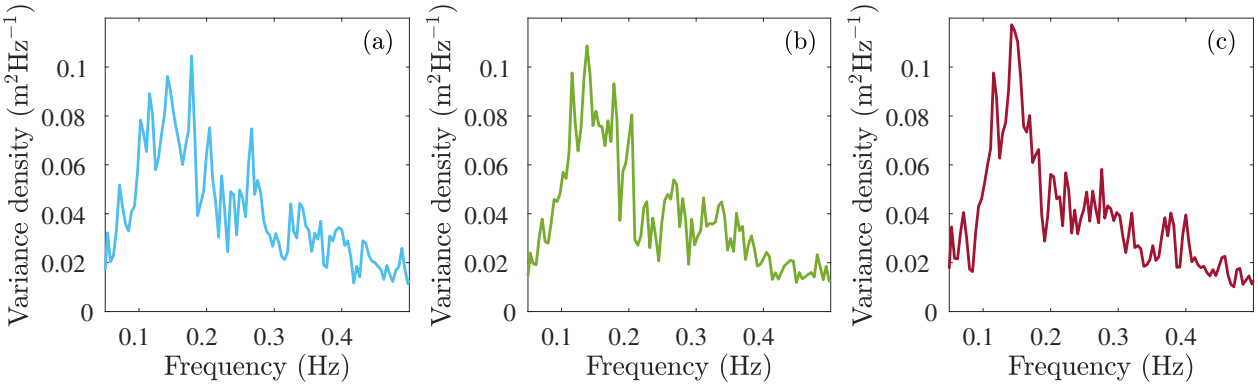

Figure E.2 – The variance wave energy density spectra of the sea surface elevation time series shown in Figure E.1 for the three cases: (a) no wind forcing, (b) wind blowing towards the coast and (c) wind blowing away from the coast.

Appendix F: The calibration results of the SWASH model using the BAR2 profile.

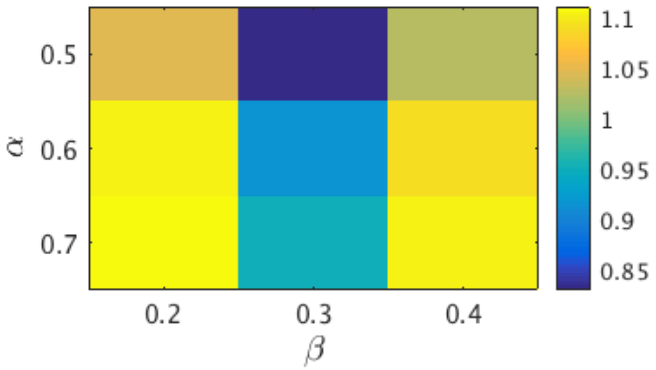

Figure F.1 – Colour plot of the total normalised root-mean-square error $E_{rms,tot}$ for for three values of the wave breaking parameters α and β, using the BAR2 profile with a constant roughness coefficient $n = 0.019$ m$^{-1/3}$s

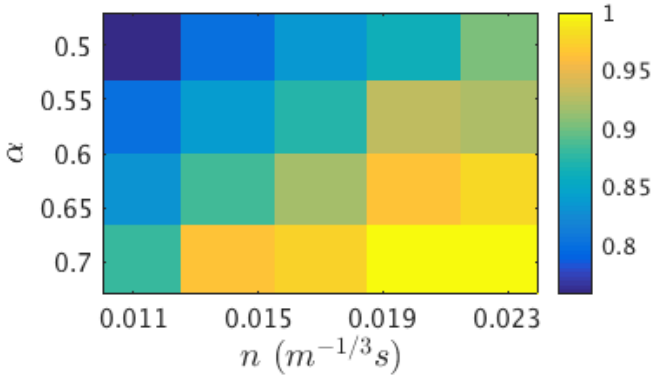

Figure F.2 – Colour plot of the total normalised root-mean-square error $E_{rms,tot}$ for four values of the Manning's roughness coefficient n and five values of the steepness parameter α, using the BAR2 profile and a constant persistence parameter $\beta = 0.3$.

Bibliography

Aagaard, T. (2011). Sediment transfer from beach to shoreface: The sediment budget of an accreting beach on the Danish North Sea Coast. *Geomorphology*, 135(1-2):143–157.

Aagaard, T., Greenwood, B., and Hughes, M. (2013). Sediment transport on dissipative, intermediate and reflective beaches. *Earth Science Reviews*, 124:32–50.

Abreu, T., Sancho, F., and Silva, P. A. (2013). Generation and evolution of longshore sandbars: model intercomparison and evaluation. In *Coastal Dynamics 2013*, pages 51–62.

Adams, T. M. and Layton, R. A. (2009). Chapter 8: Piezoresistive transducers. In *Introductory MEMS: Fabrication and applications*, chapter 8, pages 211–214. Springer Science & Business Media.

Allen, J. R. L. (1985). *Physical sedimentology*. George Allen & Unwin, London.

Bayram, A. and Larson, M. (2000). Wave transformation in the nearshore zone: Comparison between a Boussinesq model and field data. *Coastal Engineering*, 39(2-4):149–171.

Blott, S. J. and Pye, K. (2001). Gradistat: A Grain Size Distribution and Statistics Package for the Analysis of Unconcolidated Sediments. *Earth Surface Processes and Landforms*, 26:1237–1248.

Booij, N., Ris, R. C., and Holthuijsen, L. H. (1999). A third-generation wave model for coastal regions: 1. Model description and validation. *Journal of Geophysical Research*, 104(C4):7649–7666.

Boussinesq, J. (1872). Theorie des ondes et des remous qui se propagent le long d'un canal rectangulaire horizontal, en communiquant an liquide contenu dans ce canal de vitesses sensiblement pareilles de la surface anfond, Liouvilles. *J. Math.*, 17:55 –108.

Bowen, A. J. and Holman, R. (1989). Shear instabilities of the mean longshore current: 2. Field observations. *Journal of Geophysical Research*, 94(1):18031.

Brinkkemper, J. (2013). Modeling the cross-shore evolution of asymmetry and skewness of surface gravity waves propagating over a natural intertidal sandbar. Master's thesis, Utrecht University.

Brinkkemper, J., Christensen, D., Price, T., Naus, I., Hansen, A., van Bergeijk, V., van de Wetering, J., Ruessink, B., Ernstsen, V., and Aagaard, T. (2017). Surf-zone morphodynamics during low-moderate energetic conditions; the TASTI field experiment. In *Coastal Dynamics 2017*, pages 1038–1048.

Castelle, B., Ruessink, B. G., Bonneton, P., Marieu, V., Bruneau, N., and Price, T. D. (2010). Coupling mechanisms in double sandbar systems. Part 1: Patterns and physical explanation. *Earth Surface Processes and Landforms*, 35(4):476–486.

de Bakker, A. T. M., Brinkkemper, J. A., van der Steen, F., Tissier, M. F. S., and Ruessink, B. G. (2016). Cross-shore sand transport by infragravity waves as a function of beach steepness. *Journal of Geophysical Research F: Earth Surface*, 121(10):1786–1799.

Delta Committee (2008). Working together with water: A living land builds for its future. Technical report.

Dobson, F. W. (1971). The damping of a group of sea waves. *Boundary-Layer Meteorology*, 1(226):399–400.

Doering, J. C. and Bowen, A. J. (1995). Parametrization of orbital velocities asymetries of shoaling and breaking waves using bispectral analysis. *Coastal Engineering*, 26(95):15–33.

Dubarbier, B., Castelle, B., Marieu, V., and Ruessink, G. (2015). Process-based modeling of cross-shore sandbar behavior. *Coastal Engineering*, 95:35–50.

Dyer, K. (1986). Chapter 4: Sediment movement. In *Coastal and estuarine sediment dynamics*, pages 108 – 121. John Wiley and Sons, Chichester, Sussex (UK),.

Elgar, S. (1987). Relationships Involving Third Moments and Bispectra of a Harmonic Process. *IEEE Transactions on Acoustics, Speech, and Signal Processing*, 35(12):1725–1726.

Elgar, S. and Guza, R. (1985). Observations of bispectra of shoaling surface gravity waves. *Journal of Fluid Mechanics*, 161:425–448.

Fernández-Mora, A., Calvete, D., Falqués, A., and de Swart, H. E. (2015). Onshore sandbar migration in the surf zone: New insights into the wave induced sediment transport mechanisms. *Geophysical Research Letters*, 42(8):2869–2877.

Fredsøe, J. and Deigaard, R. (1992). Chapter 7: Basic concepts of sediment transport. In *Mechanics of coastal sediment transport*, pages 194 – 205. World Scientific Publishing Co Inc.

Gallagher, E. L., Elgar, S., and Guza, R. (1998). Observations of sand bar evolution on a natural beach. *Journal of Geophysical Research*, 103:3203–3215.

Garnier, R., Calvete, D., Falqués, A., and Dodd, N. (2008). Modelling the formation and the long-term behavior of rip channel systems from the deformation of a longshore bar. *Journal of Geophysical Research: Oceans*, 113(7):1–18.

Glover, T. J. (1989). *Pocket Ref*. Sequoia Publishing, 4th edition.

Hasselmann, K., Barnett, T., Bouws, E., Carlson, H., Cartwright, D., Enke, K., Ewing, J., Gienapp, H., Hasselmann, D., Kruseman, P., Meerburg, A., Müller, P., Olbers, D., Richter, K., Sell, W., and Walden, H. (1973). Measurements of wind-wave growth and swell decay during the Joint North Sea Wave Project (JONSWAP). *Ergänzungsheft zur Deutsche Hydrographischen Zeitschrift*.

Henderson, S. M. and Allen, J. S. (2004). Nearshore sandbar migration predicted by an eddy-diffusive boundary layer model. *Journal of Geophysical Research C: Oceans*, 109(6):1–15.

Hoefel, F. and Elgar, S. (2003). Wave-Induced Sediment Transport and Sandbar Migration. *Science*, 299(5614):1885–1887.

Holthuijsen, L. H. (2007). *Waves in coastal waters*. Cambridge University Press, Technische Universiteit Delft, the Netherlands.

Hsu, T. J., Elgar, S., and Guza, R. T. (2006). Wave-induced sediment transport and onshore sandbar migration. *Coastal Engineering*, 53(10):817–824.

Jensen, S. G., Aagaard, T., Baldock, T. E., Kroon, A., and Hughes, M. (2009). Berm formation and dynamics on a gently sloping beach; the effect of water level and swash overtopping. *Earth Surface Processes and Landforms*, 34(July):155–161.

Kabat, P., Fresco, L. O., Stive, M. J. F., Veerman, C. P., van Alphen, J. S. L. J., Parmet, B. W. A. H., Hazeleger, W., and Katsman, C. A. (2009). Dutch coasts in transition. *Nature Geoscience*, 2(7):450.

Kaergaard, K., Fredsoe, J., and Knudsen, S. B. (2012). Coastline undulations on the West Coast of Denmark: Offshore extent, relation to breaker bars and transported sediment volume. *Coastal Engineering*, 60(1):109–122.

Lam, D. C. L. and Simpson, R. B. (1976). Centered differencing and the box scheme for diffusion convection problems. *Journal of computational physics*, 22(4):486–500.

Leatherman, S. P., Zhang, K., and Douglas, B. C. (2000). Sea level rise shown to drive coastal erosion. *Eos, Transactions American Geophysical Union*, 81(6):55–57.

Lesser, G. R., Roelvink, J. A., van Kester, J. A. T. M., and Stelling, G. S. (2004). Development and validation of a three-dimensional morphological model. *Coastal Engineering*, 51(8-9):883–915.

Masselink, G., Hughes, M., and Knight, J. (2014). *Introduction to Coastal Processes and Geomorphology*.

Masselink, G., Kroon, A., and Davidson-Arnott, R. G. D. (2006). Morphodynamics of intertidal bars in wave-dominated coastal settings - A review. *Geomorphology*, 73(1-2):33–49.

Naus, I. (2017). Observations of alongshore variability in intertidal beach development and wave conditions. Master's thesis, Utrecht University.

Nelson, S. A. (2013). Slope Stability, Triggering Events, Mass Movement Hazards.

Noyes, T. J., Guza, R. T., Feddersen, F., Elgar, S., and Herbers, T. H. (2005). Model-data comparisons of shear wave in the nearshore. *Journal of Geophysical Research C: Oceans*, 110(5):1–12.

Ozkan-Haller, H. T. (2003). Effects of wave-current interaction on shear instabilities of longshore currents. *Journal of Geophysical Research*, 108(C5):3139.

Press, W., Teukolsky, S., Vetterling, W., Flannery, B., Ziegel, E., Press, W., Flannery, B., Teukolsky, S., and Vetterling, W. (1987). *Numerical Recipes: The Art of Scientific Computing*, volume 29.

Ribberink, J. S. (1998). Bed-load transport for steady flows and unsteady oscillatory flows. *Coastal Engineering*, 34(1-2):59–82.

Rijkswaterstaat (2017). Kustonderhoud.

Roelvink, D., Reniers, A., van Dongeren, A., van Thiel de Vries, J., McCall, R., and Lescinski, J. (2009). Modelling storm impacts on beaches, dunes and barrier islands. *Coastal Engineering*, 56(11-12):1133–1152.

Roelvink, J. and Stive, M. (1989). Bar-Generating Cross-Shore Flow Mechanisms on a Beach. *Journal of Geophysical Research*, 94(C4):4785–4800.

Ruessink, B. G., Michallet, H., Abreu, T., Sancho, F., Van Der A, D. A., Van Der Werf, J. J., and Silva, P. A. (2011). Observations of velocities, sand concentrations, and fluxes under velocity-asymmetric oscillatory flows. *Journal of Geophysical Research: Oceans*, 116(3):1–13.

Ruessink, B. G., Ramaekers, G., and Van Rijn, L. C. (2012). On the parameterization of the free-stream non-linear wave orbital motion in nearshore morphodynamic models. *Coastal Engineering*, 65:56–63.

Shields, A. (1936). Anwendung der Ähnlichkeitsmechanik und der Turbulenzforschung auf die Geschiebebewegung. *PhD Thesis Technical University Berlin, Preussischen Versuchsanstalt für Wasserbau*.

Smit, P., Zijlema, M., and Stelling, G. (2013). Depth-induced wave breaking in a non-hydrostatic, near-shore wave model. *Coastal Engineering*, 76:1–16.

Stelling, G. and Zijlema, M. (2003). An accurate and efficient finite-difference algorithm for non-hydrostatic free-surface flow with application to wave propagation. *International Journal for Numerical Methods in Fluids*, 23(May 2002):1–23.

Stocker, T. F., Qin, D., Plattner, G.-K., Tignor, M., Allen, S. K., Boschung, J., Nauels, A., Xia, Y., Bex, B., and Midgley, B. (2013). *IPCC, 2013: climate change 2013: the physical science basis. Contribution of working group I to the fifth assessment report of the intergovernmental panel on climate change*. IPCC.

Svendsen, I. A. (1984). Mass flux and undertow in a surf zone. *Coastal Engineering*, 8(4):347–365.

Sverdrup, H. U. and Munk, W. H. (1947). Wind, sea, and swell: theory of relations for forecasting.

Thornton, E. B. and Guza, R. (1983). Transformation of Wave Height Distribution. *Journal of Geophysical Research*, 88(C10):5925–5938.

Van der A, D. A., Ribberink, J. S., Van der Werf, J. J., O'Donoghue, T., Buijsrogge, R. H., and Kranenburg, W. M. (2013). Practical sand transport formula for non-breaking waves and currents. *Coastal Engineering*, 76:26–42.

Van Rijn, L., Grasmeijer, B., and Ruessink, B. (2000). Measurement errors of instruments for velocity, wave height, sand concentration and bed levels in field conditions. Technical Report November, Deltares (WL)-Utrecht University.

van Rijn, L. C. (2013). Simple General Formulae For Sand transport In Rivers, Esturies and Coastal Waters. *Retrieved from www. leovanrijn-sediment. com*, pages 1–16.

Warren, I. R. and Bach, H. K. (1992). MIKE 21: a modelling system for estuaries, coastal waters and seas. *Environmental Software*, 7(4):229–240.

Wright, J., Colling, A., and Park, D. (1999). *Waves, tides, and shallow-water processes*. Gulf Professional Publishing.

Wright, L. D. and Short, A. D. (1984). Morphodynamic variability of surf zones and beaches: A synthesis. *Marine Geology*, 56(1-4):93–118.

Zijlema, M., Stelling, G., and Smit, P. (2011). SWASH: An operational public domain code for simulating wave fields and rapidly varied flows in coastal waters. *Coastal Engineering*, 58(10):992–1012.

Zijlema, M. and Stelling, G. S. (2005). Further experiences with computing non-hydrostatic free-surface flows involving water waves. *International Journal for Numerical Methods in Fluids*, 48(2):169–197.